The Astrophysical Journal, 783:122 (31pp), 2014 March 10 doi:10.1088/0004-637X/783/2/122

THE ALLWISE MOTION SURVEY AND THE QUEST FOR COLD SUBDWARFS

J. Davy Kirkpatrick[1], Adam Schneider[2], Sergio Fajardo-Acosta[1], Christopher R. Gelino[1,3], Gregory N. Mace[4], Edward L. Wright[4], Sarah E. Logsdon[4], Ian S. McLean[4], Michael C. Cushing[2], Michael F. Skrutskie[5], Peter R. Eisenhardt[6], Daniel Stern[6], Mislav Baloković[7], Adam J. Burgasser[8], Jacqueline K. Faherty[9], George B. Lansbury[10], J. A. Rich[11], Nathalie Skrzypek[12], John W. Fowler[1], Roc M. Cutri[1], Frank J. Masci[1], Tim Conrow[1], Carl J. Grillmair[1], Howard L. McCallon[1], Charles A. Beichman[1,3], and Kenneth A. Marsh[13]
[1] Infrared Processing and Analysis Center, MS 100-22, California Institute of Technology, Pasadena, CA 91125, USA; davy@ipac.caltech.edu
[2] Department of Physics and Astronomy, MS 111, University of Toledo, 2801 West Bancroft St., Toledo, OH 43606-3328, USA
[3] NASA Exoplanet Science Institute, MS 100-22, California Institute of Technology, Pasadena, CA 91125, USA
[4] Department of Physics and Astronomy, UCLA, 430 Portola Plaza, Box 951547, Los Angeles, CA 90095-1547, USA
[5] Department of Astronomy, University of Virginia, Charlottesville, VA 22904, USA
[6] NASA Jet Propulsion Laboratory, 4800 Oak Grove Drive, Pasadena, CA 91109, USA
[7] California Institute of Technology, MC 249-17, Pasadena, CA 91125, USA
[8] Department of Physics, University of California, San Diego, CA 92093, USA
[9] Department of Terrestrial Magnetism, Carnegie Institution of Washington, Washington, DC 20015, USA
[10] Department of Physics, Durham University, Durham DH1 3LE, UK
[11] Observatories of the Carnegie Institution of Washington, 813 Santa Barbara Street, Pasadena, CA 91101, USA
[12] Astro Group, Imperial College London, Blackett Laboratory, Prince Consort Road, London SW7 2AZ, UK
[13] School of Physics and Astronomy, Cardiff University, Cardiff CF24 3AA, UK
Received 2014 January 10; accepted 2014 February 3; published 2014 February 24

ABSTRACT

The AllWISE processing pipeline has measured motions for all objects detected on *Wide-field Infrared Survey Explorer* (*WISE*) images taken between 2010 January and 2011 February. In this paper, we discuss new capabilities made to the software pipeline in order to make motion measurements possible, and we characterize the resulting data products for use by future researchers. Using a stringent set of selection criteria, we find 22,445 objects that have significant AllWISE motions, of which 3525 have motions that can be independently confirmed from earlier Two Micron All Sky Survey (2MASS) images, yet lack any published motions in SIMBAD. Another 58 sources lack 2MASS counterparts and are presented as motion candidates only. Limited spectroscopic follow-up of this list has already revealed eight new L subdwarfs. These may provide the first hints of a "subdwarf gap" at mid-L types that would indicate the break between the stellar and substellar populations at low metallicities (i.e., old ages). Another object in the motion list—WISEA J154045.67−510139.3—is a bright ($J \approx 9$ mag) object of type M6; both the spectrophotometric distance and a crude preliminary parallax place it ∼6 pc from the Sun. We also compare our list of motion objects to the recently published list of 762 *WISE* motion objects from Luhman. While these first large motion studies with *WISE* data have been very successful in revealing previously overlooked nearby dwarfs, both studies missed objects that the other found, demonstrating that many other nearby objects likely await discovery in the AllWISE data products.

Key words: brown dwarfs – catalogs – solar neighborhood – stars: fundamental parameters – stars: low-mass – subdwarfs

Online-only material: color figures, machine-readable table

1. INTRODUCTION

The *Wide-field Infrared Survey Explorer* (*WISE*; Wright et al. 2010) was built to survey the sky simultaneously in four bands with central wavelengths of 3.4, 4.6, 12, and 22 μm (hereafter referred to as $W1$, $W2$, $W3$, and $W4$, respectively). The four-band cryogenic mission covered the sky 1.2 times between 2010 January 07 and 2010 August 06. After the solid hydrogen cryogen was depleted in the outer tank, data covering 30% of the sky continued to be acquired in the three-band ($W1$, $W2$, and $W3$) cryogenic mission until 2010 September 29, when cryogen in the inner tank was exhausted. *WISE* surveyed 70% of the sky in the two-band ($W1$ and $W2$) post-cryogenic NEOWISE mission (Mainzer et al. 2011) until the satellite was placed into hibernation on 2011 February 01. In total, *WISE* surveyed the full sky twice in at least two bands and 20% of the sky a third time, with each coverage epoch separated by approximately six months.

Data were processed and released separately for the cryogenic and post-cryogenic missions. The aim of the AllWISE program was to combine all of the data from the *WISE* mission to leverage the full depth and time history of the $W1$ and $W2$ data. Specifically, one of these goals was to use the full *WISE* data to perform the first all-sky proper motion survey at these wavelengths. In addition to the exciting prospects created by doing a kinematic survey in a new wavelength regime, AllWISE processing—because of the short, six-month time baseline between epochs—enables us to search for very high motion objects that may have been overlooked by the longer time baselines of earlier all-sky motion surveys. In these surveys, an object could be "lost" between consecutive views. A case in point is the first motion discovery from AllWISE, the usdM3 star WISEA J070720.50+170532.7 (Wright et al. 2013), which is moving at $1\farcs8\,\mathrm{yr}^{-1}$ and was missed by all previous motion surveys despite being in the more heavily studied northern hemisphere, being easily detected at optical

wavelengths, and falling in an uncomplicated region free of source confusion.

In this paper, we describe how motions are measured in AllWISE (Section 2), characterize the resulting motions and present caveats to users of the AllWISE data products (Section 3), present a catalog of new motion discoveries (Section 4), compare that to the recent list of *WISE* motion discoveries published by Luhman (2014; Section 5), discuss our spectroscopic follow-up of some of the discoveries (Section 6), and highlight a couple of specific science cases—the hunt for rare, L-type subdwarfs (Section 7) and the search for missing members of the immediate solar neighborhood (Section 8)—that we have already explored using the discovery list. In Section 9, we provide a summary of our AllWISE results thus far.

2. MEASURING MOTIONS IN ALLWISE

AllWISE combines all previous *WISE* single-exposure images (called Level 1b frames) that satisfy a minimum quality standard. These individual frames are match-filtered and co-added on pre-defined $1.^{\circ}56 \times 1.^{\circ}56$ Atlas Tile footprints on the sky. Pixel outlier rejection is used to suppress transient features and objects of extremely high motion (e.g., asteroids and satellite streaks).

In processing of the earlier *WISE* data sets, the following procedure was used for source detection and astrometric/photometric measurement. A list of detections from a multiband signal-to-noise ratio map of the coadded images was first generated for each Atlas Tile. At the position of each detection in the list, a point response function fit was then performed to measure the source position and flux via a χ^2 minimization procedure on the stack of individual frames that generated the coadd. Because the *WISE* beam size is large (the full-width at half-maximum, FWHM, is $12''$ at $W4$), the deblending of overlapping detections—and the further deconvolution of those detections into possible multiple components—is handled through a χ^2 minimization procedure explained in more detail in the WISE All-Sky Release Explanatory Supplement.[14]

During AllWISE processing, the source position measurement model was augmented with linear motion terms in R.A. and Decl. (the "motion fit"). In AllWISE processing, the fit excluding these new motion terms (the "stationary fit") is performed first, and the full set of photometric parameters is computed. The motion fit begins with the stationary position as the initial position estimate at a fiducial time that is the flux-weighted mean observational epoch of each source. Because of the effects of noise on the non-linear χ^2 minimization algorithm, it is sensitive to the initial estimates used to start the minimization search. Of the several ways to weigh the epoch averaging, flux weighting based on the stationary-fit single-frame flux solutions was found to be the most effective in reproducing motions of known moving objects. Readers are encouraged to consult the AllWISE Release Explanatory Supplement[15] for additional details.

As a result of this addition to the AllWISE processing, motions are now measured for all coadd-detected *WISE* sources, giving researchers a powerful new tool with which to study and/or identify nearby stars and brown dwarfs. This paper characterizes these new motion measurements, discusses the caveats, and showcases two research areas—the search for low-metallicity stars and brown dwarfs and the hunt for missing members of the solar neighborhood—that are particularly well suited for this data set.

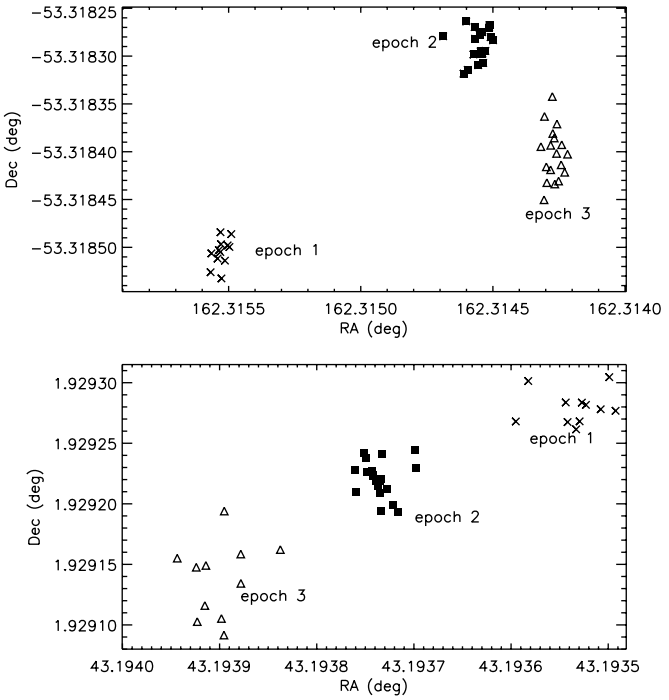

Figure 1. Astrometry measured from the individual Level 1b frames for the nearby L+T dwarf binary WISE J104915.57−531906.1 (top) and LHS 161 (bottom). The three clusters of points labeled "epoch 1," "epoch 2," and "epoch 3" show the *WISE* data separated by six-month intervals.

3. ANALYSIS OF THE ALLWISE MOTION PRODUCTS

3.1. Apparent Motion versus Proper Motion

The AllWISE time baseline is typically between six months and a year for any point on the sky. Except for ecliptic polar regions, the time sampling will be confined to discrete epochs separated by roughly six months. Multiple measurements, spanning the range of a few days, are taken at each epoch. Most of the sky has two epochs covering six months, and ∼20% of the sky has three epochs spanning a time range of one year.

It is important to understand what this time sampling means for motion measurements. In general, it is the closest objects to the Sun that exhibit the largest proper motions. Being close, these objects will also exhibit substantial parallax. Because data are taken near 90° solar elongation, *WISE* observed these objects at their maximum parallax factors. As an example, an object seen at two *WISE* epochs will have motion that is a combination of half its yearly proper motion (because the two epochs are only separated by six months) and twice its parallax (because the vantage point between epochs has shifted by 2 AU). Having only two epochs, AllWISE cannot disentangle the effects of parallax and proper motion and thus measures only *apparent motion* on the sky as opposed to *proper motion*.

Figure 1 (top panel) shows the individual Level 1b frame measurements of the position of the nearby L+T dwarf binary WISE J104915.57−531906.1. This source has three epochs of coverage in AllWISE. The motion is not linear because this binary's parallax ($\pi = 0.''50$) and proper motion ($\mu = 2.''78\,\mathrm{yr}^{-1}$) are comparable in size (Luhman 2013). It would be possible to measure the proper motion by using only the epoch 1 and epoch 3 points, since these clusters of points were

[14] See http://wise2.ipac.caltech.edu/docs/release/allsky/expsup/.
[15] See http://wise2.ipac.caltech.edu/docs/release/allwise/expsup/.

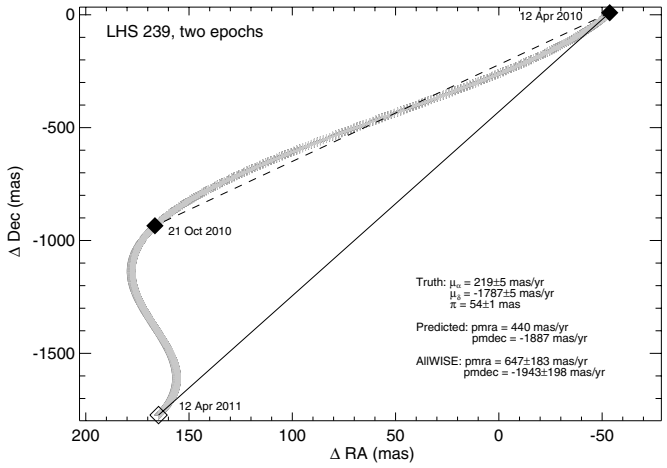

Figure 2. Predicted motion track (gray plus signs, one symbol per day) for the DC12 white dwarf LHS 239. Solid diamonds show the dates of the *WISE* observations. The open diamond shows the date 12 months after the initial *WISE* observation. AllWISE measures a motion over six months as noted by the dashed line (that is, the reported yearly motion will be twice this long), whereas the true proper motion over a full year is denoted by the solid line.

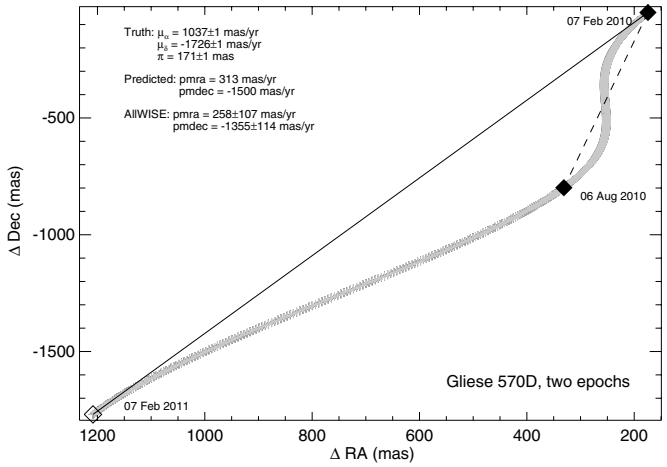

Figure 3. Predicted motion track (gray plus signs, one symbol per day) for the T7.5 brown dwarf Gliese 570D. Solid diamonds show the dates of the *WISE* observations. The open diamond shows the date 12 months after the initial *WISE* observation. AllWISE measures a motion over six months as noted by the dashed line, whereas the true proper motion over a full year is denoted by the solid line.

taken at the same parallax factor; however, AllWISE uses data from all three epochs and thus will measure a motion that is not the actual "proper" motion. The extreme M subdwarf LHS 161 in Figure 1 (bottom panel) demonstrates a case at the opposite extreme, where the parallax is swamped by a much larger proper motion ($\pi = 0\farcs025$ and $\mu = 1\farcs455\ \mathrm{yr}^{-1}$; van Altena et al. 1995). As expected for this case, the three separate epochs of data more closely follow a linear progression in time.

This can be further demonstrated with a couple of examples drawn from areas with two-epoch coverage, which represents the majority of *WISE* data. Figure 2 shows the predicted path of the white dwarf LHS 239 on the sky, and Figure 3 shows the path for the T dwarf Gliese 570 D. In each of these plots, the gray track shows the predicted path of the object from the date of the first *WISE* epoch to a date one year later. The date of the second (i.e., final) *WISE* epoch, approximately six months after the first, is also noted. The motion that AllWISE measures is the positional difference between the start of the track and the point six months later, whereas the true proper motion would be that measured between the start of the track and the point twelve months later. The true proper motion and parallax, the predicted motion from AllWISE, and the actual AllWISE values are given in the legend of both figures. Note that the actual AllWISE measurements are, within their errors, identical to the predicted values, although not necessarily close to the true proper motion measures. As stated earlier, these AllWISE measurements should be regarded as *apparent motion* values (parallax + proper motion) and not as pure *proper motion* values.

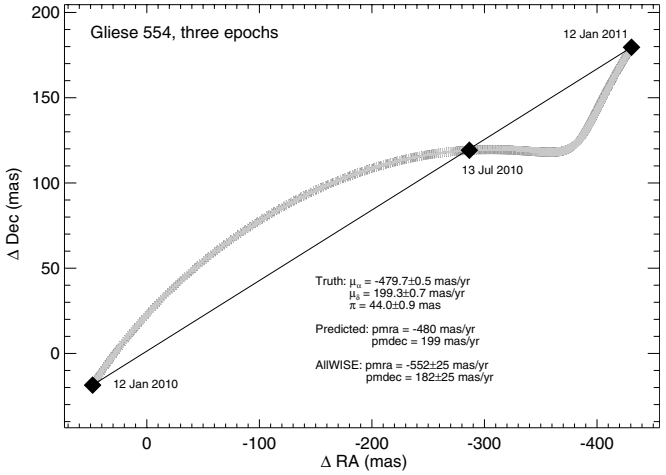

Figure 4. Predicted motion track (gray plus signs, one symbol per day) for the K3 dwarf Gliese 554. Dates of the *WISE* data points (denoted by solid diamonds) cover a full year. AllWISE measures a motion that is very close to the true proper motion in this case.

Figure 4 illustrates the predicted sky path for the K dwarf Gliese 554, located in an area with three epochs of coverage. In this case, the *WISE* data fall almost perfectly along the proper motion vector. It would be expected that the AllWISE motion measure would be very close to the true proper motion value, which is indeed the case. It should be noted that a measurement using only epoch 1+2 data would have a larger motion than a measurement using only epoch 2+3 data, although both would have the correct position angle.

Because the AllWISE-measured motions do not decouple proper motion and parallax, these motions cannot be used to predict source positions at other epochs. Rather, their utility is in identifying potentially interesting, nearby objects for further follow-up.

3.2. Motion Limits

3.2.1. What is the Largest Motion Measurable?

AllWISE is able to identify objects with very high motion. Table 1 lists the 11 highest proper motion systems known ($\mu > 4\farcs6\ \mathrm{yr}^{-1}$) and compares their published proper motions to the motions derived by AllWISE. Most of these sources are extremely bright and heavily saturated on the *WISE* detectors. Agreement between published values and those in AllWISE is not expected due both to saturation effects and to parallax. Nonetheless, the comparison shows that the highest motion stars can be identified as such in AllWISE data.

Objects with motions as high as Barnard's Star ($10\farcs4\ \mathrm{yr}^{-1}$) can be successfully recovered with AllWISE, but what is the theoretical limit to the largest motion that AllWISE can measure for a real, astrophysical source? There are sources in the combination of the AllWISE Source Catalog and Reject

Table 1
Motion Comparisons for the Eleven Highest Proper Motion Systems Known

Object Name	Sp. Type	AllWISE Designation	AllWISE $W1$ (mag)	AllWISE R.A. Motion (mas yr^{-1})	AllWISE Decl. Motion (mas yr^{-1})	Published μ_α (mas yr^{-1})	Published μ_δ (mas yr^{-1})	Published π (mas)	Ref.
(1)	(2)	(3)	(4)	(5)	(6)	(7)	(8)	(9)	(10)
Barnard's Star	M5 V	WISEA J175747.94+044323.8	5.02	−1630 ± 71	13703 ± 65	−798.58 ± 1.72	10328.12 ± 1.22	548.31 ± 1.51	1, 9
Kapteyn's Star	sdM1p	WISEA J051146.81−450204.5	4.92	8166 ± 29	−8065 ± 32	6505.08 ± 0.98	−5730.84 ± 0.96	255.66 ± 0.91	3, 9
Groombridge 1830	G7 V+	WISEA J115302.28+374206.6	4.33	2224 ± 59	−14307 ± 66	4003.98 ± 0.37	−5813.62 ± 0.23	109.99 ± 0.41	4, 9
Lacaille 9352	M2 V	WISEA J230557.86−355057.2	2.59	1866 ± 56	−841 ± 60	6768.20 ± 0.59	1327.52 ± 0.68	305.26 ± 0.70	5, 9
CD−37 15492	M3 V	WISEA J000529.35−372151.0	4.40	−471 ± 77	−2662 ± 86	5634.68 ± 0.86	−2337.71 ± 0.71	230.42 ± 0.90	5, 9
61 Cygni A	K5 V	WISEAR J210657.70+384530.8[a]	0.18	−4028 ± 52	5420 ± 54	4168.31 ± 6.57	3269.20 ± 12.08	286.82 ± 6.78	1, 9
61 Cygni B	K7 V	WISEA J210658.89+384504.5	0.97	−1171 ± 58	215 ± 66	4106.90 ± 0.32	3144.68 ± 0.44	285.88 ± 0.54	1, 9
Ross 619	M4 V	WISEA J081158.31+084529.4	7.18	1661 ± 34	−5277 ± 32	1081.4 ± 1.6	−5087.3 ± 1.6	145.5 ± 3.9	2, 11
Teegarden's Star	M6.5 V	WISEA J025303.34+165213.2	7.15	3471 ± 56	−3666 ± 25	3403.8 ± 2.2	−3807.0 ± 2.2	260.63 ± 2.69	6, 10
Lalande 21185	M2 V	WISEA J110319.67+355722.4	2.47	338 ± 50	786 ± 48	−580.27 ± 0.62	−4765.85 ± 0.64	392.64 ± 0.67	1, 9
ϵ Ind A	K2 V	WISEA J220326.69−564735.5	0.87	1218 ± 32	−26 ± 36	3960.93 ± 0.24	−2539.23 ± 0.17	276.06 ± 0.28	8, 9
ϵ Ind BaBb	T1+T6	WISEA J220415.75−564724.4	10.72	3132 ± 41	−3124 ± 38	3960.93 ± 0.24[b]	−2539.23 ± 0.17[b]	276.06 ± 0.28[b]	7, 9
Wolf 359	M6 V	WISEA J105626.19+070025.0	5.84	−2618 ± 44	−4881 ± 42	−3838.6 ± 0.2	−2697.8 ± 0.2	418.9 ± 2.4	1, 12

Notes. References for spectral type and high-precision astrometry: (1) Kirkpatrick et al. 1991; (2) Henry et al. 1994; (3) Keenan & Pitts 1980; (4) Keenan & Keller 1953; (5) Walker 1983; (6) Teegarden et al. 2003; (7) McCaughrean et al. 2004; (8) van de Kamp 1953; (9) van Leeuwen 2007; (10) Henry et al. 2006; (11) Harrington & Dahn 1980; (12) Harrington et al. 1993.

[a] 61 Cygni A is the only one of these sources failing to satisfy the criteria for inclusion in the AllWISE Source Catalog. This object is part of a small-separation same-tile (SSST) source group (see Section 3.4.3). Unfortunately, despite best efforts to recover such sources, neither member of the 61 Cyg A SSST group satisfies all the criteria necessary for Catalog consideration. The entry for 61 Cyg A can, however, be found in the AllWISE Reject Table, as the source designation indicates.

[b] The published astrometry for ϵ Ind A is used here for ϵ Ind BaBb.

Table that have single-axis motions as large as 670″ yr^{-1} (670,000 mas yr^{-1}); spot checks of these sources show them to be artifacts associated with extended structures like diffraction spikes and optical ghosts. Ultimately, the algorithm of χ^2 minimization is only limited by the detection step on the coadd images; that is, as long as a source is identified on the coadds, extremely large motions can be recovered in the Level 1b images. The only real sources that will not have a coadd detection are those moving so fast that outlier rejection will have eliminated them from the coadd entirely. Real examples of this include main belt asteroids and near-earth objects. Outlier rejection is more likely to eliminate objects seen less than 50% of the time in the frame stack.[16] So it is just possible, in the two-epoch case, for an object near the ecliptic plane moving at ∼2.5 × FWHM between the first and last exposures over one epoch, or 15″ per ∼2 days (∼2700″ yr^{-1}), to have survived coaddition and be detected. For areas of sky with three epochs of coverage, assuming equal numbers of frames per epoch, a source moving at ∼2700″ yr^{-1} would be seen within a 2.5 × FWHM window only 33% of the time, and would thus be removed from the coadd because it fails to meet the 50% outlier threshold. For such a three-epoch case, the motion limit is more likely to be ∼2.5 × FWHM between two consecutive epochs, or ∼15″ per 6 months (∼30″ yr^{-1}).

3.2.2. What is the Smallest Motion Measurable?

Figure 5 shows the motion measurement uncertainties for sources in a typical AllWISE Atlas Image plotted against $W1$ magnitude. Bright sources free of saturation effects ($8 < W1 < 10$ mag) approach an asymptote of ∼0.″035 yr^{-1} in their per-axis errors. Requiring a 3σ detection per axis means that the smallest significant motion[17] that is measurable is ∼0.″15 yr^{-1}. At fainter magnitudes, the smallest measurable significant motion increases dramatically as the minimum motion errors themselves increase. At $W1 = 15$ mag, for example, the motion errors are roughly 10 × larger, meaning that the smallest measurable significant motion is ∼1.″5 yr^{-1}.

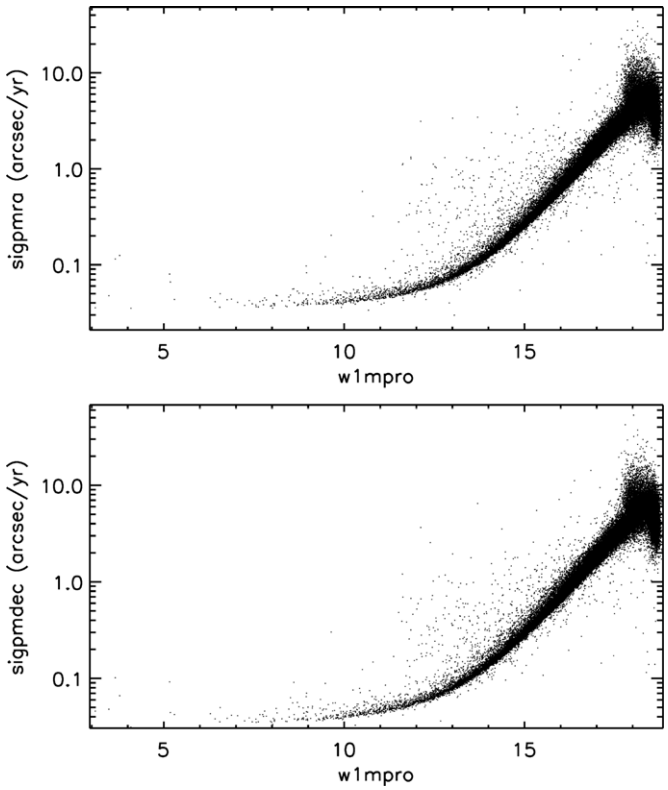

Figure 5. Uncertainty in AllWISE motion measures in R.A. (top), and Decl. (bottom) for all sources in coadd 2243m213_ac51, plotted as a function of the $W1$ profile-fit photometry.

[16] See http://wise2.ipac.caltech.edu/docs/release/allsky/expsup/sec4_4f.html#outrej of the WISE All-Sky Release Explanatory Supplement for more details.

[17] Requiring the stricter $\chi^2_{\rm motion} > 27.63$ criterion from Section 3.4 results in a smallest motion of ∼0.″18 yr^{-1}.

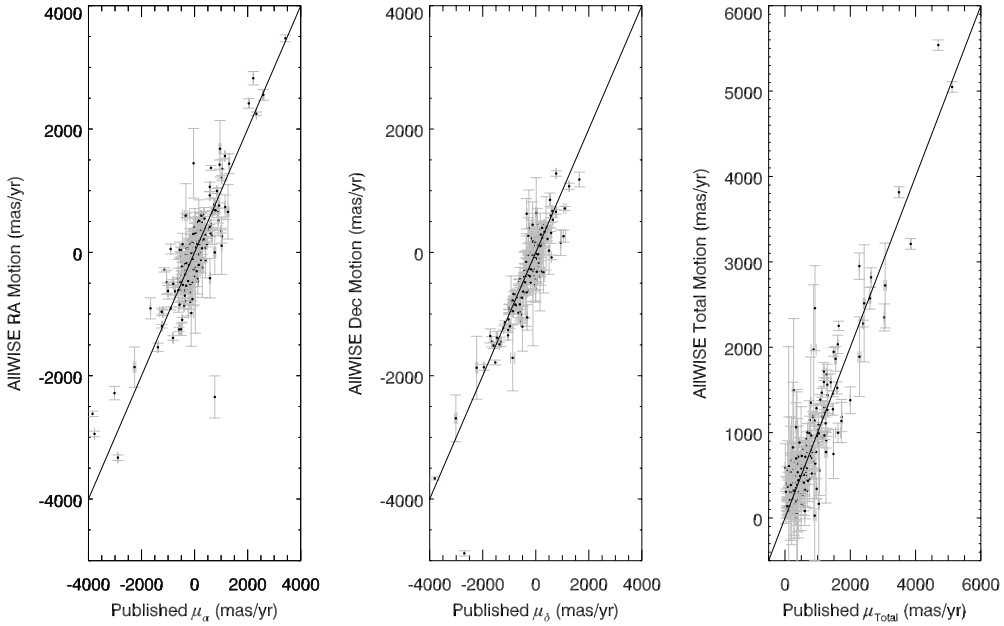

Figure 6. Comparison of the AllWISE R.A., Decl., and total motion measurements to published R.A., Decl., and total proper motion measurements of late-M, L, T, and Y dwarfs in the literature. The straight line corresponds to perfect one-to-one correspondence. The discrepant point near (800, −2350) in the left panel is Wolf 940B (*cc_flags* = "*Hh*00″), which is contaminated by the halo of Wolf 940A, and the discrepant point near (−2700, −4900) in the middle panel is the saturated star Wolf 359 (see Table 1).

The Atlas Image used in this example, 2243m213_ac51, has an average depth of coverage of ∼24 framesets, as is typical of Atlas Tiles located near the ecliptic plane and observed at two *WISE* epochs. Atlas Tiles farther from the ecliptic will have greater coverage depths. For these cases, and for any Tiles with three *WISE* epochs, motion limits will be even smaller than those quoted above.

3.3. Comparisons to Truth

Despite the fact that AllWISE measures an apparent motion over only a short time baseline, these measurements can still be compared to proper motion values determined for stars specifically targeted in astrometric monitoring campaigns as long as the sample size is statistically significant and scattered over the entire sky so that the influence of parallax is suppressed. In the first subsection below, the AllWISE motion measurements are compared to published proper motion values for an all-sky collection of late-type dwarfs. In the second subsection, the internal repeatability of the AllWISE measurements is checked using the individual components of widely separated common-proper-motion binary systems.

3.3.1. External Comparisons Using Previously Known Motion Objects

A typical user of the AllWISE data products may wish to check how the AllWISE measurements compare to published values from a favorite motion catalog. As demonstrated in Section 3.1, parallax contributes to the AllWISE motion measurements, making a direct comparison difficult. Are other statistical effects seen when a large sample is used? To this end, the AllWISE measurements have been compared to published astrometry for a set of known low-mass stars and brown dwarfs. These objects were selected because they have high signal-to-noise ratios in one or more *WISE* bands but are generally not saturated. Specifically, objects in the Database of Ultracool Parallaxes,[18] compiled as of 2013 October, were used (Dupuy & Liu 2012). This list contains proper motions for all late-M, L, T, and Y dwarfs that have published parallaxes. After excluding close binaries and blends, 233 objects were available for comparison. Figure 6 shows a comparison of the published values of μ_α, μ_δ, and $\mu_{\rm Total}$ to the R.A., Decl., and total motions measured by AllWISE. The overall agreement is excellent, with the trend very closely following the line of one-to-one correspondence.

The influence of parallax on the AllWISE motion measurements can be seen in Figure 7. In this figure, the difference between the published proper motions and the AllWISE motions shows a larger dispersion in R.A. than in Decl., and both dispersions are larger than would be expected based on the average AllWISE motion errors, which are 122.3 mas and 129.4 mas for R.A. and Decl., respectively. As shown in Figure 8, which illustrates the motion differences in R.A. and Decl. plotted as a function of parallax, the R.A. differences have a striking dependence on parallax (i.e., objects with the largest differences tend to have the largest parallax values) while the Decl. differences show only a modest increase at the largest parallaxes. Because the ecliptic and equatorial systems are tilted with respect to each other by only ∼23 degrees, parallactic motion, which is primarily manifested in ecliptic longitude, affects equatorial longitude (R.A.) more severely than equatorial latitude (Decl.). Other than this effect, no other issues are seen, as the R.A. and Decl. differences show a mean near zero and have no appreciable skew.

Figure 9 shows the motion difference plotted as a function of $W2$ mag, which for most L, T, and Y dwarfs is the *WISE* band with the highest signal-to-noise ratio and thus the band driving the astrometry. Agreement is best in the range $7 < W2 < 12$ mag. Astrometric precision is degraded at brighter magnitudes ($W2 < 7$ mag) because such objects have saturated image cores, and it quickly degrades at fainter magnitudes ($W2 > 12$ mag) due to poorer photon counting statistics.

[18] See https://www.cfa.harvard.edu/~tdupuy/plx/Database_of_Ultracool_Parallaxes.html.

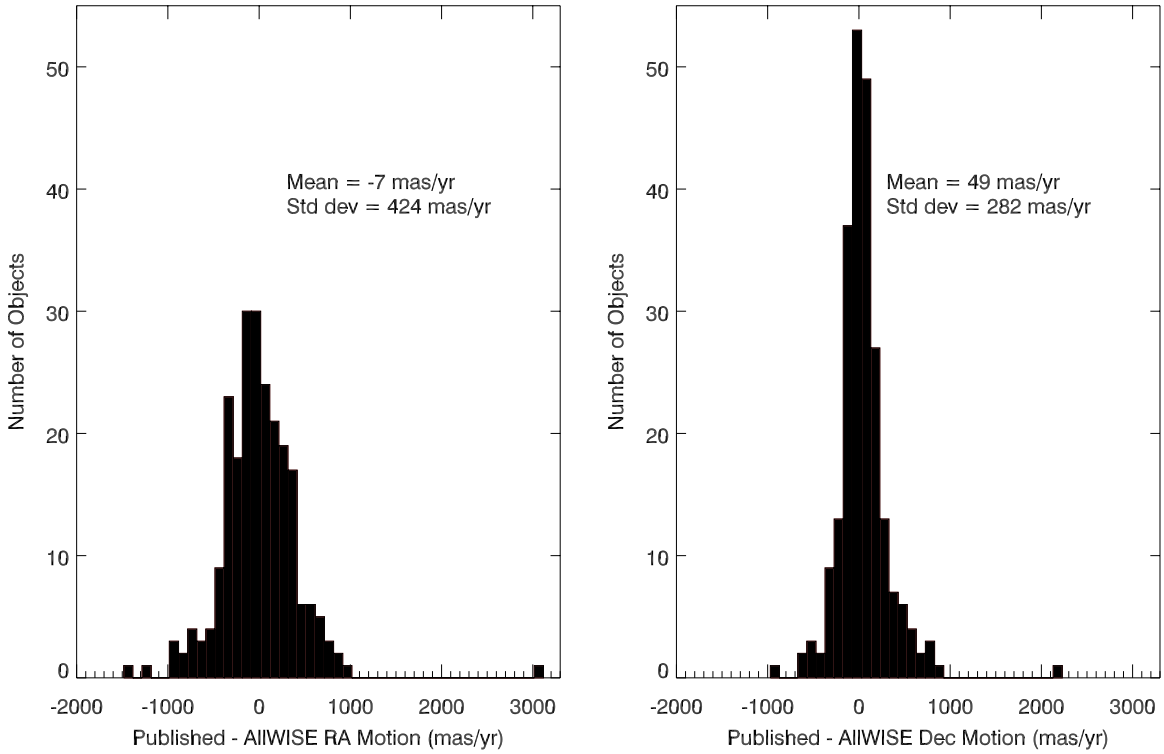

Figure 7. Histograms of the difference between published and AllWISE motions in R.A. (left panel) and Decl. (right panel) for late-M, L, T, and Y dwarfs.

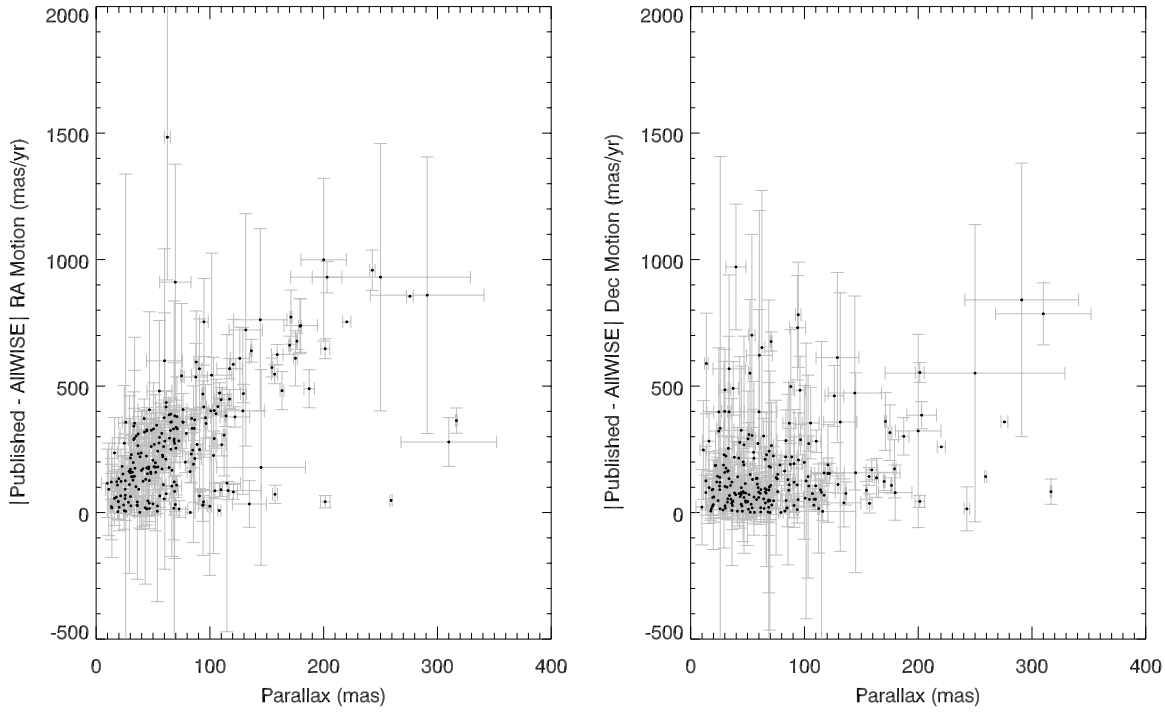

Figure 8. Absolute value of the difference between published proper motion and AllWISE motion in R.A. (left) and Decl. (right) as a function of parallax for late-M, L, T, and Y dwarfs.

3.3.2. Internal Consistency Checks Using Common-proper-motion Binaries

As part of AllWISE Quality Assurance checks, the software reported sources in each Atlas Tile that had a high likelihood of being real motion stars. (See Section 3.4 below.) During the course of quality assessment, reviewers noted 55 pairs of objects identified as having significant motions and located within ∼15″–400″ of each other. These pairs were checked in SIMBAD and were confirmed to be known common-proper-motion systems, found to be new ones verified through independent means, or identified as possible new pairs based on independent checks. The AllWISE measured motions should be identical for each member of the pair because the common parallax between components will affect the motion measures identically. Therefore, we can use these systems to perform

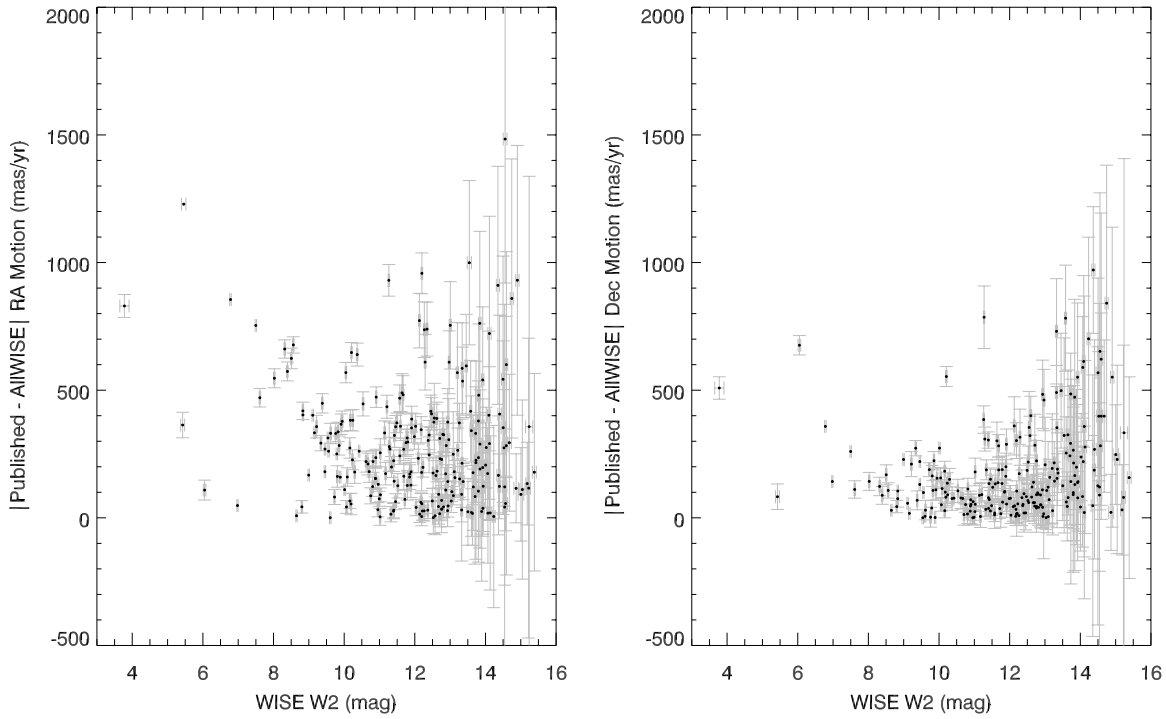

Figure 9. Absolute value of the difference between published proper motion and AllWISE motion in R.A. (left) and Decl. (right) as a function of *WISE W*2 profile-fit magnitude for late-M, L, T, and Y dwarfs.

an internal consistency check to see whether AllWISE motion measurements are the same within the errors.

Table 2 lists these fifty-five common-proper-motion binaries and Figure 10 shows the difference in motion between the two members of each pair. The difference is shown per axis, is expressed in units of the larger motion error within the pair, and is plotted as a function of the $W1$ profile-fit magnitude of the source with the larger motion error. Overall, agreement is very good. The majority of unsaturated pairs has a difference <2 times the error.

3.4. Motions, Both Real and False

In this section, we examine the distribution of motions for objects in a typical $1.^{\circ}56 \times 1.^{\circ}56$ AllWISE Atlas Image. We then extract sources having statistically significant motions and discuss the average success rate for finding bona fide motion stars. In the final subsection, we take a broader view and categorize the sources of false motion seen during our quality assurance checks (described in more detail in Section 4.1) over the entire sky.

3.4.1. A Typical Distribution of Motion Measurements

Motion measurements for all sources in a typical Atlas Image are illustrated in Figure 11. The total proper motion is plotted as a function of $\chi^2_{\rm motion} = (pmra/sigpmra)^2 + (pmdec/sigpmdec)^2$, where *pmra* and *pmdec* are the AllWISE-measured R.A. and Decl. motions, respectively, and *sigpmra* and *sigpmdec* are their associated uncertainties. AllWISE tiles typically have $\sim 10^5$ extracted sources, so any source with $Q = e^{-\chi^2_{\rm motion}/2} < 10^{-6}$ violates,[19] with a very high degree of confidence, the hypothesis of a real object with zero motion (and errors correctly

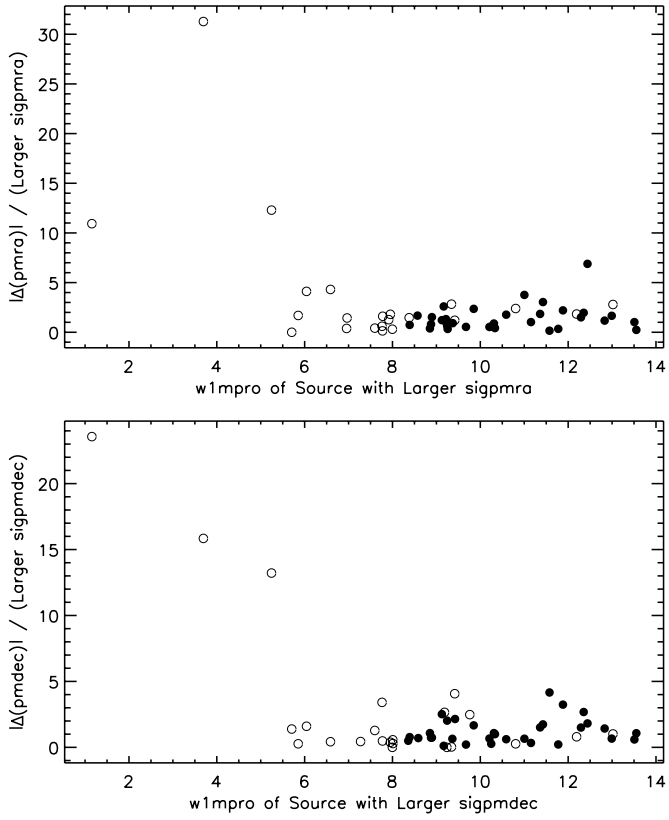

Figure 10. Difference in motion in R.A. (top) and Decl. (bottom), expressed in units of the larger motion error within the pair, for 55 common proper motion binaries noted during quality assessment. These differences are plotted as a function of the $W1$ profile-fit magnitude of the source with the larger motion error. Pairs having at least one component in the saturated regime ($W1 < 8.1$ mag or $W2 < 7.0$ mag) are shown by open circles. All others are shown by solid circles.

[19] This threshold was found to produce a sample of potentially interesting motion sources for human perusal that was not too small and not overwhelmingly large.

Table 2
Common-proper-motion Binaries Noted During AllWISE Quality Checks

WISEA Designation	*W*1 (mag)	*W*2 (mag)	AllWISE R.A. Motion (mas yr^{-1})	AllWISE Decl. Motion (mas yr^{-1})	Note
(1)	(2)	(3)	(4)	(5)	(6)
J012655.16+120022.0	9.872 ± 0.022	9.886 ± 0.021	−83 ± 36	−364 ± 33	NLTT 4817, LSPM J0126+1200N
J012654.11+120002.9	12.830 ± 0.023	12.669 ± 0.027	−151 ± 58	−444 ± 56	NLTT 4814, LSPM J0126+1200S (sep 24.″5)
J013054.96+524442.3	7.915 ± 0.027	7.977 ± 0.020	−222 ± 26	22 ± 24	BD+51 318A
J013056.36+524500.8	9.760 ± 0.024	9.658 ± 0.020	−189 ± 25	−40 ± 25	BD+51 318B (sep 22.″5)
J015329.15+732940.2	8.109 ± 0.023	8.058 ± 0.020	420 ± 31	−208 ± 30	LP 29-233, "LHS 6036"
J015326.94+733015.4	9.124 ± 0.023	8.939 ± 0.020	459 ± 32	−130 ± 31	LP 29-232, "LHS 6035" (sep 36.″4)
J021157.87+042140.9	6.955 ± 0.054	7.020 ± 0.020	−155 ± 26	−11 ± 25	BD+03 301, LSPM J0211+0421
J021159.43+042150.7	9.184 ± 0.023	9.080 ± 0.020	−145 ± 26	−80 ± 26	*new cpm companion*[a] (sep 25.″3)
J022104.69+365258.7	8.358 ± 0.024	8.180 ± 0.021	768 ± 26	−562 ± 26	GJ 1047AB, LHS 1393
J022102.54+365241.5	9.256 ± 0.023	9.060 ± 0.020	777 ± 27	−549 ± 26	GJ 1047C, LHS 1392 (sep 31.″0)
J025051.72+033035.6	8.852 ± 0.022	8.904 ± 0.019	175 ± 26	−83 ± 25	BD+02 436A, LSPM J0250+0330N
J025051.32+033006.7	9.023 ± 0.022	9.077 ± 0.019	185 ± 26	−56 ± 25	BD+02 436B, LSPM J0250+0330S (sep 29.″5)
J025403.21−355418.7	5.853 ± 0.119	5.731 ± 0.047	523 ± 26	−150 ± 26	LHS 1466
J025402.74−355454.7	8.179 ± 0.022	8.066 ± 0.019	479 ± 24	−143 ± 24	LHS 1467 (sep 36.″4)
J030531.36+114952.8	7.997 ± 0.023	7.863 ± 0.019	165 ± 26	−254 ± 26	G 5-13, LSPM J0305+1149N
J030530.76+114932.1	8.346 ± 0.023	8.249 ± 0.020	157 ± 26	−254 ± 26	G 5-12, LSPM J0305+1149S (sep 22.″6)
J031407.66+083319.0	8.391 ± 0.023	8.433 ± 0.021	303 ± 38	−14 ± 36	G 79-15, LSPM J0314+0833S
J031408.29+083345.6	8.707 ± 0.022	8.702 ± 0.021	275 ± 37	14 ± 36	G 79-16, LSPM J0314+0833N (sep 28.″2)
J031608.21−374158.4	9.565 ± 0.023	9.624 ± 0.020	65 ± 24	51 ± 24	TYC 7561-77-1
J031606.54−374215.4	13.552 ± 0.024	13.341 ± 0.027	55 ± 42	6 ± 42	*new cpm companion*[b] (sep 26.″1)
J033528.69−321806.2	9.007 ± 0.023	8.941 ± 0.020	−292 ± 25	−331 ± 24	LP 888-32, LEHPM 3410
J033530.11−321829.1	10.333 ± 0.023	10.146 ± 0.021	−303 ± 26	−306 ± 25	LP 888-33, LEHPM 3411 (sep 29.″1)
J033936.37+252814.8	7.777 ± 0.024	7.698 ± 0.020	377 ± 36	−497 ± 34	Wolf 204, LHS 1573
J033940.66+252842.2	8.007 ± 0.023	7.919 ± 0.021	319 ± 36	−517 ± 35	Wolf 205, LHS 1574 (sep 64.″4)
J035228.33−315026.6	12.741 ± 0.023	12.499 ± 0.023	231 ± 32	−531 ± 32	LHS 1609
J035227.56−315105.2	13.508 ± 0.023	13.254 ± 0.026	189 ± 41	−506 ± 42	*new cpm companion*[c] (sep 39.″8)
J043942.59+095215.6	6.464 ± 0.086	6.406 ± 0.023	−24 ± 37	−456 ± 35	G 83-28
J043943.24+095142.9	9.238 ± 0.023	9.077 ± 0.020	14 ± 39	−456 ± 37	G 83-29 (sep 34.″1)
J044349.59−481934.0	5.706 ± 0.130	5.558 ± 0.046	63 ± 37	347 ± 36	LTT 2077
J044350.89−482003.8	9.517 ± 0.023	9.363 ± 0.020	63 ± 31	297 ± 30	*new cpm companion*[d] (sep 32.″5)
J051729.18−345346.0	>1.155	>1.308	712 ± 42[y]	627 ± 39[y]	*o* Columbae, CD−35 2214
J051723.88−345121.8	9.724 ± 0.023	9.538 ± 0.019	253 ± 34	−292 ± 33	*new cpm companion*[e] (sep 158.″2)
J065438.74+131038.5	3.694 ± 0.394	3.369 ± 0.283	2033 ± 57[y]	−1035 ± 64[y]	38 Geminorum AB, HR 2564
J065448.82+131002.5	9.840 ± 0.023	9.664 ± 0.020	250 ± 38	−21 ± 36	*new cpm companion*[f] (sep 151.″6)
J074020.22−172451.5	9.064 ± 0.022	8.831 ± 0.020	1563 ± 34	−628 ± 33	LHS 235
J074021.62−172454.8	12.440 ± 0.023	12.432 ± 0.025	1928 ± 53	−726 ± 54	LHS 234[g] (sep 20.″3)
J075812.35+875734.7	8.850 ± 0.022	8.681 ± 0.020	−222 ± 28	−536 ± 28	LHS 1962
J075909.31+875742.9	10.207 ± 0.023	10.001 ± 0.020	−238 ± 30	−556 ± 30	LHS 1965 (sep 31.″5)
J082854.03−243541.8	9.308 ± 0.022	9.185 ± 0.021	200 ± 36	−335 ± 36	WT 1549
J082852.10−243536.5	11.881 ± 0.023	11.665 ± 0.022	297 ± 44	−186 ± 46	*new cpm companion*[h] (sep 26.″9)
J103734.02+295955.5	10.092 ± 0.023	9.939 ± 0.021	284 ± 38	−84 ± 38	LP 316-395, LSPM J1037+2959N
J103734.43+295937.9	11.153 ± 0.022	10.967 ± 0.022	327 ± 42	−98 ± 42	LP 316-396, LSPM J1037+2959S (sep 18.″4)
J105607.88−575041.1	10.309 ± 0.022	10.164 ± 0.020	−182 ± 25	125 ± 25	UPM J1056−5750
J105536.09−575042.1	10.366 ± 0.023	10.227 ± 0.020	−160 ± 24	152 ± 25	*new cpm companion*[i] (sep 254.″8)
J110604.58+425246.3	10.323 ± 0.023	10.151 ± 0.020	−156 ± 35	−384 ± 36	G 176-13
J110605.07+425303.3	11.361 ± 0.023	11.111 ± 0.021	−84 ± 39	−325 ± 39	G 176-14 (sep 17.″9)
J113333.55−413954.4	8.675 ± 0.023	8.712 ± 0.020	−140 ± 25	−134 ± 25	CD−40 6796
J113333.67−414016.7	10.589 ± 0.024	10.484 ± 0.020	−186 ± 26	−118 ± 26	*new cpm companion*[j] (sep 22.″3)
J120907.21+473602.2	9.166 ± 0.023	8.975 ± 0.021	713 ± 35	−349 ± 35	LHS 2516
J120907.24+473531.8	10.036 ± 0.024	9.856 ± 0.020	804 ± 35	−353 ± 35	LHS 2517 (sep 30.″4)
J121058.01−461917.3	6.042 ± 0.097	5.997 ± 0.040	−4 ± 26	169 ± 25	CD−45 7595, LTT 4560
J121058.26−461204.5	8.822 ± 0.022	8.711 ± 0.020	103 ± 25	129 ± 25	*new cpm companion*[k] (sep 432.″8)
J124007.18+204828.9	6.801 ± 0.066	6.837 ± 0.020	250 ± 35	−449 ± 35	G 59-32, BD+21 2442
J124014.80+204752.7	13.020 ± 0.024	12.803 ± 0.026	426 ± 63	−381 ± 67	*new cpm companion*[l] (sep 112.″7)
J124725.86−434353.2	7.850 ± 0.023	7.893 ± 0.019	−165 ± 24	−162 ± 24	LTT 4892, CD−43 7881
J124726.75−434441.8	12.192 ± 0.023	11.997 ± 0.021	−220 ± 30	−138 ± 30	*new cpm companion*[m] (sep 49.″5)
J124737.85−274637.3	9.715 ± 0.022	9.568 ± 0.020	−220 ± 27	−15 ± 26	LP 853-37
J124739.94−274642.7	9.849 ± 0.022	9.700 ± 0.020	−154 ± 28	−60 ± 27	LP 853-38 (sep 28.″4)
J125433.93−381122.7	7.951 ± 0.024	8.016 ± 0.020	208 ± 26	−68 ± 26	TYC 7772-1225-1
J125435.54−381111.7	8.175 ± 0.022	8.209 ± 0.019	161 ± 26	−78 ± 26	*possible new cpm companion*[n] (sep 22.″0)
J131407.63+061814.3	11.804 ± 0.022	11.790 ± 0.022	−206 ± 33	−294 ± 33	G 62-19, LSPM J1314+0618S
J131408.36+061828.3	12.291 ± 0.022	12.231 ± 0.022	−152 ± 36	−240 ± 36	G 62-20, LSPM J1314+0618N (sep 17.″8)
J134454.85−453518.5	7.547 ± 0.025	7.570 ± 0.019	−304 ± 33	67 ± 32	LTT 5330
J134457.17−453537.2	9.343 ± 0.022	9.160 ± 0.019	−403 ± 35	68 ± 34	*new cpm companion*[o] (sep 30.″7)

Table 2
(Continued)

WISEA Designation	$W1$ (mag)	$W2$ (mag)	AllWISE R.A. Motion (mas yr^{-1})	AllWISE Decl. Motion (mas yr^{-1})	Note
(1)	(2)	(3)	(4)	(5)	(6)
J140400.30−592400.5	9.363 ± 0.021	9.179 ± 0.020	−44 ± 34	−418 ± 34	L 197-165, NLTT 36089
J140350.20−592348.0	9.371 ± 0.022	9.194 ± 0.020	−76 ± 35	−396 ± 34	*new cpm companion*[p] (sep 78.″1)
J140926.79−305551.4	7.772 ± 0.026	7.819 ± 0.021	−496 ± 29	−271 ± 29	LHS 2807
J140924.56−305534.1	8.728 ± 0.023	8.643 ± 0.020	−492 ± 26	−285 ± 25	*new cpm companion*[q] (sep 33.″4)
J141509.28+221537.3	8.877 ± 0.022	8.891 ± 0.020	−212 ± 26	129 ± 26	NLTT 36714, LSPM J1415+2215S
J141509.80+221559.8	8.966 ± 0.022	9.042 ± 0.019	−191 ± 26	110 ± 26	NLTT 36716, LSPM J1415+2215N (sep 23.″7)
J142051.70−045805.5	8.348 ± 0.032	8.393 ± 0.029	−76 ± 25	−75 ± 26	BD−04 3668
J142053.60−050137.8	11.003 ± 0.023	10.877 ± 0.020	−185 ± 29	−56 ± 29	*new cpm companion*[r] (sep 214.″2)
J153519.64+174245.2	7.762 ± 0.022	7.597 ± 0.019	−1455 ± 38	34 ± 34	Ross 513A, LHS 399
J153519.45+174302.6	9.316 ± 0.023	9.081 ± 0.020	−1478 ± 36	−82 ± 33	Ross 513B, LHS 400 (sep 17.″6)
J154850.51+175056.1	8.855 ± 0.023	8.781 ± 0.020	−268 ± 36	165 ± 36	G 137-55, LSPM J1548+1750E
J154848.52+175050.0	9.673 ± 0.022	9.525 ± 0.020	−288 ± 37	157 ± 38	G 137-54, LSPM J1548+1750W (sep 29.″1)
J155306.56+344508.8	6.966 ± 0.034	6.877 ± 0.020	158 ± 32	−470 ± 29	LHS 3129
J155306.84+344442.4	8.009 ± 0.023	7.884 ± 0.020	112 ± 32	−479 ± 31	LHS 3130 (sep 26.″6)
J155831.76+572242.3	7.597 ± 0.030	7.674 ± 0.020	133 ± 24	−241 ± 25	G 225-39
J155831.67+572309.1	10.000 ± 0.023	9.823 ± 0.020	143 ± 24	−209 ± 24	G 225-38 (sep 26.″8)
J164836.25+550743.4	7.273 ± 0.030	7.325 ± 0.020	162 ± 25	−269 ± 25	G 226-28
J164835.74+550809.7	8.379 ± 0.023	8.461 ± 0.020	124 ± 26	−258 ± 25	G 226-27 (sep 26.″6)
J165524.66−081930.5	6.588 ± 0.061	6.374 ± 0.022	−1207 ± 42	−764 ± 40	LHS 427
J165534.68−082349.7	8.619 ± 0.023	8.393 ± 0.020	−1388 ± 37	−781 ± 35	LHS 429, vB 8 (sep 298.″9)
J170428.76+034342.7	8.570 ± 0.022	8.586 ± 0.020	−408 ± 37	−196 ± 36	G 19-10
J170428.57+034422.7	8.587 ± 0.023	8.648 ± 0.020	−346 ± 37	−170 ± 37	G 19-11 (sep 40.″1)
J171828.99−224630.2	9.217 ± 0.024	9.056 ± 0.020	−270 ± 43	−138 ± 39	*new cpm system*[s]
J171826.98−224543.5	9.424 ± 0.023	9.313 ± 0.019	−327 ± 42	−52 ± 40	*new cpm system*[s] (sep 54.″3)
J172230.07−695119.2	8.336 ± 0.023	8.243 ± 0.020	−236 ± 40	−221 ± 36	*possible new cpm system*[t]
J172237.14−695112.2	11.426 ± 0.023	11.259 ± 0.021	−81 ± 51	−308 ± 50	*possible new cpm system*[t] (sep 54.″3)
J182000.63−522138.6	9.244 ± 0.023	9.170 ± 0.020	125 ± 39	−308 ± 38	L 272-87, NLTT 46256
J182001.39−522200.7	9.512 ± 0.023	9.399 ± 0.020	151 ± 38	−385 ± 38	L 272-88, NLTT 46257 (sep 23.″1)
J182038.54+404836.0	11.156 ± 0.023	11.047 ± 0.020	−202 ± 39	−264 ± 42	NLTT 46342, LSPM J1820+4048N
J182038.57+404759.2	11.774 ± 0.023	11.609 ± 0.020	−188 ± 41	−274 ± 46	NLTT 46343, LSPM J1820+4048S (sep 36.″9)
J185252.01−570745.3	7.473 ± 0.032	7.462 ± 0.020	−368 ± 35	−836 ± 34	LHS 3421
J185257.45−570821.9	10.804 ± 0.024	10.620 ± 0.020	−466 ± 41	−847 ± 41	2MASS J18525777−5708141 (sep 57.″4)
J190250.67−755058.1	10.928 ± 0.023	10.768 ± 0.021	−13 ± 38	−225 ± 38	SCR J1902−7550A
J190254.95−755110.8	12.353 ± 0.023	12.135 ± 0.023	87 ± 51	−375 ± 56	SCR J1902−7550B (sep 22.″5)
J201605.71−115838.5	8.778 ± 0.022	8.629 ± 0.019	−258 ± 39	−230 ± 37	*new cpm system*[u]
J201605.96−115916.7	8.897 ± 0.022	8.746 ± 0.019	−197 ± 40	−202 ± 38	*new cpm system*[u] (sep 38.″3)
J205103.71−013357.8	9.639 ± 0.023	9.611 ± 0.019	−285 ± 41	−168 ± 40	Wolf 885, NLTT 50000
J205103.50−013342.6	10.248 ± 0.023	10.136 ± 0.019	−310 ± 43	−179 ± 41	Wolf 884, NLTT 49999 (sep 15.″6)
J210630.56−382606.1	12.874 ± 0.023	12.599 ± 0.026	156 ± 67	−530 ± 69	*new cpm system*[v]
J210632.73−382640.4	12.992 ± 0.023	12.717 ± 0.025	40 ± 70	−577 ± 71	*new cpm system*[v] (sep 42.″7)
J214737.18−135422.0	9.809 ± 0.023	9.798 ± 0.020	156 ± 41	−260 ± 42	Ross 208
J214736.41−135335.4	11.575 ± 0.023	11.464 ± 0.021	164 ± 51	−468 ± 50	*new cpm companion*[w] (sep 48.″0)
J230213.97+801412.0	6.683 ± 0.071	6.704 ± 0.022	−73 ± 27	168 ± 28	BD+79 762
J230226.16+801241.8	9.417 ± 0.023	9.278 ± 0.020	−108 ± 29	290 ± 30	*new cpm companion*[x] (sep 95.″3)
J231049.97+453041.3	5.245 ± 0.174	5.107 ± 0.072	−864 ± 54[y]	331 ± 55[y]	HD 218868, LTT 16813, WDS 23108+4531A
J231054.77+453043.5	9.690 ± 0.023	9.515 ± 0.021	−200 ± 36	−396 ± 35	WDS 23108+4531C (sep 50.″5)

Notes.

[a] WISEA J021159.43+042150.7: Using the 2MASS-to-WISE time baseline we obtain a motion, (μ_α, μ_δ), of (-140.5 ± 10.2, -65.8 ± 9.3) mas yr^{-1} for this object. The other component, BD+03 301, has a published motion of (-144.70 ± 1.64, -78.66 ± 1.18) mas yr^{-1} (van Leeuwen 2007). These motions are identical within their 2σ errors, so this is likely a common-proper-motion system.

[b] WISEA J031606.54−374215.4: Using the 2MASS-to-WISE time baseline we obtain a motion, (μ_α, μ_δ), of (48.0 ± 11.3, 36.3 ± 10.4) mas yr^{-1} for this object. The other component, TYC 7561-77-1, has a published motion of (57.4 ± 2.2, 30.6 ± 2.1) mas yr^{-1} (Høg et al. 2000). Although small, these motions are identical within their 1σ errors, so this is likely a common-proper-motion system.

[c] WISEA J035227.56−315105.2: Using the 2MASS-to-WISE time baseline we obtain a motion, (μ_α, μ_δ), of (196.6 ± 11.0, -531.9 ± 10.4) mas yr^{-1} for this object. The other component, LHS 1609, has a published motion of (219, −533) mas yr^{-1} (Luyten 1979a). These motions are identical to within 2σ, so this is likely a common-proper-motion binary.

[d] WISEA J044350.89−482003.8: Using the 2MASS-to-WISE time baseline we obtain a motion, (μ_α, μ_δ), of (-5.5 ± 9.0, 263.4 ± 8.8) mas yr^{-1} for this object. The other component, LTT 2077, has a published motion of (4.75 ± 0.37, 276.85 ± 0.43) mas yr^{-1} (van Leeuwen 2007). These motions are identical to within 2σ, so this is likely a common-proper-motion binary.

[e] WISEA J051723.88−345121.8: Using the 2MASS-to-WISE time baseline we obtain a motion, (μ_α, μ_δ), of (86.7 ± 8.2, -340.4 ± 8.0) mas yr^{-1} for this object. The other component, *o* Columbae, has a published motion of (92.67 ± 0.14, -336.23 ± 0.22) mas yr^{-1} (van Leeuwen 2007). These motions are identical within their 1σ errors, so this is very likely a common-proper-motion system.

Table 2
(Continued)

[f] WISEA J065448.82+131002.5: Using the 2MASS-to-WISE time baseline we obtain a motion, (μ_α, μ_δ), of (63.7 ± 9.2, -86.2 ± 8.8) mas yr^{-1} for this object. The other component, 38 Geminorum AB, has a published motion of (68.48 ± 1.78, -72.98 ± 1.46) mas yr^{-1} (van Leeuwen 2007). These motions are identical within their 2σ errors, so this is likely a common-proper-motion system.

[g] WISEA J074021.62−172454.8: This object falls in a tile overlap region, so it was processed twice by AllWISE. The apparition chosen for inclusion in the AllWISE Source Catalog, whose values are listed in the table above, was selected over the other apparition because the former is further from the tile edge. The other apparition, which appears in the AllWISE Reject Table as WISEAR J074021.62−172454.8, has motion values of 1563 ± 50 mas yr^{-1} and -608 ± 52 mas yr^{-1} in R.A. and Decl., respectively. The values for the AllWISE Reject source are $<1\sigma$ discrepant from either apparition of the primary, LHS 235. Because the same underlying frames are used for both tiles, it is unclear why the motion for one of the apparitions of LHS 234 is so wildly discrepant in R.A.

[h] WISEA J082852.10−243536.5: Using the 2MASS-to-WISE time baseline we obtain a motion, (μ_α, μ_δ), of (157.6 ± 10.8, -137.5 ± 10.7) mas yr^{-1} for this object. The other component, WT 1549, has a published motion of (151 ± 13, -140 ± 13) mas yr^{-1} (Wroblewski & Torres 1996). These motions are identical within their 1σ errors, so this is very likely a common-proper-motion system.

[i] WISEA J105536.09−575042.1: Using the 2MASS-to-WISE time baseline we obtain a motion, (μ_α, μ_δ), of (-196.5 ± 9.3, 128.2 ± 9.3) mas yr^{-1} for this object. The other component, UPM J1056−5750, has a published motion of (-194.4 ± 7.4, 121.9 ± 6.9) mas yr^{-1} (Finch et al. 2010). These motions are identical within their 1σ errors, so this is very likely a common-proper-motion system.

[j] WISEA J113333.67−414016.7: Using the 2MASS-to-WISE time baseline we obtain a motion, (μ_α, μ_δ), of (-152.9 ± 9.2, -120.1 ± 8.5) mas yr^{-1} for this object. The other component, CD−40 6796, has a published motion of (-169.7 ± 1.9, -117.3 ± 1.7) mas yr^{-1} (Høg et al. 2000). These motions are identical within their 2σ errors, so this is likely a common-proper-motion system.

[k] WISEA J121058.26−461204.5: Using the 2MASS-to-WISE time baseline we obtain a motion, (μ_α, μ_δ), of (101.3 ± 8.3, 167.7 ± 8.1) mas yr^{-1} for this object. The other component, CD−45 7595, has a published motion of (89.11 ± 0.40, 168.15 ± 0.47) mas yr^{-1} (van Leeuwen 2007). These motions are identical within their 2σ errors, so this is likely a common-proper-motion system.

[l] WISEA J124014.80+204752.7: Using the 2MASS-to-WISE time baseline we obtain a motion, (μ_α, μ_δ), of (205.6 ± 10.6, -369.1 ± 10.8) mas yr^{-1} for this object. The other component, BD+21 2442, has a published motion of (202.04 ± 1.44, -368.45 ± 0.99) mas yr^{-1} (van Leeuwen 2007). These motions are identical within their 1σ errors, so this is very likely a common-proper-motion system.

[m] WISEA J124726.75−434441.8: Using the 2MASS-to-WISE time baseline we obtain a motion, (μ_α, μ_δ), of (-182.0 ± 7.1, -95.4 ± 7.1) mas yr^{-1} for this object. The other component, CD−43 7881, has a published motion of (-196.60 ± 0.80, -94.31 ± 0.89) mas yr^{-1} (van Leeuwen 2007). These motions are identical within their 2σ errors, so this is likely a common-proper-motion system.

[n] WISEA J125435.54−381111.7: Using the 2MASS-to-WISE time baseline we obtain a motion, (μ_α, μ_δ), of (161.1 ± 7.9, -25.4 ± 7.8) mas yr^{-1} for this object. The other component, TYC 7772-1225-1, has a published motion of (149.6 ± 2.8, -40.1 ± 2.7) mas yr^{-1} (Høg et al. 2000). These motions are identical to within 2σ, so this could be a common-proper-motion binary. In the UCAC4 Catalog this pair has listed motions of (147.6 ± 0.7, -38.2 ± 1.0) mas yr^{-1} for the brighter component and (144.5 ± 0.8, -29.0 ± 0.8) mas yr^{-1} for the fainter component. Although the 10σ discrepancy in Decl. would seem to rule these out as a cpm pair, UCAC4 measurements can be unreliable and thus we still list this pair as a possible physical system.

[o] WISEA J134457.17−453537.2: Using the 2MASS-to-WISE time baseline we obtain a motion, (μ_α, μ_δ), of (-237.8 ± 8.0, 35.7 ± 8.0) mas yr^{-1} for this object. The other component, LTT 5330, has a published motion of (-240.51 ± 13.1, 25.99 ± 13.1) mas yr^{-1} (Röser et al. 2008). These motions are identical within their 1σ errors, so this is very likely a common-proper-motion system.

[p] WISEA J140350.20−592348.0: Using the 2MASS-to-WISE time baseline we obtain a motion, (μ_α, μ_δ), of (30.5 ± 8.7, -494.3 ± 8.5) mas yr^{-1} for this object. The other component, L 197-165, has a published motion of (33, −469) mas yr^{-1} (Luyten 1979b). The motion of the unpublished *WISE* object is identical within its 1σ errors to the R.A. motion of the Luyten object but discrepant by $\sim 3\sigma$ from the Luyten Decl. measurement. Given the large motion in Decl. and the proximity of the sources, this is still likely a common-proper-motion system.

[q] WISEA J140924.56−305534.1: Using the 2MASS-to-WISE time baseline we obtain a motion, (μ_α, μ_δ), of (-456.4 ± 8.1, -213.8 ± 8.0) mas yr^{-1} for this object. The other component, LHS 2807, has a published motion of (-460.60 ± 3.68, -219.82 ± 3.02) mas yr^{-1} (van Leeuwen 2007). These motions are identical to $<1\sigma$, so this is likely a common-proper-motion system.

[r] WISEA J142053.60−050137.8: Using the 2MASS-to-WISE time baseline we obtain a motion, (μ_α, μ_δ), of (-131.2 ± 10.2, -55.4 ± 10.0) mas yr^{-1} for this object. The other component, BD−04 3668, has a published motion of (-137.5 ± 3.5, -58.0 ± 3.2) mas yr^{-1} (Roeser & Bastian 1988). These motions are identical to $<1\sigma$, so this is likely a common-proper-motion system.

[s] WISEA J171828.99−224630.2 and WISEA J171826.98−224543.5: Using the 2MASS-to-WISE time baseline we obtain a motion, (μ_α, μ_δ), of (-149.3 ± 8.9, -149.9 ± 8.4) mas yr^{-1} for the brighter object and (-148.7 ± 8.8, -148.8 ± 8.3) mas yr^{-1} for the fainter one. These motions are identical to $<1\sigma$, so this is very likely a common-proper-motion pair.

[t] WISEA J172230.07−695119.2 and WISEA J172237.14−695112.2: Using the 2MASS-to-WISE time baseline we obtain a motion, (μ_α, μ_δ), of (-145.6 ± 10.4, -217.6 ± 8.7) mas yr^{-1} for the brighter object and (-37.6 ± 11.5, -221.9 ± 9.8) mas yr^{-1} for the fainter one. Although the (larger) Decl. motions are identical to $< 1\sigma$, the R.A. motions are discrepant by $>9\sigma$. A visual check of the system more strongly supports common proper motion than do the actual measurements. We suspect that the *WISE* astrometry for the fainter source in the pair may be corrupted by a background object—seen at nearly equal magnitude in the earlier DSS2 images—that lies near its position in the *WISE* data.

[u] WISEA J201605.71−115838.5 and WISEA J201605.96−115916.7: Both of these objects are listed in the UCAC4 Catalog, but no other literature is available. Using the 2MASS-to-WISE time baseline we obtain motions, (μ_α, μ_δ), of (-72.4 ± 8.9, -141.1 ± 7.5) mas yr^{-1} for the brighter component and (-69.4 ± 9.0, -134.4 ± 7.7) mas yr^{-1} for the dimmer component, which are identical within their 1σ errors. In the UCAC4 Catalog this pair has listed motions of (-70.9 ± 2.1, -135.6 ± 2.2) mas yr^{-1} for the brighter component and (-57.3 ± 2.1, -130.5 ± 2.1) mas yr^{-1} for the fainter component. Although the 6.5σ discrepancy in R.A. would seem to rule these out as a cpm pair, the secondary appears to be blended with another source of nearly equal magnitude in the DSS2 images. Because visual checks strongly suggest this is a co-moving system, we still list this as a possible physical pair.

[v] WISEA J210630.56−382606.1 and WISEA J210632.73−382640.4: Using the 2MASS-to-WISE time baseline we obtain a motion, (μ_α, μ_δ), of (174.9 ± 10.1, -323.4 ± 10.1) mas yr^{-1} for the brighter object and (187.1 ± 10.3, -323.3 ± 10.2) mas yr^{-1} for the fainter one. The motions are identical to $<2\sigma$, so these are likely a common-proper-motion pair.

[w] WISEA J214736.41−135335.4: Using the 2MASS-to-WISE time baseline we obtain a motion, (μ_α, μ_δ), of (151.6 ± 10.0, -300.2 ± 9.3) mas yr^{-1} for this object. The other component, Ross 208, has a published motion of (152 ± 5, -296 ± 5) mas yr^{-1} (Salim & Gould 2003). These motions are identical within $<1\sigma$, so this is very likely a common-proper-motion system.

[x] WISEA J230226.16+801241.8: Using the 2MASS-to-WISE time baseline we obtain a motion, (μ_α, μ_δ), of (-68.1 ± 9.9, 114.1 ± 9.9) mas yr^{-1} for this object. The other component, BD+79 762, has a published motion of (-53.2 ± 1.2, 127.2 ± 1.2) mas yr^{-1} (Høg et al. 2000). These motions are identical within their 2σ errors, so this is likely a common-proper-motion system.

[y] This measurement should be treated with caution because the core of this source is heavily saturated in the *WISE* images.

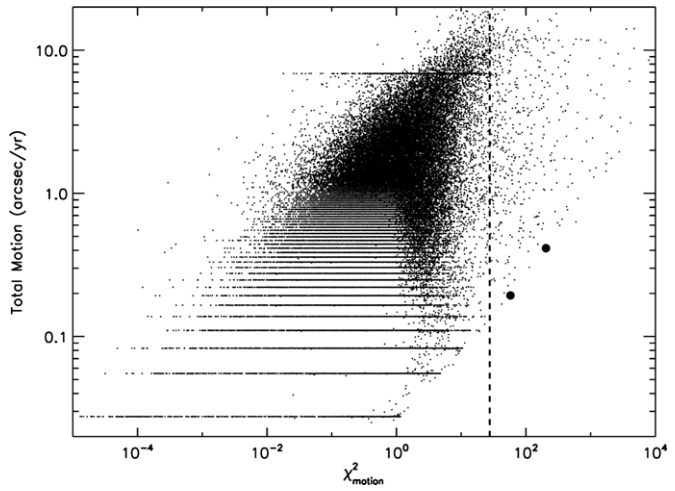

Figure 11. Total motions for sources in AllWISE Atlas Tile 0440p166_ac51 plotted as a function of χ^2_{motion}. Objects to the right of the dashed line have $\chi^2_{motion} > 27.63$ and are considered to have statistically significant motions. The previously known motion stars LTT 10950 and NLTT 9223 are shown by the larger dots. The quantized motion measures (further illustrated in the upper panel of Figure 13; see Section 3.5.1) are seen for small motion values in the lower portion of the plot, and the motion "pile-up" for spurious sources (further illustrated in the lower panel of Figure 13; see Section 3.5.2) is seen near the top of the plot at a value of 6.″875 yr^{-1}.

characterized by the Gaussian uncertainties). This limit on Q corresponds to $\chi^2_{motion} > 27.63$. Sources in this tile that satisfy this criterion are found to the right of the dashed line in Figure 11. Although a few of these objects are motion stars (see Section 3.4.2), other sources have complications that create high values of χ^2_{motion} but do not have real motions. Examples are contaminated and spurious objects flagged as such by *cc_flags*, objects with low signal-to-noise in all bands, and blended or extended sources that can often be identified by the *nb*, *w?chi2*, and *rchi2* criteria.[20] Other examples of false motion sources are given in Section 3.4.3.

3.4.2. Real Moving Sources

A total of 16 objects in Figure 11 passed additional criteria—no blending ($nb = 1$), *w?rchi2* values indicating a point source (<2.0 in all bands), and other criteria as further explained in Section 4.1. Only two of these, highlighted by larger dots in the figure, also passed a visual inspection step showing them to be point-like, unconfused, and moving (if present in data from earlier surveys). Both are previously published motion stars. The first, WISEA J025517.56+161832.7, has AllWISE measured motions in (R.A., Decl.) of (367 ± 29, 190 ± 29) mas yr^{-1} and is the known motion star LTT 10950 with published proper motions in (R.A., Decl.) of (203.09 ± 0.82, −47.76 ± 0.58) mas yr^{-1} (van Leeuwen 2007). The discrepancy in measured values is likely due more to the fact that this source is heavily saturated in AllWISE ($W1 = 5.7$ mag) rather than to parallax, which is only 37.32 ± 0.66 mas (van Leeuwen 2007). The second source, WISEA J025326.12+172429.8, has AllWISE measured motions in (R.A., Decl.) of (−55 ± 26, −185 ± 25) mas yr^{-1} and is the known motion star NLTT 9223 with published proper motions in (R.A., Decl.) of (20, −258) mas yr^{-1} (Lépine & Shara 2005). This source is also saturated in AllWISE ($W1 = 7.7$ mag), which is likely the reason for the poor agreement between AllWISE and published values.

This Tile highlights the typical success rate in finding new motion objects. Generally fewer than two dozen motion candidates are retained by the automated criteria, and only a small number survive the visual inspection step. Most of those that remain have been previously identified as motion objects by other surveys. Given that we identified 3525 new motion objects over the entire sky and that there are 18,240 Atlas Tiles total, the average Tile does not contain a new discovery.

3.4.3. False Moving Sources

False-motion sources generally fall into one of the following categories. Representative examples and their probable causes are discussed below.

1. Blended/extended sources: As in any motion survey, blended or extended objects in AllWISE create the potential for false motions. One such source is WISEA J130716.06+061032.7, an object whose AllWISE measurements indicate a significant motion of 4795 ± 471 and 2381 ± 493 mas yr^{-1} in R.A. and Decl., respectively. A very faint, extended source is seen at this position in the Sloan Digital Sky Survey (SDSS) *r* and *i* band imagery taken in 2003 (Figure 12(a)), so the source is clearly not moving at the rates indicated by AllWISE. This source is extended in the *W2* band and the photocenters at *W1* and *W2* do not align, likely giving rise to the false motion.
2. Spurious small-separation, same-tile (SSST) sources:[21] WISEAR J103558.13−370522.0 is a source in the AllWISE Reject Table with a seemingly high and statistically significant motion; AllWISE measures 3527 ± 350 and −1209 ± 119 mas yr^{-1} in R.A. and Decl., respectively. This, however, is a spurious small-separation, same-tile (SSST) source and is flagged as such by the *rel* flag in the AllWISE Reject Table. As seen in Figure 12(b), this source falls in the wings of a real object, named WISEA J103558.04−370520.9, that is found in the AllWISE Source Catalog and that has motion measures of −4 ± 44 and 27 ± 44 mas yr^{-1} in R.A. and Decl., respectively, indicating no apparent motion. Users are cautioned to pay particular attention to the *rel* flag when using motion measures from the AllWISE Reject Table.
3. Flux transients: Flux variables can sometimes trigger false motions. When an object appears at only one epoch, a nearby noise blip at the other epoch(s) may trigger a false, generally large motion. Because the derived motion is so large, it may appear to be statistically significant despite having rather large errors. An example of this is WISEA

[20] Throughout the paper, we use the shorthand "*w?chi2*" to refer to *w1chi2*, *w2chi2*, *w3chi2*, and *w4chi2*.

[21] An SSST source is part of a group of detections with unphysically small separations extracted on the same Atlas Tile and having nearly identical positions and fluxes. The false sources in these groups are created by a coding error in the AllWISE processing pipeline. The photometry routine works on detections in descending order of brightness; the intention was to process the brightest sources first so that their flux could be subtracted from the individual frames before processing fainter sources. The software error caused the flux subtraction step to be skipped in most cases. For a faint source in the wings of a brighter source, this error can cause the faint source to migrate to the flux from the brighter object because that minimizes χ^2 better than a near zero-motion solution near the faint-source detection position itself. Post-processing identified sources in these SSST groups, and the *rel* parameter was used to flag these in the Catalog and Reject Table. Sources thought to be the original, correct entries have *rel* codes of *s* or *c* and were considered for inclusion in the AllWISE Source Catalog; sources believed to be unreliable members of the SSST group were given *rel* = *r* and will be found only in the AllWISE Reject Table. Sources with *rel* = *null* are not affected by the SSST phenomenon.

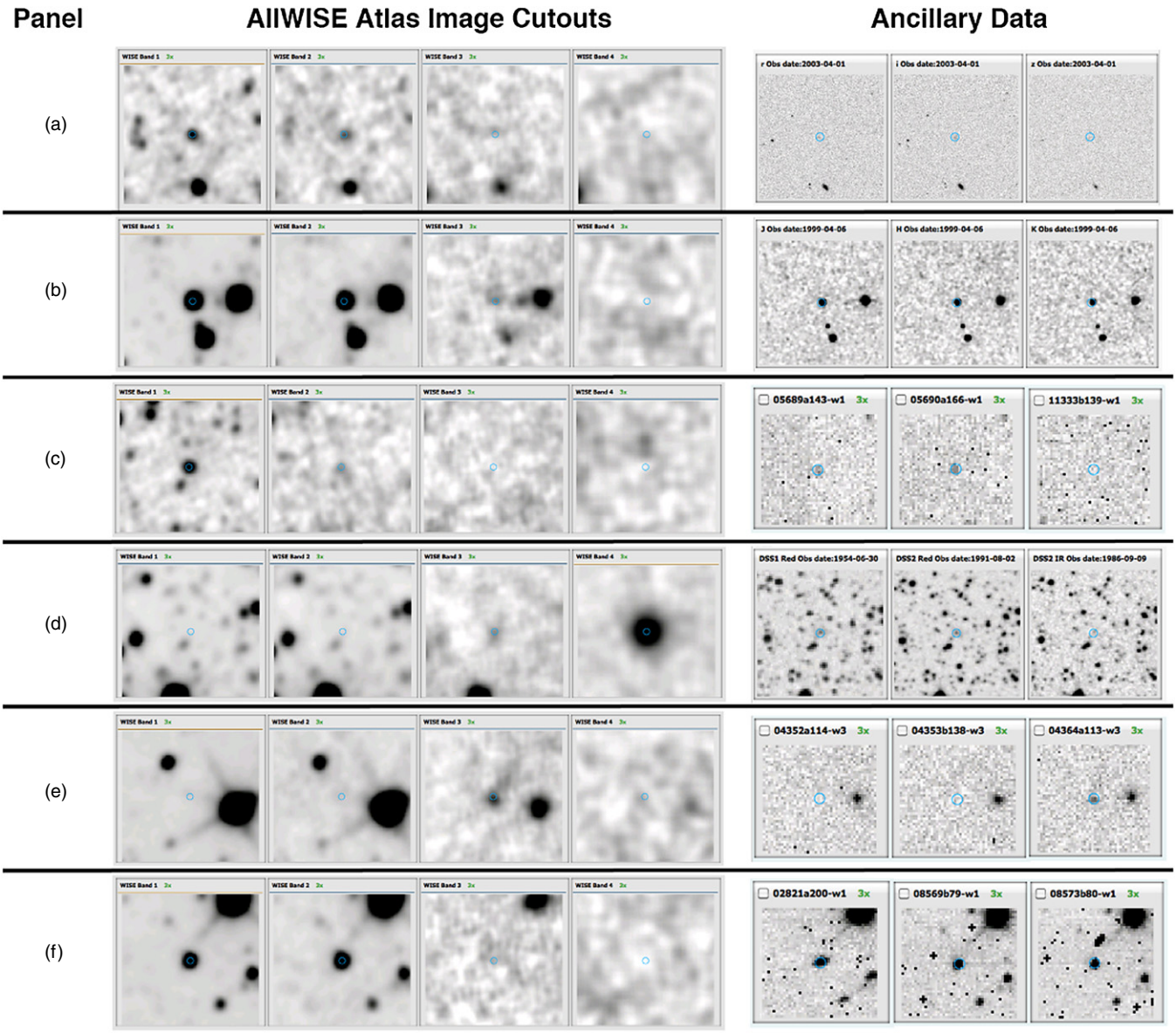

Figure 12. Seven categories of false-motion sources. The $W1$, $W2$, $W3$, and $W4$ AllWISE Atlas Image fields ($2' \times 2'$ with north up and east to the left) along with three ancillary images are shown for each example. The faint blue circle denotes the position of the AllWISE source. Ancillary images are identified as—(a) SDSS r, i, and z. Note that a faint source is seen at the AllWISE position. (b) 2MASS J, H, and K_s. Note that the blue circle is not well centered on the bright source in either the AllWISE or 2MASS images. (c) Representative *WISE* Level 1b frames at $W1$; the first two frames are from the first epoch of *WISE* observations and the third frame is from the second epoch. Note that the object is seen only at the first epoch. (d) DSS1 R and DSS2 R and I. Note that there is a faint source at the AllWISE position. (e) Three *WISE* Level 1b frames at $W3$. Note that the first two show no source at the location of the AllWISE object; the third is the only Level 1b image at this sky location showing a source at this position. (f) The only first-epoch *WISE* Level 1b image at $W1$ along with two representative second-epoch $W1$ images. Note that the first-epoch frame is significantly smeared due to spacecraft motion.

(A color version of this figure is available in the online journal.)

J122559.53+070005.2, which has AllWISE-reported motions of 24902 ± 4071 and 11567 ± 7922 mas yr^{-1} in R.A. and Decl., respectively. This object appears only in the first epoch and not the second (Figure 12(c)), as confirmed by the AllWISE Multi-Epoch Source Table, which gives a mean $w1mpro$ value of $\sim$15.3 mag for the first epoch and limits of $>$17.0 mag for the second.

4. $W3$- and $W4$-dominated sources: Sources that are detected only at $W3$ and/or $W4$ may show spurious motions. Such sources will be seen only at the earlier epochs before cryogen was exhausted and not at the later epochs when those bands were not operational. Nearby noise blips at the later epochs in $W1$ and/or $W2$ can trigger false motions. One such example is the planetary nebula PN SB 24, also known as WISEA J185716.62−175050.4 (Figure 12(d)), which has AllWISE-measured motions of 6243 ± 1101 and -11981 ± 1162 mas yr^{-1} in R.A. and Decl., respectively, despite the fact that the nebula is known to have near-zero proper motion (Kerber et al. 2008).
5. Cosmic rays in low-coverage areas: Areas having less than five frames of coverage do not reap the benefit of outlier rejection[22] in the coaddition step, so spurious sources can bleed through into the coadds. In some cases, these

[22] See http://wise2.ipac.caltech.edu/docs/release/allsky/expsup/sec4_4f.html#outrej in the WISE All-Sky Release Explanatory Supplement.

spurious sources have falsely measured, yet apparently significant, motions in AllWISE. One example is WISEA J210220.65−083948.6 (Figure 12(e)), a cosmic ray that appears in only one *W*3 frame (04364a113) in an area of sky where that *W*3 frame is the only one of acceptable quality for AllWISE processing. A nearby noise blip in another band at a different epoch nonetheless causes AllWISE to measure a large, although false, motion for it of 4573 ± 1094 and 6531 ± 1213 mas yr^{-1} in R.A. and Decl., respectively.

6. Sources falling in a streaked frame in a low-coverage area: Another consequence of low-coverage areas is the increased influence of the occasional poorer quality frame going into the coadd. The most extreme example is one in which only a single frameset is available for one of the *WISE* epochs, and that frameset has non-optimal image quality. False motions may result, as is the case for source WISEA J061658.37+701209.5 (Figure 12(f)). This object lies in an area of sky with single-frameset coverage (02821a200) at the first epoch, but this frameset is slightly smeared due to momentum dumping[23] by the spacecraft. The astrometric solution for the entire frameset is slightly biased in R.A. because of this smearing. Data at the later epoch are not affected. As a result of the mismatch in positions across epochs, a false motion of 1547 ± 129 and −5 ± 127 mas yr^{-1} in R.A. and Decl., respectively, is created. It should be noted that this is an extremely rare occurrence in AllWISE, as Quality Assurance flagged almost all of the smeared frames and eliminated them from consideration for coaddition. Nonetheless, users are advised to treat with caution any motion measures in areas of low-coverage at a single epoch.

3.5. Other Caveats

3.5.1. Motion Measurements are Quantized

A plot of AllWISE motion measurements in a single Atlas Tile (upper panel of Figure 13) shows that certain, discrete values have a higher frequency of occurrence. The solution for motion values and source positions is an iterative process whereby a minimization of χ^2 is sought in the phase space of source position and motion. Convergence is rapidly achieved for position estimates, using initial values. On the other hand, convergence on motion values is achieved only after one or more iterative steps. The step size used for motion estimates is 27.5 mas yr^{-1}, and converged motion values are thus quantized at multiples of this value.[24]

3.5.2. Spurious Motion Measurements Show "Pile-up" at Large Values

A total motion value of 6875 mas yr^{-1} is often seen for spurious sources in AllWISE. The "pile-up" of motion measures at this value is illustrated in the lower panel of Figure 13. The algorithm for minimization of χ^2 has a maximum number of iterations of 250. Each iteration step for motion uses, as stated above, a step size of 27.5 mas yr^{-1}. A spurious or pure-noise solution that has not converged after the maximum number of steps will lead to a motion at the "pile-up" value[25] of 6875 mas yr^{-1}.

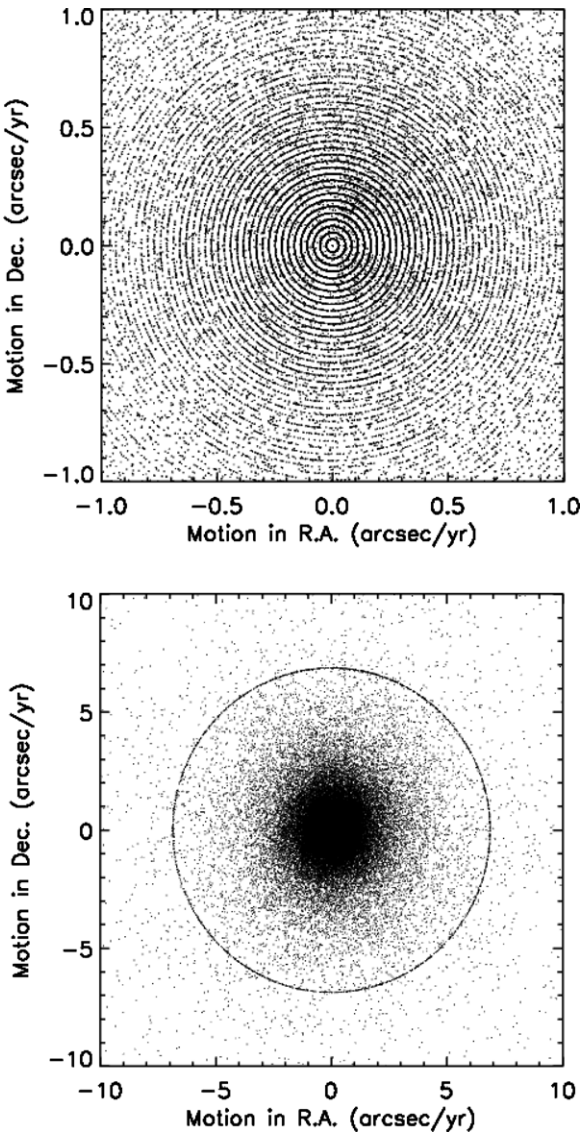

Figure 13. Plots of the AllWISE-measured motions in R.A. plotted against the AllWISE-measured motions in Decl. for a typical Atlas Tile (1174p075_ac51). (Upper panel) A zoom-in showing motion quantization at small values. (Lower panel) A zoom-out showing the motion "pile-up" at a value of 6.″875 yr^{-1}.

4. A CATALOG OF MOTION DISCOVERIES

4.1. Criteria for Selecting Motion Candidates

As part of AllWISE pipeline processing at IPAC, the Quality Assurance code filtered the list of detections from each Atlas Tile to identify objects believed to be moving significantly. These criteria were used to select only the choicest motion objects from the source lists and to keep the number of candidates manageable on the tight schedule allotted for AllWISE Quality Assurance checks. The criteria used are as follows.

1. To ensure that the object is not flagged as an artifact, the *cc_flags* parameter was required not to have a capital-letter

[23] See http://wise2.ipac.caltech.edu/docs/release/allwise/expsup/sec4_2.html#torque in the AllWISE Explanatory Supplement.

[24] See http://wise2.ipac.caltech.edu/docs/release/allwise/expsup/sec5_3bii.html#gradient-descent_algo in the AllWISE Explanatory Supplement for further information.

[25] See http://wise2.ipac.caltech.edu/docs/release/allwise/expsup/sec5_3bii.html#effect_noise_motion_solution in the AllWISE Explanatory Supplement for more details.

value at any position in its four-character code, in which the four characters refer to the four *WISE* bands. Capital letters are used when the software has determined in that band that the object was a spurious detection of either a diffraction ("D") spike, a scattered light halo ("H") surrounding a bright star, an optical ("O") ghost image, or persistence ("P")—i.e., a short-term latent image—left behind by a bright source on the detector. Values of *cc_flags* having only lower-case versions of these same letters (indicating that the object is likely real and only contaminated by an artifact) or zero (indicating that the source is unaffected by known artifacts) were allowed.

2. To ensure that the object is point-like, a value of $nb = 1$ (no blends) was required. Also, the motion-fit, reduced χ^2 values in all bands, $w?rchi2\_pm$, were required to be less than two to eliminate sources that are obviously extended.
3. To eliminate more poorly measured sources from consideration, the signal-to-noise ratio, $w?snr$, was required to be greater than seven in at least one band.
4. To ensure that the code selected only those objects with robust and statistically significant motions, the following criteria were applied: (a) The ratio of the reduced χ^2 value between the stationary and motion fit, $rchi2/rchi2\_pm$, was required to be greater than 1.03. This ensures that the motion-fit solution significantly improves the overall reduced χ^2 value compared to the stationary fit. (b) As explained in Section 3.4 above, the $\chi^2_{\rm motion}$ criterion was required to be greater than 27.63 to select only those objects with statistically significant motions. (c) The second and third characters of *pmcode* were required to be "N" and "0," respectively. A value of "N" means that no blend-swapping has occurred and a value of "0" means that the offset between the stationary-fit and the motion-fit position at the mean epoch is less than 1″. These values were chosen because blended sources often have blend swapping, and spurious sources often have unphysically large positional differences at the mean epoch between the non-motion and motion solutions.[26]
5. To ensure that the motion measurement has a solid foundation of $W1$- and $W2$-band data underlying it, we experimented with various values of $w1m$, $w2m$, and $w1mJDmax - w1mJDmin$. The first two parameters specify the number of frames in $W1$ and $W2$, and the third parameter specifies the time difference between the earliest and latest frames in $W1$. In the end, these parameters were all set to be greater than zero because regions of very sparse coverage were found not to contribute a large number of spurious motion sources, mainly because the vast majority of the sky is well covered across two or more epochs.

These criteria were written to eliminate blended/extended sources, spurious objects, and pure noise. Other contaminants listed in Section 3.4.3—the SSST sources, flux transients, $W3$- and $W4$-dominated sources, and cosmic rays and streaked frames in low coverage areas—were discovered as a result of these Quality Assurance checks. These contaminants were generally easy to recognize via a visual inspection step, which displayed images of the field in the AllWISE $W1$, $W2$, $W3$, and $W4$ coadds along with Two Micron All Sky Survey (2MASS) images at J, H, and K_s. For *WISE* objects that were also visible in 2MASS, which represents the vast majority of sources identified, any motion should be obvious in the 10+ yr between the 2MASS and *WISE* image sets.[27] The Quality Assurance scientists checked these images for all candidate motion objects and retained only those objects having no 2MASS source at the AllWISE position.

4.2. Vetting the List of Candidates

The Quality Assurance scientists (J.D.K. and S.F.A.) produced a list of 26,850 candidates as a result of the criteria filtering and image checking discussed above. This list was then run (by J.D.K.) through SIMBAD using a 2′ search radius around the AllWISE position to search for previously known objects. If SIMBAD noted a proper motion source within 10″ of the AllWISE position, the object was eliminated from the list.[28] When known proper motion sources were found outside of 10″, the AllWISE- and SIMBAD-reported motions were checked to see if the object was a very high-motion source, generally $>1''\,{\rm yr}^{-1}$. This further check eliminated many known, small-numbered LHS (Luyten Half Second) objects.

The remaining list of objects was then checked (by J.D.K.) against the Fourth US Naval Observatory CCD Astrograph Catalog[29] (UCAC4; Zacharias et al. 2013) using a 1′ search radius. Objects with significant UCAC4-reported motions were considered to be possible matches to the AllWISE source. The match was considered confirmed if the UCAC4 source appeared to have a motion of the right magnitude and in the correct direction, as inferred from visual inspection of the motion source across the DSS2, 2MASS, and *WISE* images, to be the AllWISE-selected object. Those objects matching a source with reliable motions in UCAC4 were flagged as such but kept in the object list because they have no SIMBAD entries.

After these checks, the list was run again through SIMBAD and further checked against DwarfArchives.org, against a list of published papers (on low-mass objects) likely not to have been ingested into SIMBAD by 2013 December, and against catalogs housed by VizieR. These checks (by G.N.M. and A.S.) enabled us to eliminate other objects. Objects were kept in the list only when SIMBAD had no reported proper motion information and no links to published papers citing a proper motion value. Thus, a few objects with published spectral types are included in the list because this will be the first refereed publication in SIMBAD giving their motion information. Objects listed only in UCAC4 and other catalogs found in VizieR are noted as such in the final list.

Of the 26,850 motion candidates selected by our Quality Assurance criteria, we found that 18,862 objects (70%) were already published and had motion information available in SIMBAD. Of the remainder, 3583 objects (13%) are new discoveries and 4405 objects (16%) were found to be non-motion sources after visual inspection of the DSS2 images.

The discovery list of 3583 itself is comprised of two sublists. The first (Table 3) contains 3525 objects whose motions could be confirmed using non-*WISE* data, and the second (Table 4) contains 58 unconfirmed objects lacking counterparts in earlier surveys. For the list of confirmed objects, one of us (A.S.)

[26] See http://wise2.ipac.caltech.edu/docs/release/allwise/expsup/sec2_1a.html#pmcode in the AllWISE Explanatory Supplement.

[27] Because the smallest motion measurable with AllWISE is $\sim 0''.15\,{\rm yr}^{-1}$ (Section 3.2.2), this means that objects will have moved $>15''$ in the 10+ yr between the 2MASS and *WISE* imaging sets, which is a sufficiently large motion to be obvious by eye.

[28] Roughly speaking, a circle of radius 10″ around the AllWISE J2000 position at epoch 2010.54 will capture all SIMBAD motion objects, reported using their J2000 positions and epoch 2000.00, moving less than $\sim 1''\,{\rm yr}^{-1}$.

[29] Available at http://irsa.ipac.caltech.edu.

Table 3
AllWISE Motion Discoveries

WISEA Designation	2MASS J (mag)	2MASS H (mag)	2MASS K_s (mag)	$W1$ (mag)	$W2$ (mag)	AllWISE R.A. Motion (mas yr^{-1})	AllWISE Decl. Motion (mas yr^{-1})	Computed μ_α[a] (mas yr^{-1})	Computed μ_δ[a] (mas yr^{-1})	Flag[b]	Note[c]
(1)	(2)	(3)	(4)	(5)	(6)	(7)	(8)	(9)	(10)	(11)	(12)
J000136.86−010146.9	12.363 ± 0.021	11.831 ± 0.020	11.565 ± 0.021	11.374 ± 0.022	11.202 ± 0.021	−166 ± 49	−378 ± 48	−38.5 ± 11.4	−233.1 ± 10.5	0	0
J000138.90−761350.1	9.477 ± 0.021	8.893 ± 0.024	8.603 ± 0.023	8.460 ± 0.023	8.374 ± 0.020	284 ± 30	−170 ± 32	241.2 ± 17.1	−16.7 ± 7.7	0	0
J000205.60−322545.9	14.079 ± 0.026	13.472 ± 0.036	13.216 ± 0.037	13.085 ± 0.024	13.023 ± 0.026	0 ± 74	0 ± 73	23.8 ± 10.1	42.0 ± 9.8	0	0
J000234.41+470030.9	10.288 ± 0.019	9.714 ± 0.030	9.468 ± 0.021	9.311 ± 0.023	9.276 ± 0.021	−69 ± 31	−202 ± 30	−93.4 ± 9.7	−107.1 ± 9.5	1	0
J000239.96+612015.0	12.709 ± 0.028	12.059 ± 0.031	11.728 ± 0.021	11.558 ± 0.023	11.390 ± 0.021	201 ± 28	92 ± 27	222.8 ± 9.2	68.5 ± 9.1	0	0
J000416.30−605925.3	11.359 ± 0.021	10.842 ± 0.022	10.636 ± 0.021	10.515 ± 0.022	10.416 ± 0.020	−258 ± 36	−218 ± 35	−228.3 ± 9.8	−213.8 ± 9.8	1	0
J000533.57+280705.8	14.073 ± 0.022	13.489 ± 0.033	13.186 ± 0.031	12.975 ± 0.024	12.702 ± 0.026	−355 ± 65	−346 ± 66	−205.1 ± 11.9	−264.8 ± 10.0	1	1
J000622.67−131955.6	16.674 ± 0.125	15.548 ± 0.105	15.115 ± 0.126	14.239 ± 0.027	13.754 ± 0.042	−416 ± 123	−852 ± 128	−239.2 ± 17.3	−413.2 ± 16.3	2	0
J000915.71−285019.7	14.744 ± 0.035	14.143 ± 0.042	13.800 ± 0.045	13.624 ± 0.026	13.435 ± 0.033	44 ± 101	−229 ± 103	86.2 ± 11.2	32.0 ± 10.9	0	0
J001102.05−421417.7	10.903 ± 0.021	10.37 ± 0.026	10.094 ± 0.021	9.912 ± 0.022	9.774 ± 0.019	−399 ± 37	−190 ± 36	−248.9 ± 11.1	−40.6 ± 9.4	1	0

Notes.
[a] This is the motion measured between the 2MASS and *WISE* epochs.
[b] If the source is a motion discovery unique to AllWISE, Flag = 0. If the only prior literature is an entry with similar motion in the UCAC4 Catalog or other VizieR catalog holding not incorporated into SIMBAD, Flag = 1. If the object appears only in the Luhman (2014) list, Flag = 2. If the object appears both in the Luhman (2014) list *and* in a prior catalog not incorporated into SIMBAD, Flag = 3.
[c] If there is an additional note about this source at the end of the table, Note = 1.

(This table is available in its entirety in a machine-readable form in the online journal. A portion is shown here for guidance regarding its form and content.)

Table 4
AllWISE Motion Candidates Lacking 2MASS Counterparts[a]

WISEA Designation	$W1$ (mag)	$W2$ (mag)	AllWISE R.A. Motion (mas yr^{-1})	AllWISE Decl. Motion (mas yr^{-1})	Flag[b]	Note[c]
(1)	(2)	(3)	(4)	(5)	(6)	(7)
J001152.64−202826.4	16.443 ± 0.072	15.261 ± 0.093	−8857 ± 686	16150 ± 720	0	0
J001449.42−055522.7	16.313 ± 0.073	16.217 ± 0.233	5931 ± 929	8629 ± 936	1	0
J003314.92−465936.0	16.094 ± 0.051	15.612 ± 0.095	−8412 ± 436	4870 ± 442	1	0
J003647.68−122155.3	15.863 ± 0.054	15.522 ± 0.124	−6302 ± 619	−1310 ± 572	1	0
J005429.43−595619.9	16.237 ± 0.057	15.772 ± 0.118	−2302 ± 570	4102 ± 547	0	0
J005519.24−491935.3	16.196 ± 0.057	16.069 ± 0.153	5645 ± 552	2333 ± 557	1	0
J005853.15−555722.4	15.540 ± 0.038	15.628 ± 0.099	5248 ± 349	826 ± 327	1	0
J010133.97−551653.9	17.206 ± 0.122	15.587 ± 0.099	−8224 ± 861	9173 ± 886	0	0
J010213.98−344757.7	16.059 ± 0.050	15.145 ± 0.069	1864 ± 454	5155 ± 486	0	0
J010309.96−151101.0	15.484 ± 0.042	15.500 ± 0.109	−4098 ± 363	1027 ± 384	1	0
J011133.57−412722.5	16.359 ± 0.058	16.203 ± 0.148	−19976 ± 722	13761 ± 761	1	0
J011759.72−281749.6	15.494 ± 0.039	15.399 ± 0.091	−1752 ± 381	3048 ± 369	1	0
J012122.26−110214.0	16.910 ± 0.115	15.257 ± 0.095	−2373 ± 735	5624 ± 805	0	0
J012255.66−223007.0	15.197 ± 0.035	14.886 ± 0.067	−1465 ± 279	226 ± 281	1	0
J014224.00−361822.7	16.046 ± 0.050	15.584 ± 0.098	−447 ± 457	−5412 ± 442	1	0
J014446.74−203855.3	16.205 ± 0.063	15.607 ± 0.128	6287 ± 626	2423 ± 661	1	0
J014507.92−355631.8	16.139 ± 0.053	15.915 ± 0.123	3276 ± 485	−633 ± 492	1	0
J014804.04−712828.3	16.360 ± 0.051	15.072 ± 0.053	−1697 ± 428	−3448 ± 394	0	0
J020801.13−161630.1	16.020 ± 0.055	15.991 ± 0.152	−3994 ± 489	11866 ± 588	1	0
J020812.38−275731.9	16.617 ± 0.072	16.350 ± 0.191	−9498 ± 602	−185 ± 616	1	0
J024519.98+134918.6	16.130 ± 0.060	15.977 ± 0.154	3028 ± 307	1042 ± 333	1	0
J025246.35−262919.1	16.385 ± 0.059	16.346 ± 0.161	−52 ± 329	−4234 ± 340	1	0
J031159.56−195310.6	15.970 ± 0.043	15.421 ± 0.082	−919 ± 229	5174 ± 229	0	0
J031303.91−453358.2	15.359 ± 0.034	15.389 ± 0.071	−1661 ± 152	510 ± 155	1	0
J032307.25−364432.4	15.885 ± 0.042	15.661 ± 0.094	1023 ± 196	−3686 ± 194	1	0
J033231.23−245841.9	16.376 ± 0.054	16.078 ± 0.133	−3320 ± 288	−2582 ± 307	1	0
J034803.93−354036.0	16.058 ± 0.043	15.580 ± 0.075	−1593 ± 196	−4013 ± 197	0	0
J053133.00−304416.7	15.447 ± 0.038	15.710 ± 0.100	−1246 ± 335	−2708 ± 340	1	0
J053509.97−313855.9	16.344 ± 0.061	16.244 ± 0.181	2027 ± 749	−4774 ± 788	1	0
J054631.32−311749.1	15.921 ± 0.048	15.706 ± 0.108	−1959 ± 556	3282 ± 619	1	0
J055034.35−363805.8	15.806 ± 0.044	15.291 ± 0.076	−3399 ± 394	−2114 ± 430	0	0
J055202.16−534725.1	16.253 ± 0.043	16.068 ± 0.095	3637 ± 433	1876 ± 467	1	0
J055537.68−175339.9	16.019 ± 0.053	15.611 ± 0.107	3813 ± 545	2242 ± 596	1	0
J055658.63−140702.8	15.367 ± 0.040	15.230 ± 0.078	−914 ± 344	−2203 ± 364	1	0
J065959.23+780829.9	15.600 ± 0.039	15.223 ± 0.068	−782 ± 330	−2872 ± 367	0	0
J085510.74−071442.5	16.231 ± 0.064	13.704 ± 0.033	−4188 ± 267	226 ± 283	2	1
J105042.60+140202.3	17.124 ± 0.138	15.568 ± 0.124	−1521 ± 800	−13560 ± 912	0	0
J111202.32+324123.7	17.128 ± 0.112	16.658 ± 0.268	5648 ± 591	5618 ± 630	0	0
J113654.49−201658.7	15.766 ± 0.046	15.718 ± 0.159	3239 ± 407	−4756 ± 441	1	0
J121607.98+191003.1	15.926 ± 0.055	15.313 ± 0.103	6708 ± 519	−4289 ± 562	1	0
J121903.27−084702.2	16.200 ± 0.067	16.594 ± 0.283	−3987 ± 637	−1822 ± 703	1	0
J125728.42+464457.6	16.574 ± 0.075	15.911 ± 0.135	6348 ± 519	−2077 ± 543	1	0
J130825.50+331256.1	15.736 ± 0.044	15.265 ± 0.074	−6619 ± 288	−2636 ± 321	1	0
J131302.32+030607.4	17.254 ± 0.144	>16.918	−1975 ± 537	−6980 ± 618	0	0
J134115.18+280218.5	17.410 ± 0.140	>16.837	−3137 ± 676	10163 ± 776	0	0
J144817.44+490631.2	16.053 ± 0.046	15.364 ± 0.073	5177 ± 330	−1900 ± 357	0	0
J151813.45+311515.8	17.376 ± 0.103	16.311 ± 0.146	7908 ± 378	−814 ± 413	0	1
J163139.17−244942.7	13.245 ± 0.026	11.004 ± 0.021	−235 ± 64	−548 ± 69	0	1
J174254.29+761729.7	15.997 ± 0.036	15.280 ± 0.047	−2100 ± 328	−2899 ± 342	0	0
J180512.73+321459.3	16.275 ± 0.057	14.869 ± 0.051	−2713 ± 507	3013 ± 566	0	0
J185818.21+804757.5	15.806 ± 0.036	15.556 ± 0.066	−1552 ± 304	−2236 ± 328	0	0
J191837.08+833036.5	15.891 ± 0.038	15.773 ± 0.078	3143 ± 359	817 ± 380	1	0
J203712.92−071456.2	16.198 ± 0.064	14.563 ± 0.056	−1541 ± 297	2346 ± 289	0	0
J205029.36−344817.4	16.044 ± 0.056	14.761 ± 0.063	2486 ± 457	1839 ± 470	0	0
J225750.96−440429.5	16.398 ± 0.055	16.842 ± 0.257	−11280 ± 550	11280 ± 596	1	0
J230744.88−200218.5	15.295 ± 0.040	15.455 ± 0.125	−2117 ± 365	6388 ± 375	1	0
J232558.27−135406.6	16.645 ± 0.089	16.629 ± 0.307	−2993 ± 961	17804 ± 962	1	0
J232822.75−385208.8	16.079 ± 0.057	15.582 ± 0.111	−1229 ± 524	−3938 ± 527	1	0

Notes.
[a] Most of the objects in this list are believed not to be actual motion sources. See the text for details.
[b] If the source is a motion discovery unique to AllWISE, Flag = 0. If this source is believed to be a flux transient and not a motion object because of its blue $W1 - W2$ color, Note = 1. If the object appears in Luhman (2014), Flag = 2.
[c] If there is an additional note about this source at the end of the table, Note = 1.
WISEA J085510.74−071442.5: This object is 28″ from the radio source 3C 209, which has the identifier WISEA J085509.46−071502.9. Although the *WISE* imaging data show a clear photocentric shift between the two epochs of data, additional imaging is needed to confirm the motion measure. WISEA J151813.45+311515.8: Brightest in $W3$ band (11.073 ± 0.097 mag) but also faintly visible at $W1$ and $W2$. WISEA J163139.17−244942.7: May correspond to the embedded, sub-mm source JCMTSE J163138.6−244950 in the ρ Oph star formation complex.

consulted the 2MASS images to find the *WISE* source at the 2MASS epoch and then tabulated the 2MASS position and magnitudes from the 2MASS All-Sky Point Source Catalog. These 2MASS associations were then double checked (by J.D.K.) by creating finder charts of DSS, 2MASS and *WISE* images centered at the position of the 2MASS source. Using these associations, a proper motion was measured for each source using the 2MASS position as the first epoch and the mean WISE All-Sky Source Catalog position as the second epoch.

Because the identification of motion candidates during Quality Assurance took place before selection of objects for the AllWISE Source Catalog (and before the SSST phenomenon was fully recognized), we had to retroactively replace a small number of our motion candidates that appeared only in the AllWISE Reject Table with their more appropriate entry from the AllWISE Source Catalog. In some cases, the entry in the AllWISE Source Catalog does not have a motion significant enough to have been selected by the Quality Assurance criteria. We retain such cases if our independent checks using the 2MASS-to-WISE time baseline confirm that the objects are truly moving. An example of this is WISEA J000205.60−322545.9, which has AllWISE motions of 0 ± 74 and 0 ± 73 mas yr^{-1} in R.A. and Decl., respectively, but whose comparison with the earlier 2MASS position confirms a motion of 23.8 ± 10.1 and 42.0 ± 9.8 mas yr^{-1} in R.A. and Decl. This motion is too small to have been legitimately uncovered by AllWISE, but we list it nonetheless as a serendipitous discovery.

The sky distribution of the confirmed motion objects is shown in Figure 14. The top panel shows the ecliptic projection that is the natural system for the *WISE* scanning pattern. The three-epoch coverage areas[30] at ecliptic longitudes of ∼25°–48° and ∼200°–223° are, as expected, seen as overdensities. An underdensity in the number of motion objects is seen toward the Galactic Center and along the Galactic mid-plane (bottom panel of Figure 14), as expected in these regions of source confusion and high backgrounds.

The sky distribution of the confirmed objects is compared in Figure 15 to the New Luyten Two Tenths Catalog (NLTT; Luyten 1979b), a large compilation of motion objects covering the entire sky. As expected, the majority of new discoveries (middle panel of Figure 15) falls primarily in the southern hemisphere because the NLTT is much less complete in those regions (top panel of Figure 15). The clumpiness of these discoveries in the southern hemisphere (e.g., at $11^h < \text{R.A.} < 22^h$ and Decl. $< -0°$) is largely a consequence of the *WISE* three-epoch coverage (middle panel of Figure 14) overlapping areas poorly covered by the NLTT.

4.3. The Motion Catalog

The list of all 3525 confirmed AllWISE motion objects is given in Table 3. Column 1 gives the source designation from the AllWISE Source Catalog. Columns 2–4 give the 2MASS J, H, and K_s magnitudes and associated errors of the source, and Columns 5 and 6 give the AllWISE $W1$ and $W2$ profile-fit magnitudes and errors. Columns 7 and 8 give the AllWISE-measured motions in R.A. and Decl. whereas Columns 9 and 10 give the proper motions computed using the 2MASS-to-WISE time baseline. Column 11 is a flag column indicating whether the source has an entry in another motion catalog, even though the source itself has no publication history, and Column 12 indicates whether additional information is available in the footnotes.

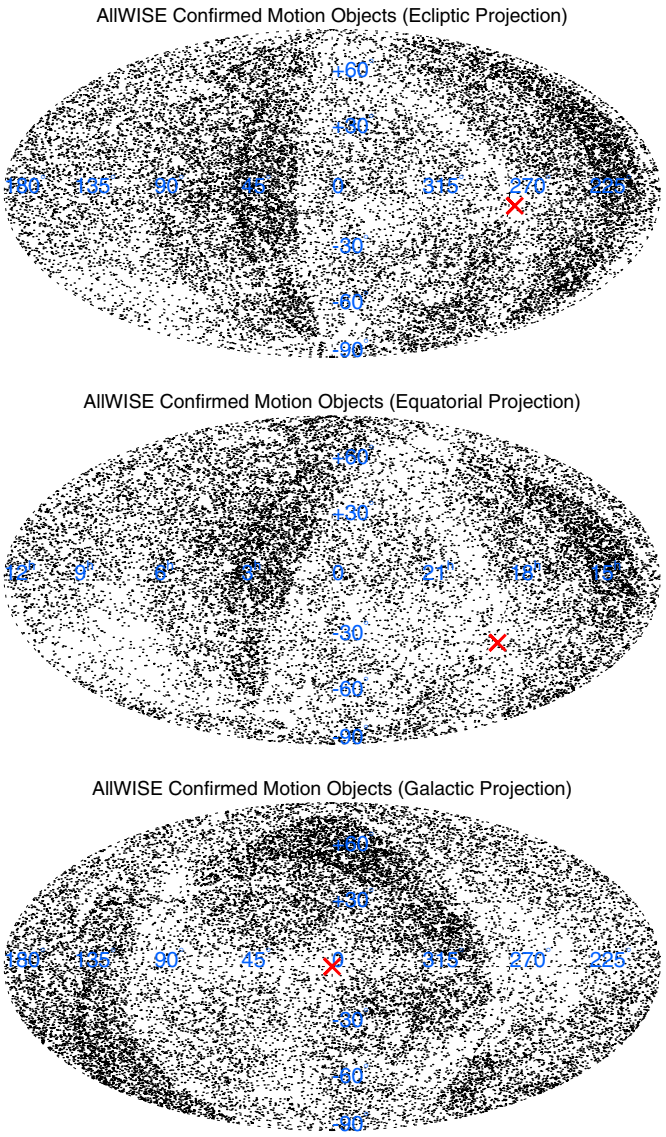

Figure 14. All-sky maps showing the locations of the 22,387 confirmed motion objects identified in AllWISE. Of these, 18,862 are rediscoveries whose motions are given in SIMBAD and the other 3525 are new discoveries from Table 3. The projections shown are (top) ecliptic, (middle) equatorial, and (bottom) Galactic. A red "X" marks the location of the Galactic Center.

(A color version of this figure is available in the online journal.)

The 58 AllWISE motion candidates lacking counterparts in 2MASS and other earlier surveys are listed in Table 4. Sixty percent of the objects in this table (35 out of 58) are believed to be flux transients based on their blue $W1-W2$ colors and appearance on the WISE All-Sky Release and AllWISE Release Atlas Images. These objects are slightly fainter versions of objects clearly seen in the $W1$ individual frames at one, and only one, *WISE* epoch, but because of their faintness, the variability cannot be confirmed by eye using the individual frames. Most of the remaining 40% of the objects may or may not be real motion objects. One of these, WISEA J085510.74−071442.5, was also found by Luhman (2014), and the AllWISE motion values of -4188 ± 267 and 226 ± 283 mas yr^{-1} in R.A. and Decl., respectively, match well with his measures of -4800 ± 300 and

[30] See the depth-of-coverage sky map (Figure 5) in Section IV.2 of the AllWISE Explanatory Supplement at http://wise2.ipac.caltech.edu/docs/release/allwise/expsup/sec4_2.html.

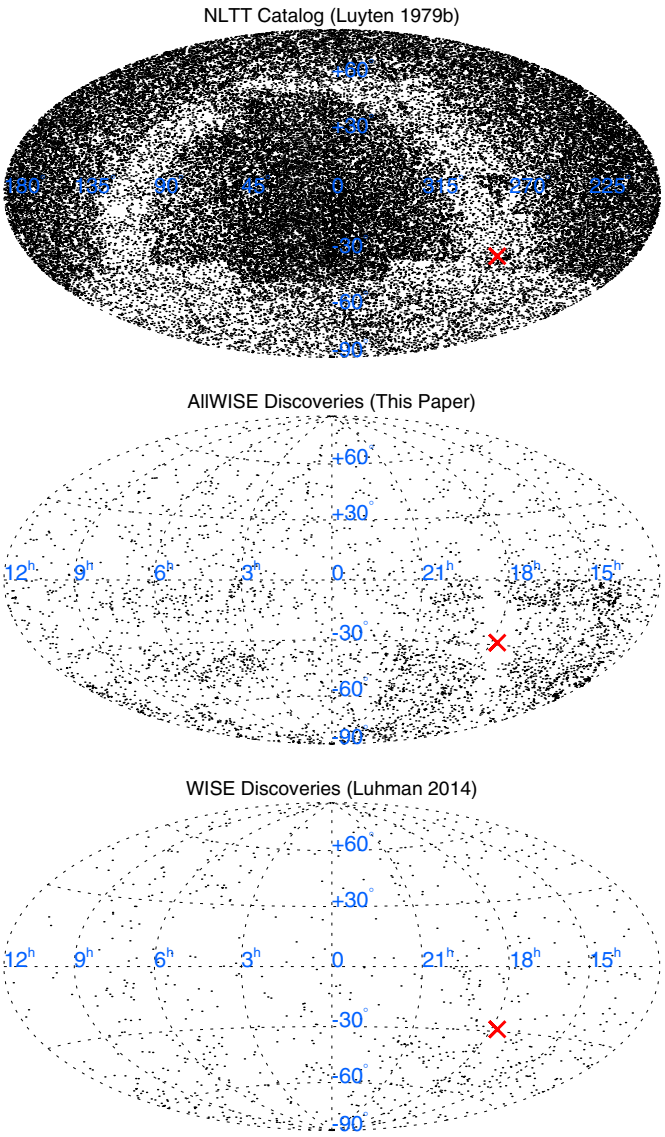

Figure 15. All-sky maps showing the locations of (top) the 58,845 motion objects from the New Luyten Two Tenths Catalog (Luyten 1979b), (middle) the 3525 motion objects from Table 3 of this paper, and (bottom) the 762 motion objects from Luhman (2014). These are equatorial coordinate projections with the vernal equinox at the center and R.A. increasing to the left. A red "X" marks the location of the Galactic Center.

(A color version of this figure is available in the online journal.)

500 ± 300 mas yr^{-1} as expected, since these motions are derived from the same data set. Visual inspection of the individual frames also strongly suggests a large motion between the two *WISE* epochs, but we nonetheless list this source as unconfirmed pending a third-epoch verification.

The next set of plots aim to characterize objects in Table 3. Figure 16 shows the AllWISE-measured motions plotted against the 2MASS-to-WISE motions. Careful analysis of the left and middle panels of this plot shows that, unlike the truth-test cases in Figure 6, the points do not fall along the line of one-to-one correspondence but rather would have a fitted slope much steeper than the one-to-one line. The reason for this is an inherent bias in our selection criteria. By demanding that the motion value be statistically significant compared to its measured errors means that at a given value of R.A. or Decl. motion we preferentially select those that are measured on the high side of the average rather than on the low side. This effect is also seen in the right panel of Figure 16. As expected given this bias, the AllWISE-measured motions tend to be higher than those measured independently.

Figure 17 shows the AllWISE $W1$ profile-fit magnitude of each source plotted against the total motion computed from the 2MASS-to-WISE time baseline. As can be seen on the figure, 10 of these objects have motions $\geqslant$1000 mas yr^{-1}, including the three highest movers WISEA J204027.30+695924.1 ($\mu = 2300 \pm 10$ mas yr^{-1}; see Section 7), WISEA J154045.67−510139.3 ($\mu = 2006 \pm 12$ mas yr^{-1}; see Section 8), and WISEA J070720.50+170532.7 ($\mu = 1802 \pm 15$ mas yr^{-1}; Wright et al. 2013).

Figure 18 shows the 2MASS J-band magnitude plotted as a function of the $J-W2$ color. As shown in Figure 7 of Kirkpatrick et al. (2011), L and T dwarfs generally have colors of $J-W2 > 2.0$ mag, so the list of AllWISE motion objects contains approximately 30 new L and T dwarfs. Figure 19 (which can be compared to Figure 9 in Kirkpatrick et al. 2011) breaks the degeneracy between the L and T dwarf populations. Figure 1 of Kirkpatrick et al. (2011) shows that the break between the L and T dwarf populations is near $W1-W2 = 0.6$ mag, which means that of the ∼30 new L and T dwarfs, only three are red enough to be T dwarfs themselves. These objects are WISEA J011154.36−505343.4, WISEA J210529.11−623559.3, and WISEA J212100.87−623921.6, all of which lack previous publication, likely because their very southern declinations have made follow-up somewhat more difficult.

None of these objects is nearly red enough to fall in the Y dwarf regime, which falls very roughly at $W1-W2 > 3.5$ mag. It is natural, then, to ask why the AllWISE motion survey wasn't more efficient at picking up T and Y dwarfs. There are two reasons. First, the apparent magnitudes of the nearest T and Y dwarfs are sufficiently faint that AllWISE would only have been able to measure significant motions for the very fastest movers (see Figure 5). Second, several bright, very high motion T and Y dwarfs *were* picked up by our criteria, but these are not included in Table 3 because they were previously known. In fact, it is hard to imagine a bright, nearby T or Y dwarf that would not have been picked up via color selection because, after all, *WISE* was designed to be highly sensitive to the methane absorption that defines these spectral types. With longer time baselines, *WISE*-like data would be able to probe deeper magnitude limits and smaller motions, enabling the discovery of fainter and/or colder objects than color selection itself can provide. Although it is possible that AllWISE has identified a moving $W2$-only source with a $W1 - W2$ color limit sufficiently marginal that color-based criteria would not have selected it, our current motion-based criteria did not extract it. Modifying the selection criteria will be further discussed in Section 5.

Finally, we present two plots that help to isolate potentially low-metallicity objects. Figure 20 shows the reduced proper motion at J band plotted against the $J-W2$ color. The reduced proper motion can be thought of as a poor man's substitute for an absolute magnitude measurement when a parallax is lacking. In the distance modulus equation, the total proper motion is used in place of the parallax (this is done because, to first order, the higher an object's proper motion, the larger its parallax is likely to be) and the "absolute magnitude" that results is called the reduced proper motion. At J band, this would be written as $H_J = J + 5\log(\mu) + 5$, where μ is expressed in arcsec yr^{-1} and the reduced proper motion is in magnitudes. Objects with abnormally high space velocities confound this

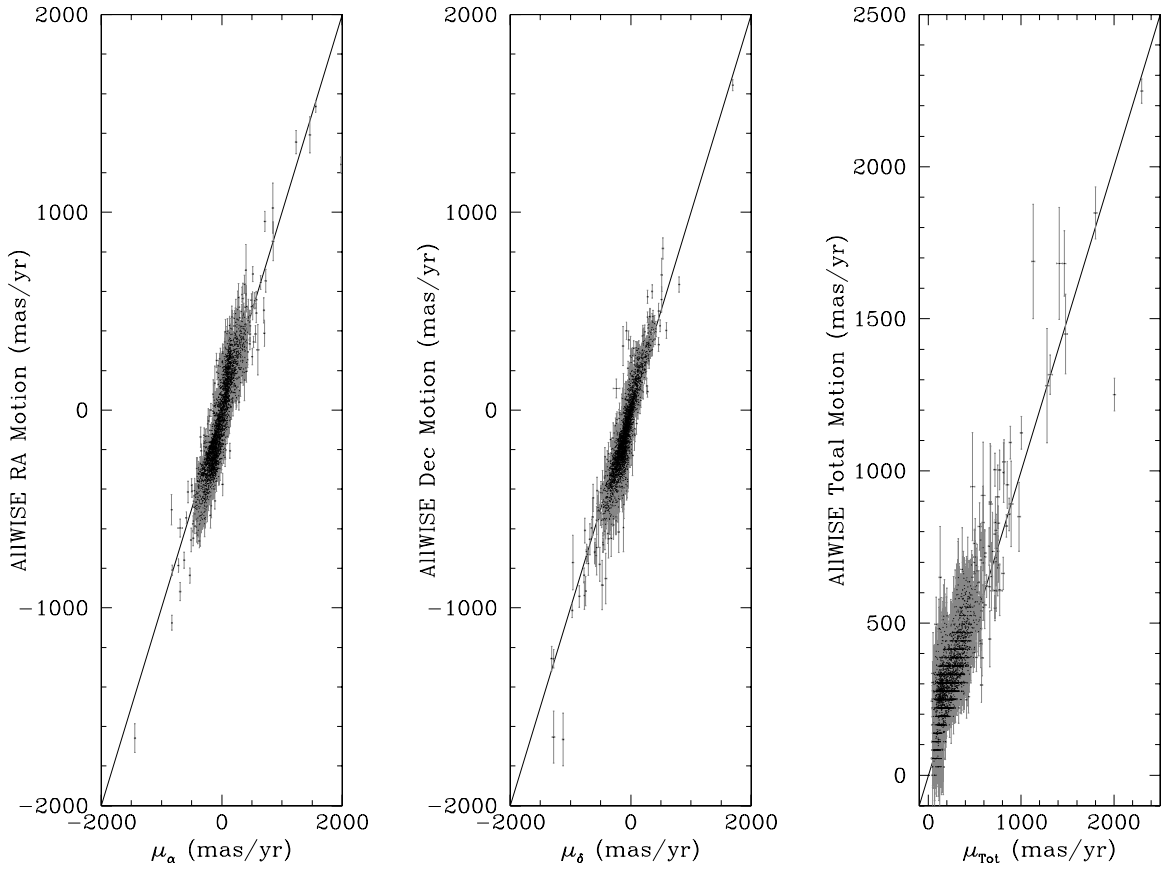

Figure 16. AllWISE-measured R.A. (left), Decl. (middle), and total (right) motions plotted against proper motions measured using the 2MASS-to-WISE time baseline for objects in Table 3. The line of one-to-one correspondence is shown in each panel.

logic, however—they have high motions not because they are close but because they are old. As a result, these objects have reduced motion values that are significantly fainter than objects of average kinematics (see Reid 1997 for a more extensive discussion). Fortunately, this enables such objects (which tend to be low-metallicity because they are very old) to be easily selected from the bulk of objects (of near solar metallicity) in the Galactic disk. Several objects with reduced proper motion at J band > 19 mag and $0.8 < J-W2 < 1.5$ mag can be seen in Figure 20 and are prime low-metallicity candidates.

Figure 21 shows the $J - K_s$ color plotted against the $J-W2$ color. The locus at lower left near (0.3, 0.3) corresponds roughly to late-F or early-G spectral types (Ali 2014) and marks the earliest spectral types for which we have new motions. The bulk of objects clustered near (1.1, 0.8) are mid-M dwarfs, which by far dominate the solar neighborhood (Figure 11 of Kirkpatrick et al. 2012). The trail of objects into the upper right corner of the figure is the ∼30 L and T dwarfs. This diagram also shows a collection of objects that fall below the standard main sequence. Qualitatively, if we take the long-baseline color, $J - W2$, to be indicative of temperature or spectral type, and the short-baseline color, $J - K_s$ to sample more specific atmospheric physics, we would expect objects at the same $J-W2$ value as a standard main sequence star but with a bluer $J - Ks$ value to be low-metallicity because of the increased contribution of collision-induced absorption by H_2 at K band. Hence, this diagram provides another handy way—using colors instead of motions, as in Figure 20—to select low-metallicity candidates.

5. COMPARISON TO THE LUHMAN (2014) MOTION LIST

While this paper was being finalized, Luhman (2014) published an independently selected set of motion objects uncovered in the same *WISE* data set. Rather than using AllWISE results, his methodology started with the publicly available single exposure catalogs from each phase of the mission. The ecliptic polar regions were ignored (to save on processing time) and the rest of the *WISE* data divided into discrete epochs encompassing the twelve or more revisits of the same patch of sky with an overall time difference generally less than one day. The mean coordinates of the group at a single epoch were computed, and these were compared to other groups at other epochs as long as two groups were within 1.″5 of one another. Motions were thus computed for these groups paired across epochs, and groups for which no pairings were found were examined separately in case they corresponded to very high motion objects. The Luhman (2014) list contains 762 objects, and its sky distribution (lower panel of Figure 15) is similar to ours, although the source density is considerably lower. Of those 762 objects, 321 are also included in our Table 3, one (the unconfirmed object WISEA J085510.74−071442.5) is included in Table 4, and another (WISEA J104915.52−531906.1) was eliminated from consideration because it was published earlier by Luhman (2013).

The remaining 439 objects enable us to determine which of our selection criteria were set too tightly, so that future researchers can perform their own, refined searches. Some sources fail more than one of the criteria discussed in Section 4.1.

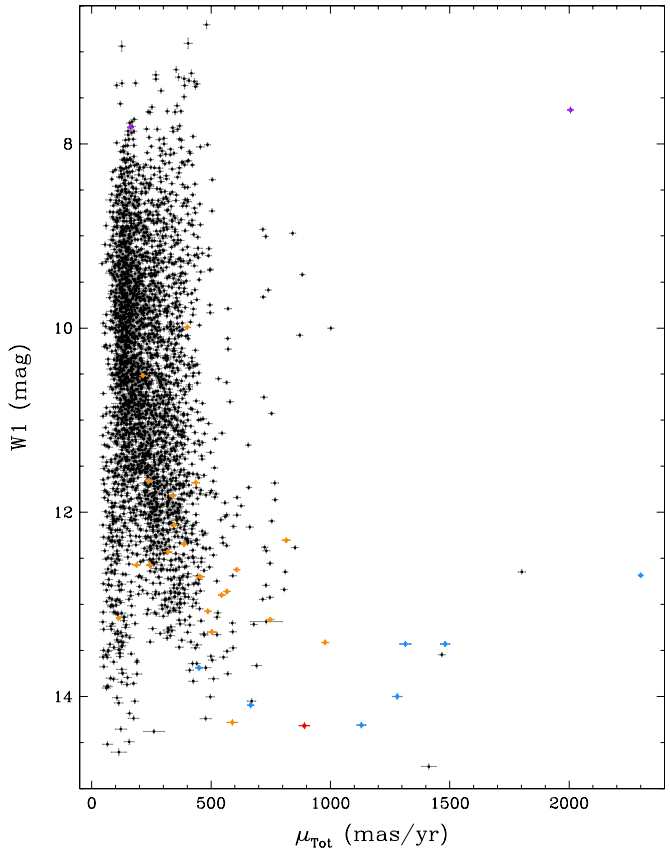

Figure 17. AllWISE $W1$ profile-fit photometry plotted as a function of the total 2MASS-to-WISE proper motion for objects in Table 3. Objects with spectroscopic follow-up in Table 5 are color coded as follows: Light blue—early-L subdwarfs; red—late-L subdwarfs; purple—bright M dwarfs discussed in Section 8; dark orange—all others.

(A color version of this figure is available in the online journal.)

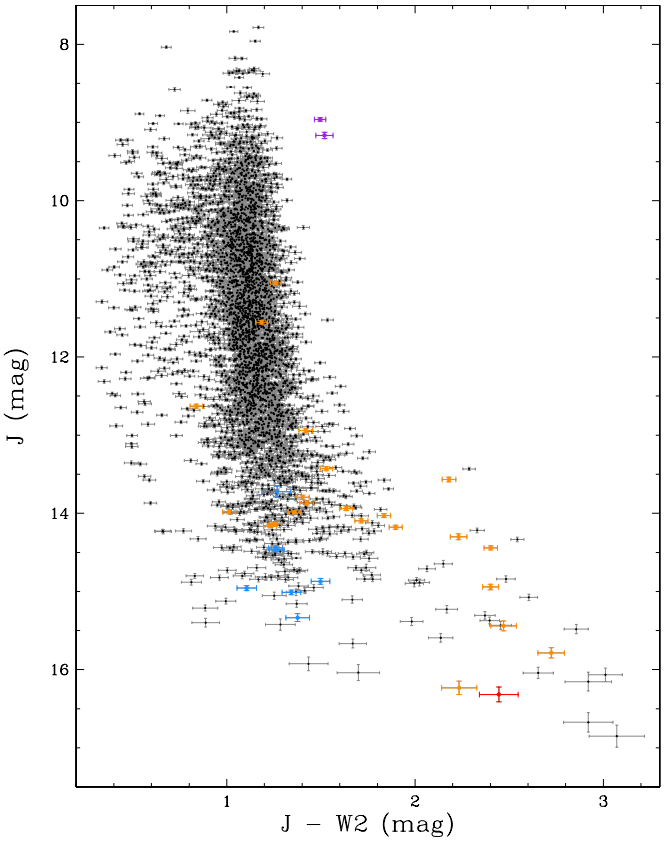

Figure 18. 2MASS J-band magnitude plotted against the $J-W2$ color for the motion objects in Table 3. Color coding is the same as in Figure 17.

(A color version of this figure is available in the online journal.)

Specifically, a total of 80% (351/439) of the objects were missed because the $rchi2/rchi2\_pm$ ratio failed to exceed a threshold of 1.03. That is, the reduced χ^2 from the motion fit was not markedly better than that from the stationary fit. In most cases, the reduced χ^2 was improved, but this improvement was less than 3%.

The next most problematic criteria were the restrictions that $w?rchi2$ be less than 2.0 to ensure a point-like source. These failed in 39% (172/439) of the cases. In a similar vein, 13% (56/439) of the sources failed the $nb = 1$ criterion to assure that the source was not blended. In most of these cases, a check of the *WISE* images confirms that the motion source from Luhman (2014) is blended with another source and/or appears slightly elongated, but AllWISE processing was nonetheless able to handle these cases. (It should be expected, however, that there are plenty of other cases of blending and elongation that are not so elegantly handled.) Finally, 15% (64/439) of the sources failed the Q criterion, 2.5% (11/439) failed the cc_flags criterion, 1.4% (6/439) failed the *pmcode* criterion, 1.4% (6/439) were missed during by-eye Quality Assurance reviewing (one of these was caused by a poor stretch on the images used to scrutinize candidates), 0.7% (3/439) were lost due to transcription errors, and 0.2% (1/439) is a previously published source that was removed from our list because it was not a new discovery.

Figure 22 compares the Luhman (2014) motion objects (760 total after removing WISEA J085510.74−071442.5 and WISEA J104915.52−531906.1) to our list of 3525 objects with confirmed motions (Table 3). The plot shows histograms in $W1$ magnitude and in total proper motion computed from the 2MASS-to-WISE time baseline. Our survey tends to sample brighter objects than the Luhman (2014) catalog and, as a result, also probes to considerably smaller motion. Both surveys are able to select high motion objects, although there are somewhat fewer objects with $\mu > 750$ mas yr^{-1} in the Luhman (2014) list than in ours.

Our criteria missed objects found by Luhman (2014), but Luhman (2014) also missed objects found by us. Our second-highest motion object, WISEA J154045.67−510139.3, is one notable example of the latter case. Clearly, the AllWISE data products hold many other potential discoveries. Moreover, with the *WISE* satellite having been reactivated in 2013 December for an additional three years of data taking, extending this all-sky motion survey to even smaller motion limits via the extended time baseline will also be possible. Such a survey would allow researchers to expand the volume and spectral type range over which *WISE* motion discoveries can be made.

6. SPECTROSCOPIC FOLLOW-UP OF SELECTED DISCOVERIES

We have selected objects for spectroscopic observation as follows. Figure 17 was used primarily to select objects of highest motion, since these tend to be either close or low-metallicity. Figure 18 was used to look for objects that were bright in J-band magnitude relative to their peers in $J-W2$ color, since such objects are generally the closest objects of their type. Figure 19 was used to select late-type objects, although all of the T dwarf

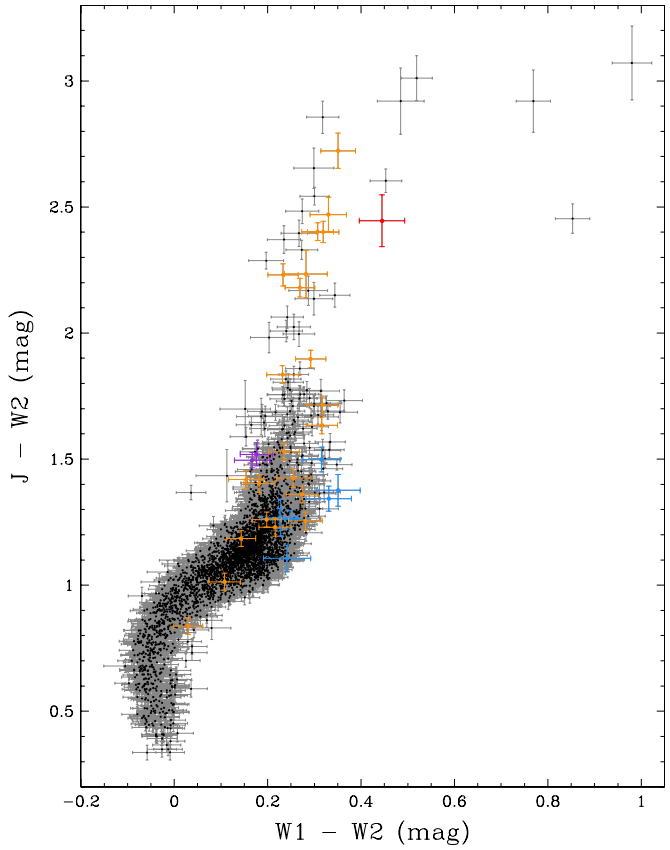

Figure 19. $J-W2$ color vs. $W1-W2$ color for the motion objects in Table 3. Color coding is the same as in Figure 17.

(A color version of this figure is available in the online journal.)

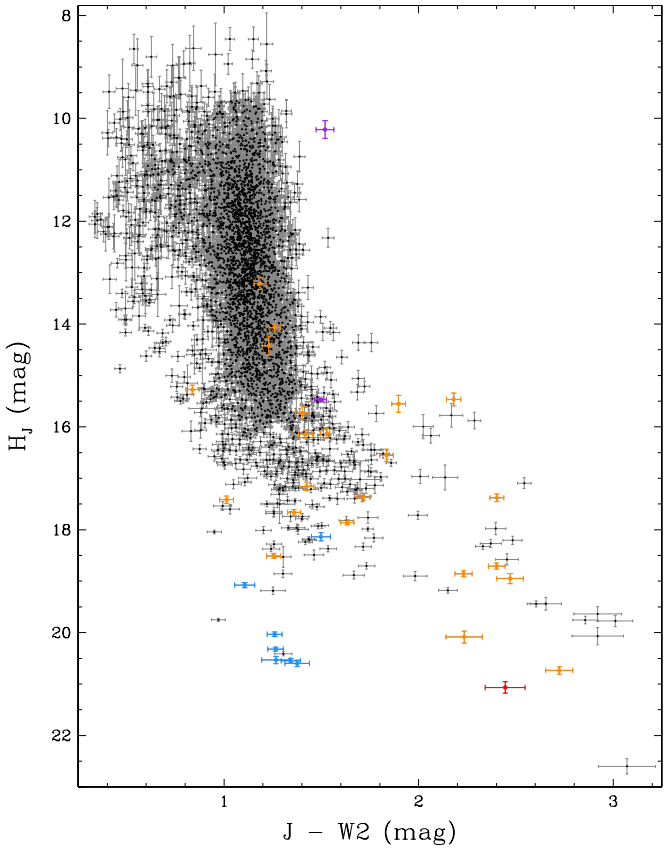

Figure 20. Reduced proper motion at J band plotted against the $J-W2$ color for the motion objects in Table 3. Color coding is the same as in Figure 17.

(A color version of this figure is available in the online journal.)

candidates were at unfavorable sky positions for the follow-up obtained for this paper. Figures 20 and 21 were used to select low-metallicity objects since, as explained earlier, such objects tend to fall in the lower parts of these diagrams, thereby distinguishing themselves from the bulk of objects, which have solar metallicities. Objects for which we have obtained spectroscopic follow-up are color coded in Figures 17–21, as described in the legend to Figure 17. These follow-up observations are detailed below and summarized in Table 5.

6.1. Optical Spectroscopy

One source was observed (by S.F.A.) on the night of 2013 July 07 UT with the Double Spectrograph on the Hale 5m telescope on Palomar Mountain, California. In the red-side spectrograph, a 316 lines mm^{-1} grating blazed at 7500 Å was used to produce a spectrum covering the range 3800–10500 Å. Standard reduction procedures for CCD data were employed. This night had cirrus clouds.

Six sources were observed (by D.S., M.B., and G.B.L.) on the nights of 2013 October 4–5 UT with the Low Resolution Imaging Spectrometer (LRIS; Oke et al. 1995) at the 10 m W. M. Keck Observatory on Mauna Kea, Hawai'i. The blue side was used with a 600 lines mm^{-1} grating blazed at 4000 Å, and the red side was used with a 400 lines mm^{-1} grating blazed at 8500 Å. Objects had very little flux in the blue side so the blue-side spectra are not considered further. The red side produced a spectrum covering the range from 5500 to 10000 Å. Standard reduction procedures for CCD data were employed. The first night had clouds and the second night was clear.

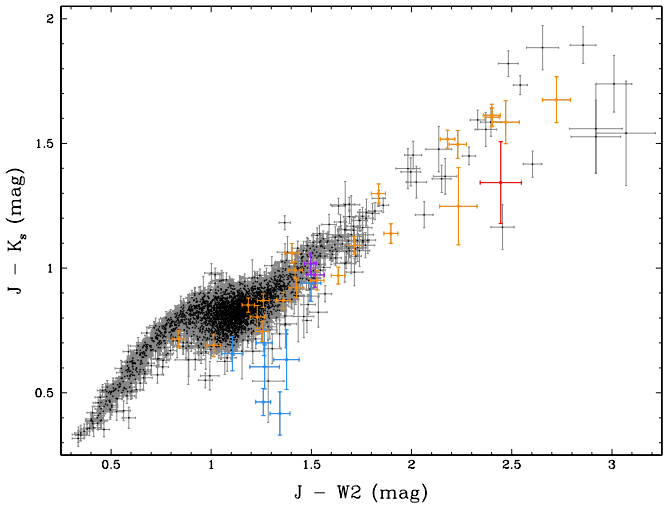

Figure 21. $J-K_s$ color plotted against the $J-W2$ color for the motion objects in Table 3. Color coding is the same as in Figure 17.

(A color version of this figure is available in the online journal.)

Three sources were observed (by D.S.) on the clear night of 2013 December 11 UT with the Deep Imaging Multi-object Spectrograph (DEIMOS; Faber et al. 2003) at the 10 m W. M. Keck Observatory on Mauna Kea, Hawai'i. The instrument was used in single-object mode utilizing the 1200 line mm^{-1} grating blazed at 7500 Å to provide continuous wavelength coverage from 6650 to 9300 Å. Standard reduction procedures for CCD data were employed.

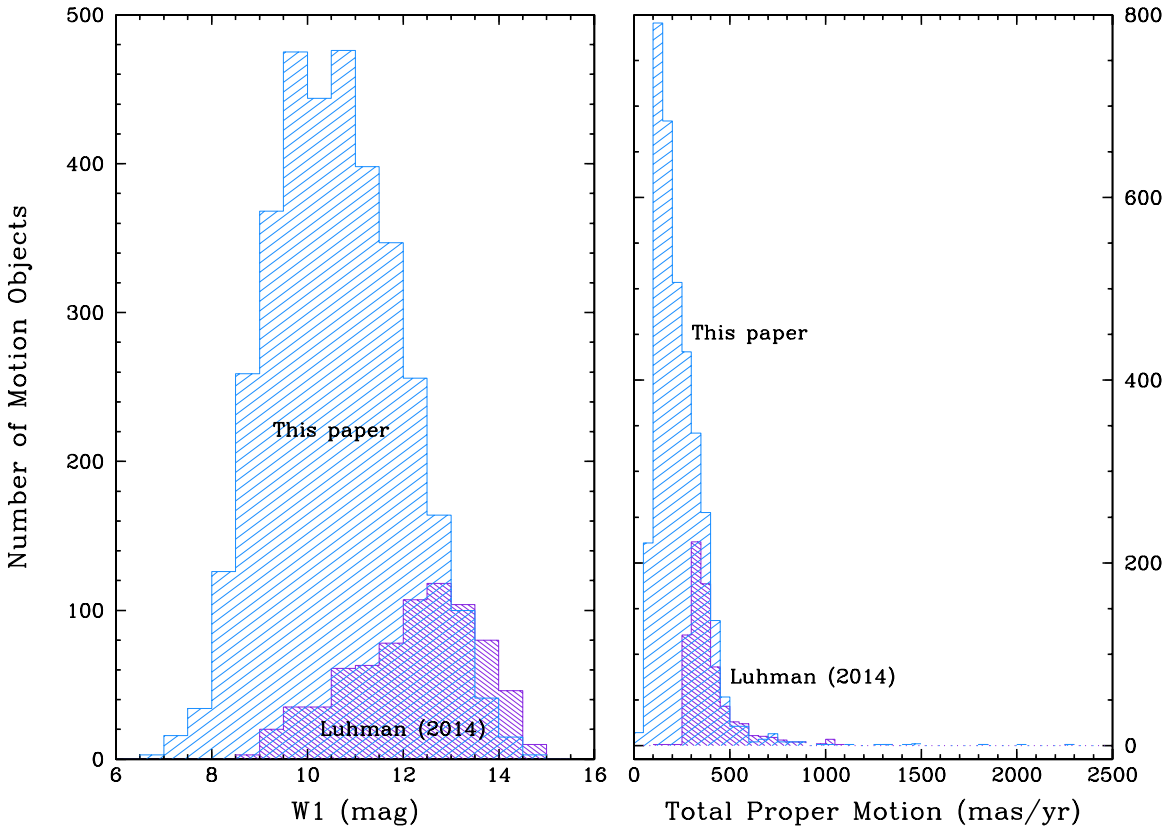

Figure 22. Histograms of the $W1$ mag (left panel) and total 2MASS-to-WISE proper motion (right panel) for our survey (light blue; 3525 objects from Table 3) compared to that of Luhman (2014; violet; 760 objects total).

(A color version of this figure is available in the online journal.)

Two objects were observed (by J.A.R.) on the clear nights of 2014 January 27 and 28 UT with the Inamori-Magellan Areal Camera and Spectrograph (IMACS; Dressler et al. 2011) on the 6.5m Walter Baade Telescope at Las Campanas Observatory, Chile. The f/4 camera was used with a Bessel *V*-band or a CTIO *I*-band filter for imaging observations and with a 600 lines mm^{-1} grating for the spectroscopic observations. The grating angle was set for a wavelength coverage of 7100–10400 Å. Standard reduction procedures for CCD data were again employed.

6.2. Near-infrared Spectroscopy

Several sources were observed with SpeX (Rayner et al. 2003) on the NASA 3m Infrared Telescope Facility (IRTF) on Mauna Kea, Hawai'i. The UT dates of observation were 2013 August 14 (by A.J.B.; cirrus and patchy clouds), 2013 October 24 (by A.S.; clear skies), 2013 November 21–22 and 24 (by J.K.F. and N.S.; thick cirrus on the first night but then clear), and 2013 December 14–15 (by A.S.; clear). For all but the October night, SpeX was used in prism mode with a 0.″5 or 0.″8 wide slit to achieve a resolving power of $R \equiv \lambda/\Delta\lambda \approx$ 100–150 over the range 0.8–2.5 μm. For the October run, SpeX was used in cross-dispersed mode to produce spectra over the range 0.9–2.4 μm with a resolving power of $R \equiv \lambda/\Delta\lambda \approx 1200$. All data were reduced using Spextool (Cushing et al. 2004); A0 stars were used for the telluric correction and flux calibration steps following the technique described in Vacca et al. (2003).

Several sources were also observed on the UT nights of 2013 November 20 and 2013 December 14 (by G.N.M. and S.E.L.) with the Near-Infrared Spectrometer (NIRSPEC; McLean et al. 1998, 2000) at the 10 m W. M. Keck Observatory on Mauna Kea, Hawai'i. There was cirrus on the November night and heavier clouds on the December one. In low-resolution mode, use of the 42″ × 0.″38 slit results in a resolving power of $R \equiv \lambda/\Delta\lambda \approx 2500$. Our brown dwarf candidates were observed in the N3 configuration (see McLean et al. 2003) that covers part of the *J*-band window from 1.15 to 1.35 μm. Data were reduced using the REDSPEC package, as described in McLean et al. (2003).

6.3. Spectral Classification

We have typed the optical spectra as follows. Each spectrum was normalized at 7500 Å or 8250 Å and overplotted on a suite of like-normalized LRIS spectra of primary M and L optical spectral standards from Kirkpatrick et al. (1991) and Kirkpatrick et al. (1999). These plots were examined by eye to determine the best match and to look for any peculiarities with respect to the standard sequence. Objects falling midway between integral classes (such as M9 and L0) were assigned the half class in between (in this case, M9.5). Objects showing notable peculiarities were given a suffix of "pec" unless the peculiarities were determined to be caused by low-metallicity, in which case these were reclassified against published optical spectra typed as late-M and early-L subdwarfs and given a prefix of "sd."

We have typed the near-infrared spectra as follows. Each target spectrum was normalized to one at 1.28 μm and compared to the near-infrared spectral standards from Kirkpatrick et al. (2010) normalized the same way. Using the methodology outlined in that paper, the core near-infrared type was determined *only* from the 0.9–1.4 μm portion, and then the corresponding goodness of fit to the same spectral standard from 1.4–2.5 μm was judged. In most cases the same spectral standard also

Table 5
Spectroscopic Follow-up of Motion Candidates

Object Name	Opt Sp. Type	NIR Sp. Type	Telescope/ Instrument	Obs. Date (UT)	Exp. Time[a] (s)	Corrector Star
(1)	(2)	(3)	(4)	(5)	(6)	(7)
WISEA J001450.17−083823.4	sdL0	...	Keck/DEIMOS	2013 Dec 11	600	...
WISEA J004326.26+222124.0	...	sdL1	IRTF/SpeX	2013 Oct 24	960	HD 7215
WISEA J004713.81−371033.7	L4:	...	Keck/DEIMOS	2013 Dec 11	600	...
WISEA J005757.64+201304.0	sdL7	...	Keck/LRIS	2013 Oct 5	1167/1130	...
...	...	sdL7	IRTF/SpeX	2013 Nov 24	1800	HD 16811
WISEA J020201.25−313645.2	sdL0	...	Keck/LRIS	2013 Oct 5	600/600	...
WISEA J023421.83+601227.3	M9.5e	...	Palomar/DSpec	2013 Jul 7	2900	...
WISEA J030601.66−033059.0	sdL0	...	Keck/DEIMOS	2013 Dec 11	300	...
...	...	sdL0	IRTF/SpeX	2013 Nov 22	720	HD 13936
WISEA J040418.01+412735.5	...	L3 pec (red)	IRTF/SpeX	2013 Oct 24	720	HD 21038
WISEA J043535.82+211508.9	sdL0	...	Keck/LRIS	2013 Oct 4	300/300	...
...	...	sdL0	IRTF/SpeX	2013 Oct 24	960	HD 27761
...	...	sdL0	Keck/NIRSPEC	2013 Dec 14	2400	HD 35036
WISEA J045921.21+154059.2	...	sdL0	IRTF/SpeX	2013 Nov 22	360	HD 35036
WISEA J053257.29+041842.5	...	L3	Keck/NIRSPEC	2013 Nov 20	720	HD 39953
WISEA J054318.95+642250.2	...	L2	Keck/NIRSPEC	2013 Dec 14	1440	HD 33654
WISEA J055007.94+161051.9	...	L2	IRTF/SpeX	2013 Nov 24	720	HD 43583
WISEA J060742.13+455037.0	...	L2.5	Keck/NIRSPEC	2013 Dec 14	1800	HD 45105
...	...	L2.5	IRTF/SpeX	2013 Dec 15	960	HD 45105
WISEA J063957.71−034607.2	sdM0.5	...	Keck/LRIS	2013 Oct 4	300/300	...
WISEA J065958.55+171710.9	...	L2	Keck/NIRSPEC	2013 Nov 20	960	HD 39953
WISEA J071552.38−114532.9	...	L5 pec?	Keck/NIRSPEC	2013 Nov 20	960	HD 43607
...	...	L4 pec (blue)	IRTF/SpeX	2013 Dec 14	960	HD 56525
WISEA J072003.20−084651.3	...	M9	IRTF/SpeX	2013 Dec 14	960	HD 56525
WISEA J074211.69−121151.6	...	<M0 (wd?)	IRTF/SpeX	2013 Nov 21	1800	HD 67725
WISEA J082640.45−164031.8	...	L9	Keck/NIRSPEC	2013 Dec 14	2400	HD 72282
WISEA J085224.36+513925.5	...	M7	IRTF/SpeX	2013 Dec 15	960	HD 45105
WISEA J091657.18−112104.7	...	M9	IRTF/SpeX	2013 Dec 15	960	HD 45105
WISEA J102304.04+155616.4	...	M8 pec	IRTF/SpeX	2013 Dec 14	960	HD 89239
WISEA J154045.67−510139.3	M6	...	Magellan/IMACS	2014 Jan 27	100	...
WISEA J162702.28−694411.8	M4+M4	...	Magellan/IMACS	2014 Jan 28	300	...
WISEA J163605.71−044013.8	...	M4.5	IRTF/SpeX	2013 Aug 14	120	HD 159008
WISEA J182121.91−070008.6	M7 pec	...	Keck/LRIS	2013 Oct 4	400/350	...
WISEA J204027.30+695924.1	sdL0	...	Keck/LRIS	2013 Oct 5	300/300	...
WISEA J204218.13−082137.8	...	M7	IRTF/SpeX	2013 Oct 24	960	HD 193689
WISEA J211543.59−322540.4	...	M6:	IRTF/SpeX	2013 Aug 14	960	HD 199090
WISEA J222013.75−361709.5	...	M8 pec	IRTF/SpeX	2013 Oct 24	960	HD 194272
WISEA J224128.33+043459.3	...	M7.5	IRTF/SpeX	2013 Oct 24	960	HD 210501
WISEA J232036.88+315739.5	...	M4.5	IRTF/SpeX	2013 Oct 24	960	HD 210290
WISEA J235459.79−185222.4	...	L2	Keck/NIRSPEC	2013 Dec 14	1800	HD 219833

Note. [a] For Keck/LRIS, the two exposure times refer to the blue-side spectrograph (left) and the red-side spectrograph (right).

provided the best fit in this longer-wavelength region. In other cases, the target spectrum was notably much bluer or redder so the fit across the *H* and *K* windows was very poor despite the excellent fit in the *J* window. These peculiar objects were given suffixes of "pec (blue)" or "pec (red)" to denote the slope of the spectrum relative to the standard (see Figure 23). Some of the peculiar spectra were deemed to be low-metallicity (prefix of "sd") and were typed against near-infrared spectra of similar subdwarfs from the published literature.

Optical and/or near-infrared spectral types are listed in Table 5. Subdwarfs are discussed in Section 7, and two bright M dwarf systems are discussed in Section 8.

7. A TROVE OF L SUBDWARF DISCOVERIES

A number of discoveries have the photometric characteristics of subdwarfs (i.e., low-metallicity objects) and were confirmed as such by our follow-up spectroscopy. Two of these are early-M subdwarfs—the sdM0.5 WISEA J063957.71−034607.2 and the usdM3 discovery by Wright et al. (2013) WISEA J070720.50+170532.7. Six others fall near late-M/early-L and another, WISEA J005757.64+201304.0, falls at late-L.

One of the subdwarfs near the M/L transition is our highest motion discovery, WISEA J204027.30+695924.1. As Figure 24 shows, the optical spectrum of this object is intermediate in type between an sdM8 and an sdL1. One of the most distinctive features in the optical spectra of subdwarfs at the M/L boundary is the emission-like feature near 7050 Å that is, in fact, a narrow wavelength region relatively free of opacity between the strong CaH band to the blue and the strong TiO band to the red. Optical spectra of four other AllWISE discoveries (Figure 25) show this same telltale signature and have overall spectral morphologies very similar to WISEA J204027.30+695924.1.

Note that this spectral morphology is distinctly different from that of a normal late-M dwarf (top spectrum in Figure 26), due mainly to the relatively stronger hydride bands in the subdwarfs. Only a few subdwarfs are known in this spectral range, so their

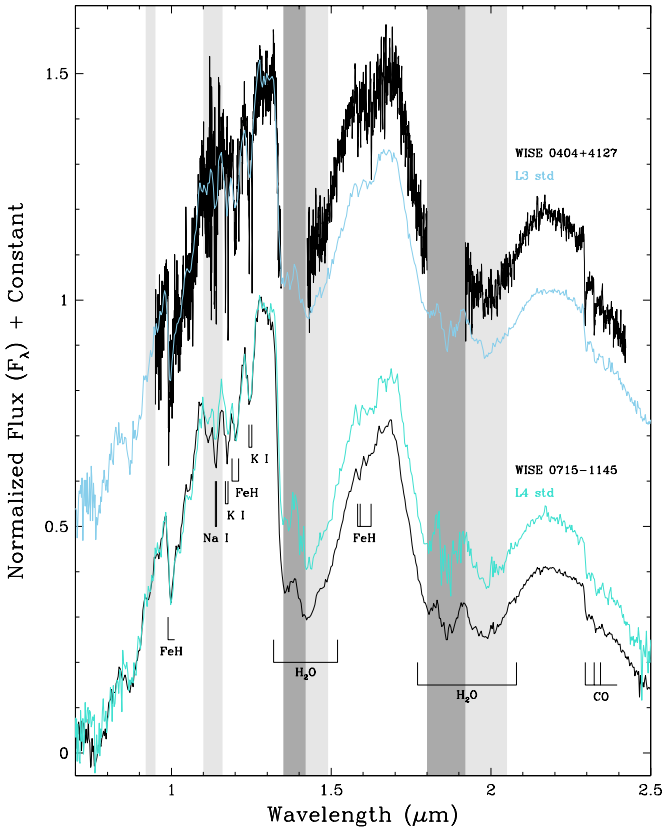

Figure 23. Near-infrared spectra of WISEA J040418.01+412735.5 (discovered earlier by Castro et al. 2013 and hence removed from our discovery list in Table 3) and WISEA J071552.38−114532.9 overplotted with the near-infrared spectral standard (Kirkpatrick et al. 2010) providing the best match throughout *J* band. Note that the *H*- and *K*-band spectra of WISEA J040418.01+412735.5 are much redder than the standard, and that of WISEA J071552.38−114532.9 is much bluer than the standard. Prominent spectral features are marked. Per Rayner et al. (2009), regions of telluric absorption are marked by the dark gray (atmospheric transmission < 20%) and light gray (20% < atmospheric transmission < 80%) zones in wavelength. Spectra have been normalized at 1.28 μm and a constant offset added to the flux to separate the spectra vertically except where overplotting was intended.

(A color version of this figure is available in the online journal.)

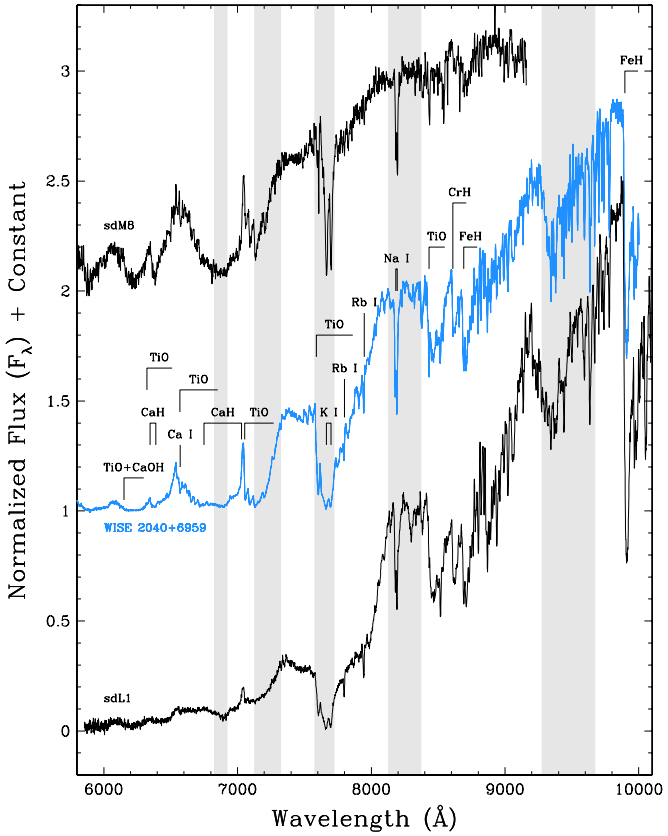

Figure 24. Optical spectra of the sdM8 LSPM J1425+7102 (Lépine et al. 2007) and the sdL1 2MASS 17561080+2815238 (Kirkpatrick et al. 2010) compared to the optical spectrum of WISEA J204027.30+695924.1. Prominent spectral features are marked. Spectra have been normalized at 8250 Å and a constant offset added to the flux to separate the spectra vertically. Regions of telluric absorption are marked by the light gray bands.

(A color version of this figure is available in the online journal.)

classification is still in its infancy. In fact, no spectroscopic standards yet exist at these types, but we can compare to other published discoveries and use their tentative types as guides. A sampling of these very late-M and early-L subdwarfs from the literature is shown by the bottom four spectra in Figure 26. There is a plateau in these spectra between 7300 and 7500 Å that is bounded on the blue side by TiO absorption and on the red side by TiO and a strong K I doublet. The slope at the top of this plateau slowly changes from slightly red to flat through the sdM9-to-sdL0.5 sequence. That is, the flux (in units of f_λ) at the left edge of the plateau near 7300 Å is lower or equal to the flux at the right edge of the plateau near 7500 Å. A check of the sdM8 spectrum in Figure 24 shows that the plateau has a redward slope, whereas the sdL1 spectrum in the same figure has a plateau with a blueward slope. Because all of our spectra in Figure 25 have plateaus with flat or slightly blueward slopes, we choose to classify all of these as sdL spectra. None, however have a spectral morphology as extreme as the sdL1 in Figure 24 and look more similar to the sdM9-to-sdL0.5 sequence in Figure 26. Thus, we tentatively classify all five of these spectra as sdL0.

Near-infrared spectra of four of the AllWISE motion discoveries are shown in Figure 27 and are compared with near-infrared spectra of an sdM9.5 and the optically classified sdL1 from Figure 24. These spectra have a similar spectral morphology—notably, strong FeH at 9896 Å and suppressed fluxes at *H* and *K* bands relative to *J*. This morphology is similar to that of the sdM9.5 and the sdL1. Two of the AllWISE objects, WISEA J030601.66−033059.0 and WISEA J043535.82+211508.9, also have optical spectra, shown in Figure 25, that we classify as sdL0. Thus, we tentatively classify these of these AllWISE sources as sdL0 objects in the near-infrared, whereas we classify WISEA J004326.26+222124.0—because its spectral morphology is more like 2MASS J17561080+2815238—as an sdL1.

One final L subdwarf discovery from AllWISE, WISEA J005757.64+201304.0, falls at late-L. Figure 28 compares the optical and near-infrared spectra of this object with the L7 standard and with a known sdL7 from the literature. In the optical, WISEA J005757.64+201304.0 fits the overall spectral shape of the normal L7 well except in the strength of the TiO band at 8432 Å, the CrH band at 8611 Å, and the FeH band at 8692 Å, all of which are stronger in the AllWISE object than in the standard. The published sdL7 spectrum, while fitting the overall shape as well as the normal L7 standard, also nicely matches the strengths of the these three discrepant bands. In the near-infrared, the spectrum of the AllWISE object best matches the L7 standard in the *J* band—although the match is rather poor—but the standard is much redder in the *H* and *K* portions of the spectrum. The near-infrared spectrum of the sdL7, on the other hand, provides a better match at *J* band, an excellent match

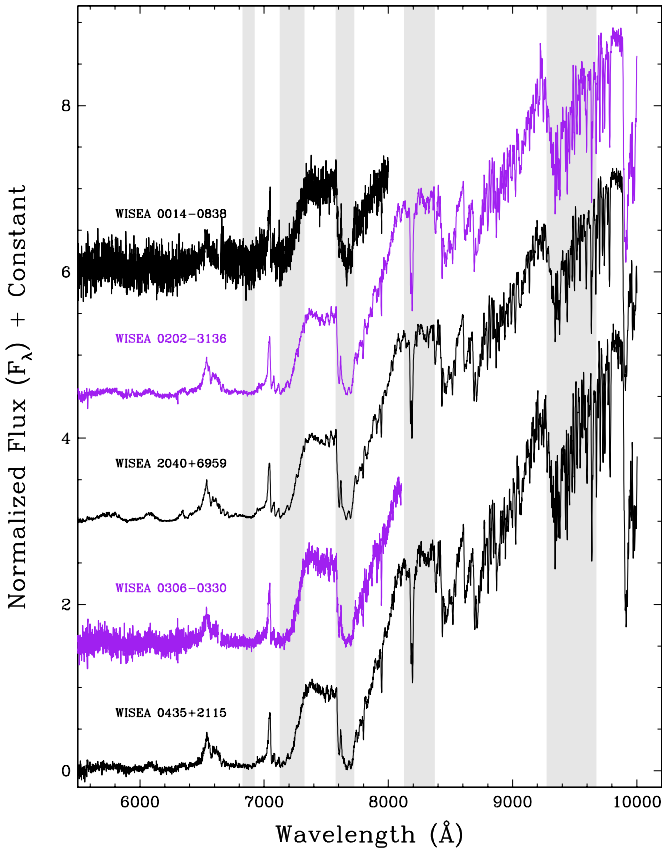

Figure 25. Optical spectra of five early-L subdwarf discoveries from AllWISE: WISEA J001450.17−083823.4, WISEA J020201.25−313645.2, WISEA J204027.30+695924.1, WISEA J030601.66−033059.0, and WISEA J043535.82+211508.9. Spectra have been normalized at 7500 Å and a constant offset added to the flux to separate the spectra vertically. Regions of telluric absorption are marked by the light gray bands.

(A color version of this figure is available in the online journal.)

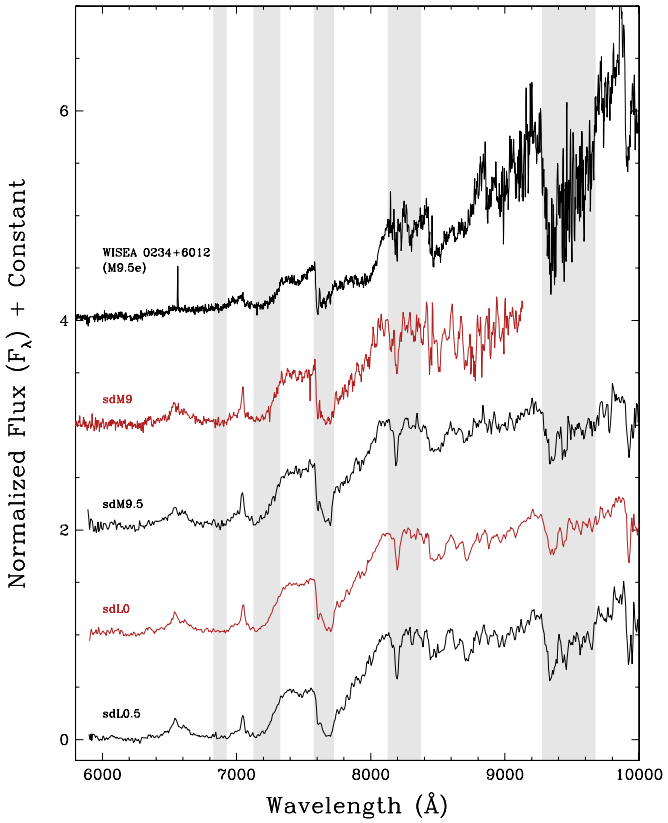

Figure 26. Optical spectrum of a normal M9.5e dwarf (the motion star WISEA J023421.83+601227.3) compared to optical spectra of very late-M and early-L subdwarfs from the literature: the sdM9 2MASS J16403197+1231068 from Gizis & Harvin (2006), the sdM9.5 ULAS J115826.62+044746.8 from Lodieu et al. (2010), and the sdL0 ULAS J033350.84+001406.1 and the sdL0.5 ULAS J124425.90+102441.9 from Lodieu et al. (2012). Spectra have been normalized at 7500 Å and a constant offset added to the flux to separate the spectra vertically. Regions of telluric absorption are marked by the light gray bands.

(A color version of this figure is available in the online journal.)

at *H*, and a much improved match at *K*. For these reasons, we tentatively classify this object as an sdL7 in both the optical and the near-infrared.

Our follow-up from AllWISE has already added several new L subdwarfs to the number published to date. Table 6 compiles all of the late-M and L subdwarfs currently recognized. Of these, 20 were known prior to AllWISE follow-up and eight are from this paper. Additional follow-up of other AllWISE motion sources is certain to reveal others. It is curious that the AllWISE subdwarf discoveries tend to cluster around a type of sdL0. Is this providing a hint regarding the number density of these objects in the solar neighborhood? Table 6 lists the AllWISE motions for all of the known late-M and L subdwarfs detected by *WISE*. Although a few of the detected objects do not have significant AllWISE motions, most could be easily selected (and many of these were noted as having been found during Quality Assurance reviews). While AllWISE is capable of uncovering subdwarfs throughout the L subdwarf range, objects at mid-L types seem to be lacking. Of the 28 objects in this table, only five fall in the broad range from sdL2 to sdL6. Seventeen objects alone are known within sdM9-sdL1 and another five are known within the sdL7-sdL8 range. (The "schizophrenic" object LSR J1610−0040 is not included in this list since its spectrum defies classification.)

Figure 29 is a rehash of Figure 21 with all known spectroscopically identified late-M and L-type subdwarfs color coded. This diagram hints at the possibility that a lightly populated gap may exist between the early-L subdwarf and late-L subdwarf populations. Such a gap would be expected on theoretical grounds: Lower metallicities generally correspond to older ages. At these older ages, substellar objects have had enough time to cool that a gap in temperature will have opened up between the hottest members of their population and the coldest, lowest mass members of similarly aged hydrogen-burning stars. Such a temperature gap would be wider the older the population, and hence, the lower the metallicity. Figure 29 shows the first signs of what may be a sparsely populated locus of color space corresponding to this temperature gap.

The late-L subdwarf at (1.92,0.26) on Figure 29 is the (e?)sdL7 2MASS J05325346+8246465 (Burgasser et al. 2003). That object has a trigonometric parallax measurement; after comparison to theoretical evolutionary models, Burgasser et al. (2008) find that the resulting luminosity is consistent with the object being a very high-mass brown dwarf just below the hydrogen-burning limit. This would place the object on the brown dwarf side of the L subdwarf gap, as shown in the figure. The early-L subdwarf at (1.30,−0.03) is the sdL4 2MASS J16262034+3925190; Burgasser (2004) finds that this object is near or below the hydrogen-burning minimum mass limit, consistent with our placement of it on the opposite side of the sparsely populated "subdwarf gap."

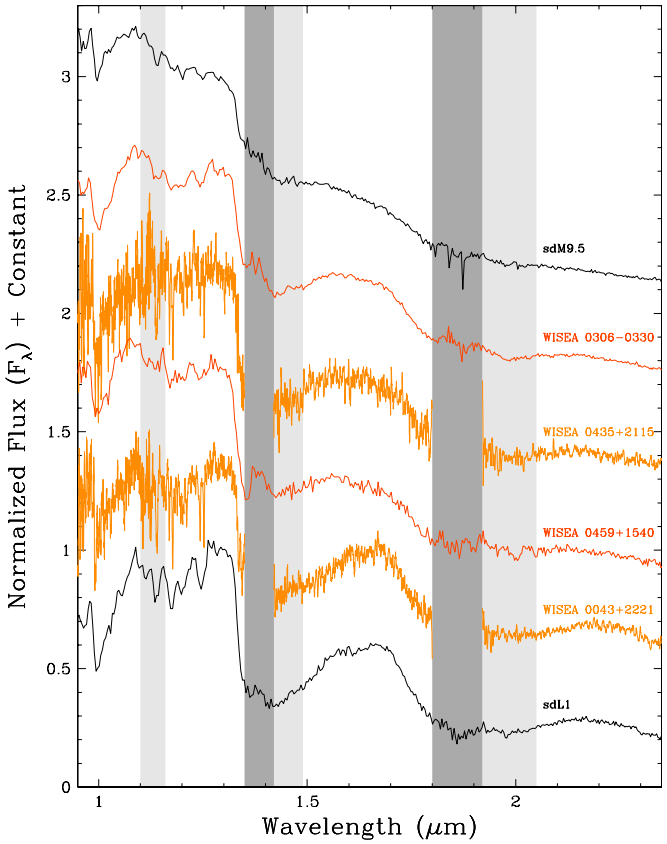

Figure 27. Near-infrared spectra of the sdM9.5 J1013−1356 (Burgasser et al. 2007) and the sdL1 2MASS J17561080+2815238 (Kirkpatrick et al. 2010) compared to the near-infrared spectra of four discoveries from AllWISE: WISEA J030601.66−033059.0, WISEA J043535.82+211508.9, WISEA J045921.21+154059.2 and WISEA J004326.26+222124.0. Regions of telluric absorption are marked by the dark gray and light gray bands as explained in the caption to Figure 23. Spectra have been normalized at 1.28 μm and a constant offset added to the flux to separate the spectra vertically.

(A color version of this figure is available in the online journal.)

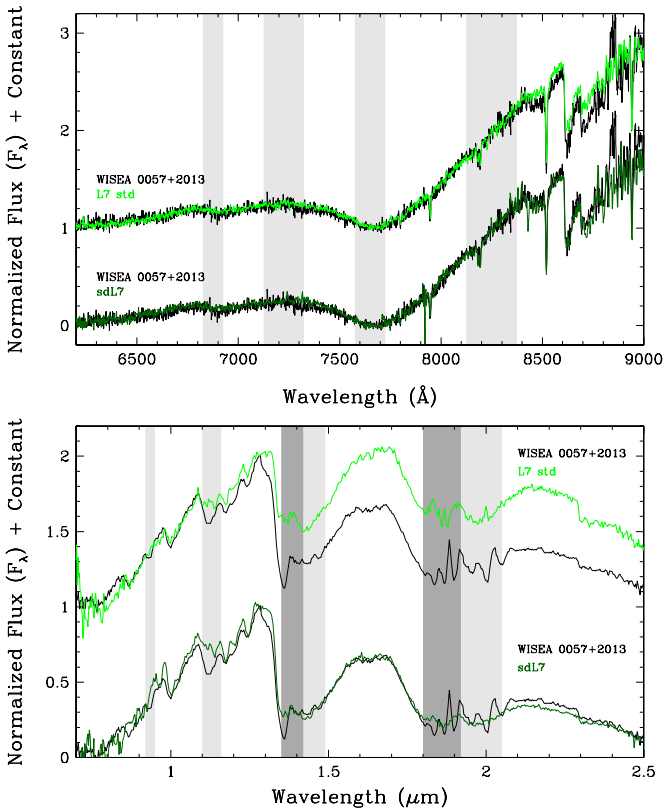

Figure 28. Spectra of WISEA J005757.64+201304.0 compared to the L7 standard and an sdL7 from the literature. (Upper panel) The optical spectrum of the AllWISE object compared to the optical L7 standard DENIS-P J0205.4−1159 (Kirkpatrick et al. 1999) and the sdL7 2MASS J11582077+0435014 (Kirkpatrick et al. 2010). (Lower panel) The near-infrared spectrum of the AllWISE object compared to the near-infrared L7 standard 2MASS J01033203+1935361 and the sdL7 2MASS J11582077+0435014 (both from Kirkpatrick et al. 2010). Normalizations, offsets, and telluric-zone shading are the same as in previous figures.

(A color version of this figure is available in the online journal.)

Despite these checks against limited published results, the zone of L subdwarf avoidance shown on Figure 29 should be regarded only as a cartoon depiction of expectations. With continued follow-up of motion discoveries from AllWISE, it is hoped that researchers will be able to more fully explore the boundaries of the gap, if it is real.

8. TWO NEW, NEARBY M DWARF SYSTEMS

There is a single object, WISEA J154045.67−510139.3, occupying the upper right quadrant of Figure 17. This object is very bright, $J = 8.96 \pm 0.02$ mag and $W2 = 7.47 \pm 0.02$ mag, and has a very large motion, $\mu = 2006 \pm 12$ mas yr^{-1}, which is the second-highest motion of any of our discoveries. A finder chart is shown in the upper panel of Figure 30. Our optical spectrum (Figure 31) shows this object to be a normal M6 dwarf. The absolute J-band magnitude for a typical M6 dwarf is 10.12 mag (Equation (6) of Cruz et al. 2003), which would place this object at a distance of ∼5.9 pc if single or ∼8.3 pc if an equal-magnitude double. We have gathered positional information on this source from a variety of online archives, as listed in Table 7. Using our fitting code, which is explained in Section 5.2 of Kirkpatrick et al. (2011), we obtain the following astrometric solution with $\chi^2 = 9.5$ and five degrees of freedom: $\mu_\alpha = 1\farcs951 \pm 0\farcs006$ yr^{-1}, $\mu_\delta = -0\farcs332 \pm 0\farcs006$ yr^{-1}, and $\pi = 0\farcs165 \pm 0\farcs041$ ($d \approx 6$ pc). Although the value of the parallax is very fragile given the size of its uncertainty, the available astrometry strongly suggests that this object is close to the Sun, in agreement with our spectrophotometric distance estimate.

A second, bright object is seen next to WISEA J154045.67−510139.3 on Figure 18. This object, WISEA J162702.28−694411.8, has magnitudes and colors of $J = 9.16 \pm 0.04$ mag, $W2 = 7.65 \pm 0.02$ mag, $J - W2 = 1.52 \pm 0.05$ mag, and $J - K_s = 0.97 \pm 0.05$ mag. A finder chart is shown in the lower panel of Figure 30. Our follow-up imaging shows it to be a near equal-magnitude binary separated by 2″.0. magnitude differences between the two components are found to be $\Delta V = 0.18 \pm 0.01$ mag and $\Delta I = 0.13 \pm 0.01$ mag. Optical spectra of the two components (Figure 31) show that both are normal M4 dwarfs. The absolute J-band magnitude for a typical M4 dwarf is 7.89 mag (Equation (6) of Cruz et al. 2003), which would place this near-equal-magnitude binary at a distance of ∼25 pc. Using additional positional information listed in Table 7, we obtain the following astrometric solution with $\chi^2 = 1.22$ and five degrees of freedom: $\mu_\alpha = 0\farcs096 \pm 0\farcs007$ yr^{-1}, $\mu_\delta = 0\farcs133 \pm 0\farcs006$ yr^{-1}, and $\pi = 0\farcs008 \pm 0\farcs039$. At face value, a nearby distance seems not to be supported by these data, but we note that the first four (of five) data points were all taken in March or April—i.e.,

Table 6
A List of Known Late-M (⩾M9) and L Subdwarfs

Designation	Opt. Sp. Type	NIR Sp. Type	Ref.	2MASS J (mag)	2MASS H (mag)	2MASS K_s (mag)	$W1$ (mag)	$W2$ (mag)	AllWISE R.A. Motion (mas yr^{-1})	AllWISE Decl. Motion (mas yr^{-1})
(1)	(2)	(3)	(4)	(5)	(6)	(7)	(8)	(9)	(10)	(11)
WISEA J001450.17−083823.4	sdL0	...	1	14.469 ± 0.026	13.950 ± 0.026	13.769 ± 0.044	13.429 ± 0.025	13.204 ± 0.030	1392 ± 92	−406 ± 93
2MASS J00412179+3547133	...	sdL?	19	15.935 ± 0.081	15.728 ± 0.152	15.166 ± 0.121	14.743 ± 0.032	14.454 ± 0.049	13 ± 133	54 ± 136
...	...	sdM9	20	...	...	...	...	...	...	...
WISEA J004326.26+222124.0	...	sdL1	1	14.871 ± 0.038	14.226 ± 0.039	13.931 ± 0.063	13.688 ± 0.025	13.373 ± 0.031	270 ± 59	−381 ± 60
WISEA J005757.65+201304.0	sdL7	sdL7	1	16.317 ± 0.095	15.449 ± 0.088	14.974 ± 0.134	14.317 ± 0.029	13.872 ± 0.039	853 ± 98	−260 ± 101
WISEA J020201.25−313645.2	sdL0	...	1	15.335 ± 0.050	14.937 ± 0.098	14.702 ± 0.108	14.310 ± 0.028	13.959 ± 0.038	−278 ± 132	−1666 ± 134
WISEA J030601.66−033059.0	sdL0	sdL0	1	14.441 ± 0.026	14.060 ± 0.040	13.978 ± 0.048	13.429 ± 0.025	13.181 ± 0.027	388 ± 44	−1258 ± 47
ULAS J033350.84+001406.1	sdL0	...	2	16.018 ± 0.111	15.698 ± 0.178	>16.630	15.077 ± 0.038	14.765 ± 0.071	663 ± 284	−70 ± 300
WISEA J043535.82+211508.9	sdL0	sdL0	1	15.011 ± 0.031	14.682 ± 0.053	14.594 ± 0.081	13.999 ± 0.029	13.668 ± 0.039	1022 ± 127	−771 ± 138
WISEA J045921.22+154059.2	...	sdL0	1	14.957 ± 0.031	14.613 ± 0.047	14.300 ± 0.062	14.093 ± 0.028	13.851 ± 0.042	707 ± 130	−553 ± 142
2MASS J05325346+8246465	late sdL	late sdL	17	15.179 ± 0.058	14.904 ± 0.091	14.918 ± 0.145	13.824 ± 0.025	13.260 ± 0.028	2416 ± 77	−1450 ± 83
...	(e?)sdL7	(e?)sdL7	4	...	...	...	...	...	...	...
...	(e)sdL7:α	(e)sdL7:α	18	...	...	...	...	...	...	...
...	sdL7	...	12	...	...	...	...	...	...	...
...	esdL7	esdL7	24	...	...	...	...	...	...	...
2MASS J06164006−6407194	sdL5	sdL5	9	16.403 ± 0.112	16.275 ± 0.228	>16.381	15.646 ± 0.030	15.183 ± 0.042	1438 ± 162	−63 ± 177
2MASS J06453153−6646120	sdL8	sdL8	4	15.602 ± 0.067	14.696 ± 0.070	14.372 ± 0.084	13.761 ± 0.023	13.308 ± 0.023	−851 ± 45	1134 ± 44
SSSPM J1013−1356	sdM9.5	sdM9.5	12	14.621 ± 0.029	14.382 ± 0.048	14.398 ± 0.077	13.797 ± 0.026	13.604 ± 0.032	90 ± 93	−1087 ± 100
...	sdM9.5	...	21	...	...	...	...	...	...	...
2MASS J11582077+0435014	sdL7	sdL7	4	15.611 ± 0.054	14.684 ± 0.064	14.439 ± 0.063	13.695 ± 0.026	13.361 ± 0.033	871 ± 103	−633 ± 109
ULAS J115826.62+044746.8	sdM9.5	...	2	16.536 ± 0.130	16.079 ± 0.201	15.725 ± 0.186	15.655 ± 0.051	15.408 ± 0.121	127 ± 469	−913 ± 525
ULAS J124425.90+102441.9	sdL0.5	...	2	16.198 ± 0.128	15.650 ± 0.160	>15.400	15.453 ± 0.041	15.138 ± 0.088	−84 ± 310	−174 ± 337
...	sdL2?	...	25	...	...	...	...	...	...	...
SDSS J125637.13−022452.4	sdL4?	...	8	16.099 ± 0.105	15.792 ± 0.148	>15.439	15.210 ± 0.036	15.005 ± 0.080	−604 ± 183	−50 ± 195
...	sdL3.5	sdL3.5	10	...	...	...	...	...	...	...
...	...	esdL3.5	24	...	...	...	...	...	...	...
HD 114762B[a]	—	d/sdM9	11	...	...	...	...	...	...	...
SDSS J133348.24+273508.8	sdL3	...	25	...	...	...	...	...	...	...
ULAS J135058.86+081506.8	sdL5 ± 1	esdL4	3	...	...	...	...	...	...	...
SDSS J141624.08+134826.7	sdL7	sdL7	4	13.148 ± 0.021	12.456 ± 0.027	12.114 ± 0.021	11.363 ± 0.022	11.026 ± 0.020	5 ± 27	80 ± 28
...	d/sdL7	...	5	...	...	...	...	...	...	...
...	L5	L4 ± 1.5 (blue)	6	...	...	...	...	...	...	...
...	L6 ± 0.5	L6± pec	7	...	...	...	...	...	...	...
...	d/sdL7	d/sdL7	24	...	...	...	...	...	...	...

Table 6
(Continued)

Designation	Opt. Sp. Type	NIR Sp. Type	Ref.	2MASS J (mag)	2MASS H (mag)	2MASS K_s (mag)	$W1$ (mag)	$W2$ (mag)	AllWISE R.A. Motion (mas yr^{-1})	AllWISE Decl. Motion (mas yr^{-1})
(1)	(2)	(3)	(4)	(5)	(6)	(7)	(8)	(9)	(10)	(11)
2MASS J14343616+2202463	...	sdM9	20	14.519 ± 0.034	13.833 ± 0.040	13.545 ± 0.041	13.248 ± 0.024	12.877 ± 0.026	−752 ± 40	177 ± 42
SSSPM J1444−2019	d/sdM9	...	12	12.546 ± 0.023	12.142 ± 0.024	11.933 ± 0.024	11.471 ± 0.023	11.211 ± 0.022	−3329 ± 45	−1864 ± 47
...	sdM9 or sdL	...	14	...	...	...	...	...	...	...
LSR J1610−0040	sdL	...	16	12.911 ± 0.018	12.302 ± 0.020	12.019 ± 0.026	11.637 ± 0.243	11.537 ± 0.023	−906 ± 51	−1220 ± 51
...	sd?M6 pec	...	22	...	...	...	...	...	...	...
...	...	d/sdM v. pec?	23	...	...	...	...	...	...	...
2MASS J16262034+3925190	...	sdL	15	14.435 ± 0.026	14.533 ± 0.049	14.466 ± 0.074	13.482 ± 0.024	13.136 ± 0.026	−1539 ± 68	398 ± 71
...	sdL4	...	13	...	...	...	...	...	...	...
...	sdL4	...	12	...	...	...	...	...	...	...
...	...	esdL4	24	...	...	...	...	...	...	...
2MASS J16403197+1231068	d/sdM9	...	12	15.946 ± 0.077	15.605 ± 0.112	>15.520	15.033 ± 0.036	14.846 ± 0.068	−365 ± 250	−324 ± 267
	sdM9/sdL?	...	13	...	...	...	...	...	...	...
	...	sdM8?	19	...	...	...	...	...	...	...
2MASS J17561080+2815238	sdL1	L1 pec (blue)	4	14.712 ± 0.031	14.135 ± 0.040	13.813 ± 0.040	13.384 ± 0.024	13.068 ± 0.026	−748 ± 67	−541 ± 73
WISEA J204027.30+695924.1	sdL0	...	1	13.723 ± 0.070	13.313 ± 0.066	13.119 ± 0.054	12.684 ± 0.023	12.456 ± 0.022	1535 ± 29	1643 ± 28

Notes. [a] Also known as 2MASS J13121982+1731016B.

References. (1) This paper, (2) Lodieu et al. 2012; (3) Lodieu et al. 2010; (4) Kirkpatrick et al. 2010; (5) Burningham et al. 2010; (6) Schmidt et al. 2010a; (7) Bowler et al. 2010; (8) Sivarani et al. 2009; (9) Cushing et al. 2009; (10) Burgasser et al. 2009; (11) Bowler et al. 2009; (12) Burgasser et al. 2007; (13) Gizis & Harvin 2006; (14) Scholz et al. 2004b; (15) Burgasser 2004; (16) Lépine et al. 2003 and Dahn et al. 2008; (17) Burgasser et al. 2003; (18) Kirkpatrick 2005; (19) Burgasser et al. 2004; (20) Sheppard & Cushing 2009; (21) Scholz et al. 2004a; (22) Reiners & Basri 2006; (23) Cushing & Vacca 2006; (24) Zhang et al. 2013; (25) Zhang et al. 2012.

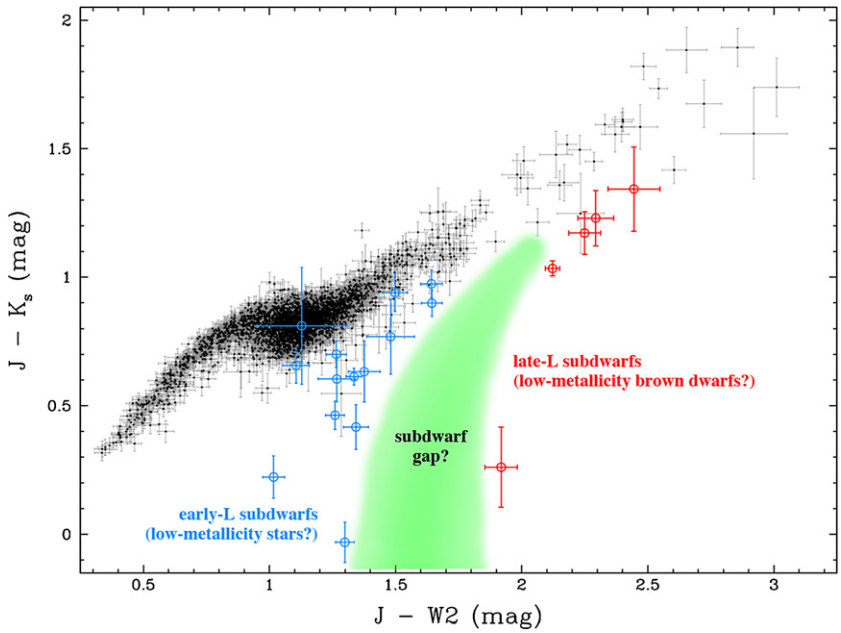

Figure 29. AllWISE motion stars (solid black dots) from Figure 21, with the three possible T dwarfs omitted for clarity. The locations of known late-M and L subdwarfs from Table 6 are shown by open circles. Those with spectral types earlier than sdL5 are shown in blue and those with types later than sdL5 are shown in red. The wedge (green zone) depicts an area of color space where L subdwarfs may rarely be found. See the text for details.

(A color version of this figure is available in the online journal.)

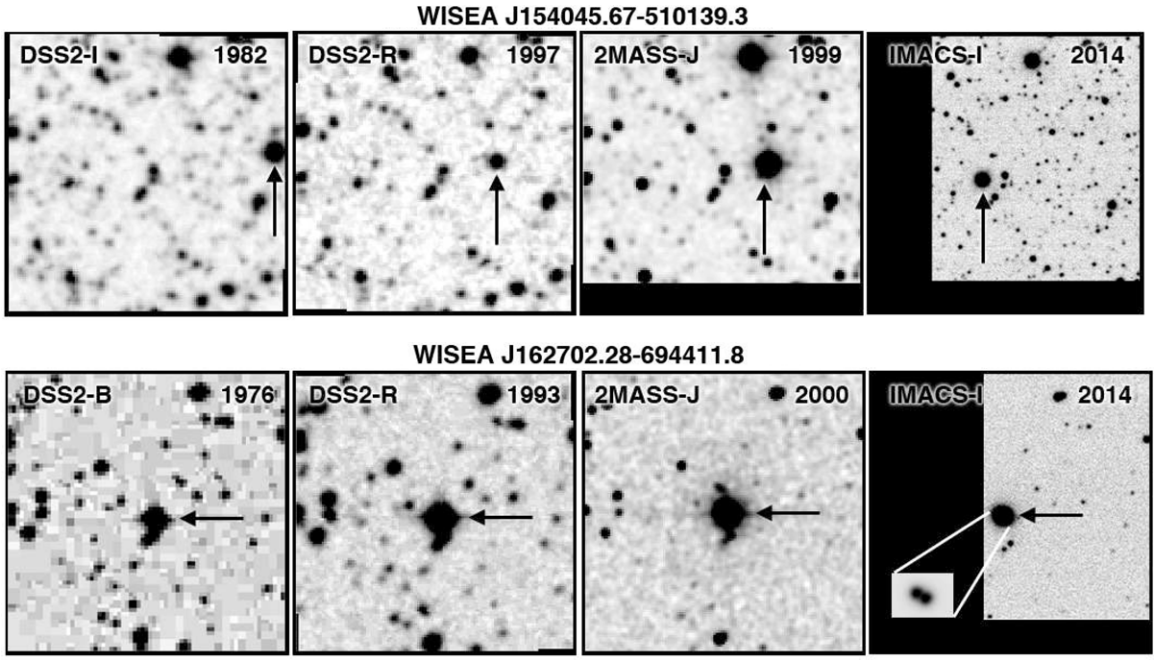

Figure 30. Images from DSS2, 2MASS, and Magellan/IMACS for two nearby M dwarf systems. (Upper panel) DSS2-*I*, DSS2-*R*, 2MASS-*J*, and IMACS-*I* images for the motion object WISEA J154045.67−510139.3. (Lower panel) DSS2-*B*, DSS2-*R*, 2MASS-*J*, and IMACS-*I* images for the motion object WISEA J162702.28−694411.8. In both panels, the epoch of each image is labeled and the position of the motion star in indicated by an arrow. Each subpanel is 2′ square with north up and east to the left. The inset on the IMACS-*I* image for WISEA J162702.28−694411.8AB shows the individual components of the system.

at nearly the same parallax factor. Only the final observation, taken in September, provides any leverage regarding the size of the parallax. Moreover, the binarity of the source may be complicating clean measurements of the photocenter. Additional astrometric monitoring is needed.

WISEA J154045.67−510139.3 and WISEA J162702.28−694411.8 have Galactic coordinates of (328.°0,+3.°4) and (319.°7,−14.°2), respectively, and fall in the lower right quadrant of Figure 15 (middle panel). One of the objects in the Luhman (2014) list, WISE J163348.95−680851.6 ($J = 11.19$ mag, $J - K_s = 1.12$ mag, J - $W2 = 2.20$ mag), is located at Galactic coordinates of (321.°0,−13.°4), and may be another close object, likely a late-M or early-L dwarf. The density of *WISE* motion discoveries in this quadrant demonstrates that a large area around the Galactic Center has been poorly surveyed by earlier searches for nearby stars.

Table 7
Additional Astrometric Data for The Two Nearby M-Dwarf Systems

MJD	Calendar Date	J2000 R.A. (deg)	J2000 Decl. (deg)	R.A. Error (″)	Decl. Error (″)	Notes
(1)	(2)	(3)	(4)	(5)	(6)	(7)
WISEA J154045.67−510139.3						
45078.690	1982 Apr 19	235.166113	−51.025275	0.333	0.333	DSS2 *I*-band
50554.606	1997 Apr 16	235.179017	−51.026369	0.333	0.333	DSS2 *R*-band
51364.022	1999 Jul 05	235.180914	−51.026588	0.06	0.06	2MASS
55251.096	2010 Feb 24	235.190210	−51.027578	0.071	0.067	*WISE* All-Sky
55432.482	2010 Aug 24	235.190481	−51.027619	0.044	0.041	*WISE* three-band Cryo
WISEA J162702.28−694411.8						
42869.726	1976 Apr 01	246.75713	−69.73792	0.5	0.5	DSS2 *B*-band
48352.721	1991 Apr 06	246.75809	−69.737244	0.33	0.33	DSS2 *I*-band
51652.288	2000 Apr 18	246.758802	−69.736984	0.06	0.06	2MASS
55264.727	2010 Mar 09	246.759567	−69.736625	0.066	0.064	*WISE* All-Sky
55444.838	2010 Sep 05	246.759596	−69.736595	0.041	0.039	*WISE* three-band Cryo

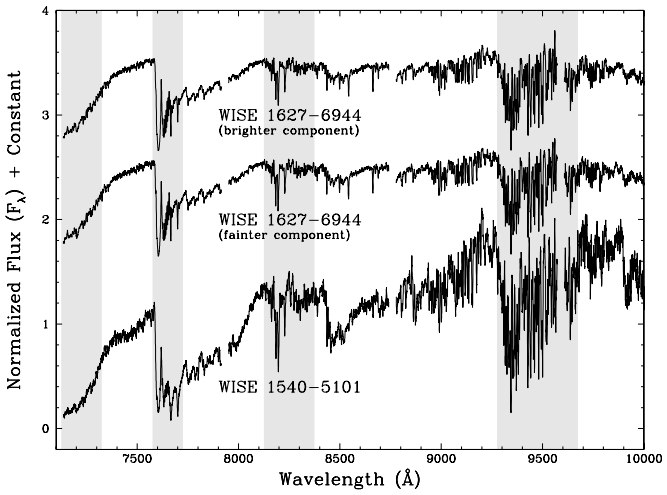

Figure 31. Optical spectra of the two components of the WISEA J162702.28−694411.8AB system (top spectra) and WISEA J154045.67−510139.3 (bottom spectrum). Spectra have been normalized at 7500 Å and a constant offset added to the flux to separate the spectra vertically. Regions of telluric absorption are marked by the light gray bands.

9. CONCLUSIONS

We have characterized the motion measurements contained within the AllWISE Data Release. We have presented a list of 3525 motion objects lacking previous literature in SIMBAD and find two very interesting results. The first is that AllWISE is revealing many more examples of low-metallicity objects near the stellar/substellar break, allowing researchers to probe the region near the hydrogen-burning minimum mass for objects formed early in the history of the Milky Way. The second is that AllWISE is continuing the *WISE* legacy of uncovering previously overlooked, very nearby objects. Prior to AllWISE processing, *WISE* had already revealed several nearby systems never before recognized –e.g., the L+T binary WISE J104915.57−531906.1 at 2.0 pc (Luhman 2013) and the T6 dwarf WISEPC J150649.97+702736.0 (Kirkpatrick et al. 2011) possibly as close as 3.4 pc (Marsh et al. 2013); AllWISE has already contributed another overlooked object—WISEA J154045.67−510139.3 (∼5.9 pc)—to this distinguished list of *WISE* discoveries within the canonical 8 pc sample. The motion measurements provided by AllWISE will likely provide researchers many new gifts over the years to come.

This publication makes use of data products from *WISE*, which is a joint project of the University of California, Los Angeles, and the Jet Propulsion Laboratory (JPL)/California Institute of Technology (Caltech), funded by the National Aeronautics and Space Administration (NASA). This research has made use of the NASA/IPAC Infrared Science Archive, which is operated by JPL/Caltech, under contract with NASA. We are indebted to the SIMBAD database and the VizieR catalog access tool, provided by CDS, Strasbourg, France, and we acknowledge use of the Database of Ultracool Parallaxes maintained by Trent Dupuy. We thank our referee, whose critique of the original draft resulted in a clearer, more complete paper. We thank Fiona Harrison, George Djorgovski, Brian Mazur, and Barry Madore for PI-ing telescope time used for spectroscopic follow-up and are grateful for the time allotted by Caltech, NASA/IRTF, and the Carnegie Observatories. We also thank Nicolas Lodieu, John Gizis, and Sebastien Lépine for providing published spectra of subdwarfs.

Facilities: WISE, Hale(Double Spectrograph), Keck:I(LRIS), Keck:II(DEIMOS, NIRSPEC), IRTF(SpeX), Magellan:Baade (IMACS).

REFERENCES

Ali, B. 2014, AAS Meeting 223, 441.37
Bidelman, W. P. 1985, ApJS, 59, 197
Bowler, B. P., Liu, M. C., & Cushing, M. C. 2009, ApJ, 706, 1114
Bowler, B. P., Liu, M. C., & Dupuy, T. J. 2010, ApJ, 710, 45
Burgasser, A. J. 2004, ApJL, 614, L73
Burgasser, A. J., Cruz, K. L., & Kirkpatrick, J. D. 2007, ApJ, 657, 494
Burgasser, A. J., Kirkpatrick, J. D., Burrows, A., et al. 2003, ApJ, 592, 1186
Burgasser, A. J., McElwain, M. W., Kirkpatrick, J. D., et al. 2004, AJ, 127, 2856
Burgasser, A. J., Vrba, F. J., Lépine, S., et al. 2008, ApJ, 672, 1159
Burgasser, A. J., Witte, S., Helling, C., et al. 2009, ApJ, 697, 148
Burningham, B., Leggett, S. K., Lucas, P. W., et al. 2010, MNRAS, 404, 1952
Castro, P. J., Gizis, J. E., Harris, H. C., et al. 2013, ApJ, 776, 126
Cruz, K. L., Reid, I. N., Kirkpatrick, J. D., et al. 2007, AJ, 133, 439
Cruz, K. L., Reid, I. N., Liebert, J., Kirkpatrick, J. D., & Lowrance, P. J. 2003, AJ, 126, 2421
Cushing, M. C., Looper, D., Burgasser, A. J., et al. 2009, ApJ, 696, 986
Cushing, M. C., & Vacca, W. D. 2006, AJ, 131, 1797
Cushing, M. C., Vacca, W. D., & Rayner, J. T. 2004, PASP, 116, 362
Dahn, C. C., Harris, H. C., Levine, S. E., et al. 2008, ApJ, 686, 548
Day-Jones, A. C., Pinfield, D. J., Napiwotzki, R., et al. 2008, MNRAS, 388, 838
Dressler, A., Bigelow, B., Hare, T., et al. 2011, PASP, 123, 288
Dupuy, T. J., & Liu, M. C. 2012, ApJS, 201, 19
Faber, S. M., Phillips, A. C., Kibrick, R. I., et al. 2003, Proc. SPIE, 4841, 1657

Finch, C. T., Zacharias, N., & Henry, T. J. 2010, AJ, 140, 844
Gianninas, A., Bergeron, P., & Ruiz, M. T. 2011, ApJ, 743, 138
Gizis, J. E. 2002, ApJ, 575, 484
Gizis, J. E., & Harvin, J. 2006, AJ, 132, 2372
Harrington, R. S., & Dahn, C. C. 1980, AJ, 85, 454
Harrington, R. S., Dahn, C. C., Kallarakal, V. V., et al. 1993, AJ, 105, 1571
Henry, T. J., Jao, W.-C., Subasavage, J. P., et al. 2006, AJ, 132, 2360
Henry, T. J., Kirkpatrick, J. D., & Simons, D. A. 1994, AJ, 108, 1437
Høg, E., Fabricius, C., Makarov, V. V., et al. 2000, A&A, 355, L27
Keenan, P. C., & Keller, G. 1953, ApJ, 117, 241
Keenan, P. C., & Pitts, R. E. 1980, ApJS, 42, 541
Kerber, F., Mignani, R. P., Smart, R. L., & Wicenec, A. 2008, A&A, 479, 155
Kirkpatrick, J. D. 2005, ARA&A, 43, 195
Kirkpatrick, J. D., Beichman, C. A., & Skrutskie, M. F. 1997, ApJ, 476, 311
Kirkpatrick, J. D., Cushing, M. C., Gelino, C. R., et al. 2011, ApJS, 197, 19
Kirkpatrick, J. D., Gelino, C. R., Cushing, M. C., et al. 2012, ApJ, 753, 156
Kirkpatrick, J. D., Henry, T. J., & McCarthy, D. W., Jr. 1991, ApJS, 77, 417
Kirkpatrick, J. D., Looper, D. L., Burgasser, A. J., et al. 2010, ApJS, 190, 100
Kirkpatrick, J. D., McGraw, J. T., Hess, T. R., et al. 1994, ApJS, 94, 749
Kirkpatrick, J. D., Reid, I. N., Liebert, J., et al. 1999, ApJ, 519, 802
Kirkpatrick, J. D., Reid, I. N., Liebert, J., et al. 2000, AJ, 120, 447
Lawson, W. A., Crause, L. A., Mamajek, E. E., & Feigelson, E. D. 2002, MNRAS, 329, L29
Lépine, S., Rich, R. M., & Shara, M. M. 2003, ApJL, 591, L49
Lépine, S., Rich, R. M., & Shara, M. M. 2007, ApJ, 669, 1235
Lépine, S., & Shara, M. M. 2005, AJ, 129, 1483
Lodieu, N., Espinoza Contreras, M., Zapatero Osorio, M. R., et al. 2012, A&A, 542, A105
Lodieu, N., Zapatero Osorio, M. R., Martín, E. L., Solano, E., & Aberasturi, M. 2010, ApJL, 708, L107
Luhman, K. L. 2001, ApJ, 560, 287
Luhman, K. L. 2013, ApJL, 767, L1
Luhman, K. L. 2014, ApJ, 781, 4
Luyten, W. J. 1979a, The Luyten Half Second Catalog (2nd ed.; Minneapolis, MN: Univ. of Minnesota)
Luyten, W. J. 1979b, The New Luyten Two Tenths Catalog (Minneapolis, MN: Univ. of Minnesota)
Maheswar, G., Manoj, P., & Bhatt, H. C. 2003, A&A, 402, 963
Mainzer, A., Bauer, J., Grav, T., et al. 2011, ApJ, 731, 53
Marsh, K. A., Wright, E. L., Kirkpatrick, J. D., et al. 2013, ApJ, 762, 119
Martín, E. L., Phan-Bao, N., Bessell, M., et al. 2010, A&A, 517, A5
McCaughrean, M. J., Close, L. M., Scholz, R.-D., et al. 2004, A&A, 413, 1029
McLean, I. S., Becklin, E. E., Bendiksen, O., et al. 1998, Proc. SPIE, 3354, 566
McLean, I. S., Graham, J. R., Becklin, E. E., et al. 2000, Proc. SPIE, 4008, 1048
McLean, I. S., McGovern, M. R., Burgasser, A. J., et al. 2003, ApJ, 596, 561
Oke, J. B., Cohen, J. G., Carr, M., et al. 1995, PASP, 107, 375
Rajpurohit, A. S., Reylé, C., Allard, F., et al. 2013, A&A, 556, A15
Rayner, J. T., Cushing, M. C., & Vacca, W. D. 2009, ApJS, 185, 289
Rayner, J. T., Toomey, D. W., Onaka, P. M., et al. 2003, PASP, 115, 362
Reid, I. N., Cruz, K. L., Kirkpatrick, J. D., et al. 2008, AJ, 136, 1290
Reid, N. 1997, in ASP Conf. Ser. 127, Proper Motions and Galactic Astronomy, ed. R. M. Humphreys (San Francisco, CA: ASP), 63
Reiners, A., & Basri, G. 2006, AJ, 131, 1806
Riaz, B., Gizis, J. E., & Harvin, J. 2006, AJ, 132, 866
Robertson, T. H. 1984, AJ, 89, 1229
Roeser, S., & Bastian, U. 1988, A&AS, 74, 449
Röser, S., Schilbach, E., Schwan, H., et al. 2008, A&A, 488, 401
Salim, S., & Gould, A. 2003, ApJ, 582, 1011
Schilbach, E., Röser, S., & Scholz, R.-D. 2009, A&A, 493, L27
Schmidt, S. J., West, A. A., Burgasser, A. J., Bochanski, J. J., & Hawley, S. L. 2010a, AJ, 139, 1045
Schmidt, S. J., West, A. A., Hawley, S. L., & Pineda, J. S. 2010b, AJ, 139, 1808
Scholz, R.-D., Lehmann, I., Matute, I., & Zinnecker, H. 2004a, A&A, 425, 519
Scholz, R.-D., Lodieu, N., & McCaughrean, M. J. 2004b, A&A, 428, L25
Sheppard, S. S., & Cushing, M. C. 2009, AJ, 137, 304
Simcoe, R. A., Burgasser, A. J., Bernstein, R. A., et al. 2008, Proc. SPIE, 7014, 70140U
Simcoe, R. A., Burgasser, A. J., Bochanski, J. J., et al. 2010, Proc. SPIE, 7735, 773514
Sivarani, T., Lépine, S., Kembhavi, A. K., & Gupchup, J. 2009, ApJL, 694, L140
Stephenson, C. B. 1986a, AJ, 91, 144
Stephenson, C. B. 1986b, AJ, 92, 139
Teegarden, B. J., Pravdo, S. H., Hicks, M., et al. 2003, ApJL, 589, L51
Vacca, W. D., Cushing, M. C., & Rayner, J. T. 2003, PASP, 115, 389
van Altena, W. F., Lee, J. T., & Hoffleit, E. D. 1995, The General Catalogue of Trigonometric [Stellar] Parallaxes (4th ed., New Haven, CT: Yale Univ. Observatory)
van de Kamp, P. 1953, PASP, 65, 73
van Leeuwen, F. 2007, A&A, 474, 653
Walker, A. R. 1983, SAAOC, 7, 106
West, A. A., Hawley, S. L., Bochanski, J. J., et al. 2008, AJ, 135, 785
Wright, E. L., Eisenhardt, P. R. M., Mainzer, A. K., et al. 2010, AJ, 140, 1868
Wright, E. L., Kirkpatrick, J. D., Gelino, C. R., et al. 2013, AJ, 147, 61
Wroblewski, H., & Torres, C. 1996, A&AS, 115, 481
Zacharias, N., Finch, C. T., Girard, T. M., et al. 2013, AJ, 145, 44
Zhang, Z. H., Pinfield, D. J., Burningham, B., et al. 2012, poster presented at "50 Years of Brown Dwarfs: From Theoretical Prediction to Astrophysical Studies": http://www.mpia.de/homes/joergens/ringberg2012_proc/zhang.pdf
Zhang, Z. H., Pinfield, D. J., Burningham, B., et al. 2013, European Physical Journal Web of Conferences, 47, 6007